Doctoral Thesis for EU Horizon 2020 Program

MARIE SKLODOWSKA-CURIE 860243: LIVE-I

Host University: **Università degli Studi di Napoli Federico II**

Industry Partner: **Adaptronica Sp. z o.o.**

Thesis topic:

Semi-active Vibration Control for Vehicle Transmission Systems

UNINA doctoral school coordinator:
Prof. Michele Grassie

Academic Supervisory Team:
Prof. Francessco Franco, Dr. Guissepe Petrone, Prof. Sergio de Rosa

Industry Supervisor:
Dr. Przemysław Kołakowski

Jury Members:
Prof. Christian Adams, Prof. Emiliano Rustighi, Prof. Luigi Grassia

Ph.D. Student:

Sina Soleimanian

Defense date: 28 Feb 2024

Abstract

This doctoral thesis proposes a novel semi-active vibration control technique for mechanical transmission systems. The backbone of current research technology is the adaptive stiffness and damping properties of metal rubber (MR) which plays the role of tuning to the vibrational system eigenmodes. The adaptive properties of MR material were proved by a previous study, but the present research investigates the effect of this feature on the structural response and designs an MR-based semi-active vibration controller for industrial application. For this purpose, the semi-active control strategy is created based on an optimal tuning using experimental harmonic test results. The control strategy is applied in practice using a linear actuator controlled by a double pole double throw (DPDT) relay, and National Instruments hardware and software for reading data and writing the control task. The isolator attachment position is defined through the analysis of eigen mode shapes that are predetermined by numerical simulation.

The assessment of isolator effectiveness is carried out in two phases. The first phase investigates the vibration control rate for a cantilevered plate and the second phase studies a plate accommodating a bearing and a shaft. The last phase is dedicated to a plate accommodating bearing and shafts in a commercial vehicle transmission system.

The first phase is prominent since it demonstrates the vibration isolator effect on dynamics response of a well-known structure. In the second phase, a maximum isolation rate of 55.17 % is measured near the vibration isolator position. It is observed that the isolation position has a prominent effect on structure vibration behavior where the elastic wave has been reduced in amplitude by passing the isolator position. The effectiveness of the MR-based semi-active control approach is eminent and its application for vibration isolation of commercial mechanical transmission systems could be studied in the future.

In the third phase of study, a particular automotive transmission component—precisely, a plate dedicated to accommodating bearings—has been selected as the focus of research to control its noise and vibrations. A microcomputer-driven

control system is applied, featuring characteristics such as high performance, compact size, lightweight design, and energy efficiency, which make it ideal for testing in the automotive sector. The efficacy of the devised control scheme is assessed through the deployment of accelerometers and sound intensity probes to quantify the vibrations and the radiated acoustic power, respectively. Interesting noise and vibration reduction rates are achieved using both open-loop and closed-loop strategies. This research opens the horizons to employ MR material in a semi-active configuration for industrial requirements surpassing its classical passive implementation, notably in terms of wide-band attenuation performance.

To my beloved wife, whose unwavering support and deep bond mean the world to me, my dear brother, for his kindness, and my parents, who instilled the value of education since my earliest days.

Acknowledgment

This project has received funding from the European Union’s Horizon 2020 research and innovation program under the Marie Skłodowska-Curie grant agreement No 860243. The author would like to acknowledge all the Institutions and Partners involved within the LIVE-I project.

The author expresses sincere gratitude to his esteemed supervisors: Professor Francesco Franco, Professor Sergio De Rosa, Dr. Giuseppe Petrone, and Dr. Przemysław Kołakowski. Their invaluable assistance and consistent support have been pivotal in the completion of this work.

The author would also like to thank, Dr. Marek Kokot, Dr. Arkadiusz Mróz, and Dr. Krzysztof Sekuła, Mr. Janek Biczyk , Mr. Damian Sala employed by Adaptronica sp. z o.o. R&D company for their valuable insights and support during this research.

In addition, the author wishes to thank Timotion company for offering TA29 linear actuator and providing technical advice.

List of Publications and conference proceedings

Semi-active vibro-acoustic control of a commercial vehicle transmission system using a metal rubber-based isolator https://www.sciencedirect.com/science/article/abs/pii/S0003682X24000124	2024
Application of metal rubber for semi-active vibration control of mechanical transmission systems, Journal of Vibration and Control. https://doi.org/10.1177/10775463231192747	2023
Numerical realization of a semi-active virtual acoustic black hole effect. Frontiers in Mechanical Engineering. https://doi.org/10.3389/fmech.2023.1126489	2023
Optimal tuning of an adaptive vibration absorber for vibration control of vehicle transmission system, EACS conference, Warsaw http://eacs2022.ippt.pan.pl/EACS%202022%20-%20Book.pdf	2022

Participated events organized by LIVE-I

Event title	Place	Date
Short overview about Magna and MPT TS the portfolio of transmissions with the main attributes	Magna company, Germany	12.11.2020
Short overview about VTC Some case studies of the design of gearboxes	Vibratec company, France	13.11.2020
Noise, Vibration, and Harshness of gear transmissions	Vibratec and ECL[1], France	25.01.2021
All about gear transmissions	Magna Powertrain & ECL	25.02.2021
Genral event about NVH Design	TUD	20.04.2021
Mechanical Design, Uncertainties and Tolerances	UNINA[2], and Powerflex	14-15.06.2021
Automobiles mechatronics, Workshop Smart technologies for NVH design, and Guided tour through TUD acoustic laboratory	TUD[3], Germany	17.11.2021
Digital Twins, Data mining and collection on real car	TUD, Germany	18.11.2021
Active vibration and noise control	Adaptronica & WUT[4], Poland	12.07.2022
Lightweight structures through metamaterials	University of Campinas & École Centrale de Lyon (virtual)	13-14.10.2022

[1] Ecole Centrale de Lyon
[2] Università di Napoli Federico II
[3] Technical University of Darmstadt
[4] Warsaw University of Technology

Experimental techniques for NVH of gear transmissions	UNINA, and Powerflex, Italy	15-17.11.2022
Clean Vehicles and Entrepreneurship	TUD, Compredict GmbH, Fraunhofer LBF and VDMA, Germany	15-17.05.2023
R & D activities in VibraTec (research on drive line)	Vibratec and ECL, France	10-12.10.2023

Nomenclature

$A_{(\Delta f_i)}$	the integral of summed of squared accelerations in selective frequency domains
A_{tot}	the integral of summed of squared accelerations in the whole frequency domain
a	acceleration
a_i	acceleration of i^{th} accelerometer
$[B]$	damping matrix
C	pre-compression level
C^{op}	optimal pre-compression level
D	excitation direction vector
e	Euler’s number
f	frequency
H	Heaviside function
i	index
$[K]$	stiffness matrix
$[M]$	mass matrix
M_r	the ratio of effective mass to total mass
n	number of frequency intervals
N	number of sensors
P	force
p	input force amplitude
$\{q\}$	displacement
t	time
U	area under the mobility-frequency response curve in the whole frequency range
u	area under the mobility-frequency response curve in sub-frequency ranges
v	design criteria variable
V	velocity
W	radiated power
ρ	density
Φ	mode shape

List of Figures

List of Tables

Contents

Chapter 1: Introduction

1.1 Framework of research

The present scholarship is a branch of the mother project entitled LIVE-I. LIVE-I which itself stands for Lightening and Innovating transmission for improving vehicle environmental impacts is defined in the framework of MARIE-SKLODOWSKA CURIE ACTIONS research fellowship. The program consortium involves 12 academic and non-academic members to build an innovative training network, and promote research on design of lightweight gear transmission systems with minimal environment impact. Nine ESR[5]s are recruited each of which is assigned to pursue a branch of the whole project.

The present research thesis is devoted to ESR7, Sina Soleimanian who was hosted by the Industrial Engineering department of University of Naples Federico II (UNINA) in Italy, and passed an industrial journey at Adaptonica company in Poland. The Industrial Engineering Department of the UNINA specializes in Industrial Engineering, addressing issues of cultural, social, and economic development while fostering technology transfer, innovation, and commercial partnerships. With specialized courses in energetic and mechanical engineering, aerospace and naval engineering, and quality and management engineering, the department is home to a Ph.D. school in industrial engineering.

Adaptronica was established as a spin-off from the Institute of Fundamental Technical Research in Warsaw, consisting of a team of highly skilled engineers who are dedicated to leveraging state-of-the-art technical advancements. Their expertise lies in intelligent technologies, seamlessly integrating powerful software algorithms, intelligent materials, and vibroacoustics relying on mechanics, electronics, and other scientific disciplines. Adaptronica's primary focus is on developing applications that enhance the durability and safety of engineering constructions, encompassing various areas such as automobiles, bridges, and aircraft.

[5] Early stage researcher

The present research is partly carried out in Adaptronica company and the UNINA. The knowledge support from UNINA scholars in Pasta Lab became the driving force to promote the current research when it met the expertise and experience of Adpatronica experts. Having along track of documented records in NVH field (D’Alessandro et al., 2013; De Rosa et al., 2012; Petrone et al., 2014), Pasta lab possessed the necessary potential to oversee the academic supervisory of the project. On the other side, the Adaptronica company contributed to the project through offering insightful consultation by their experts with noticeable research track in the relevant field (Kołakowski et al., 2011; Mróz et al., 2008).

1.2 Motivation and Background

Noise, vibration, and harshness (NVH) performance in the automotive industry have become a crucial design factor due to the increasing demand for vibro-acoustic comfort. This trend is further reinforced by the implementation of new standards such as UN/ECE[6] regulations (Boer and Schroten, 2007; De Roo, 2013; UN-ECE Regulation, n.d.) which imposes limitations on permissible noise and vibration levels in the automotive industry. To have a basic insight about the contribution of noise sources from a pass-by vehicle *Figure 1* (Braun et al., 2013; Li, 2018) represents a graphical ranking. According to this ranking, the powertrain exhibits a moderate to substantial impact on the overall noise emission. In addition, it is documented that at low speeds the noise produced by the powertrain and engine is dominant (Ahmed, 1995; Covaciu et al., 2015; Laib et al., 2019). Since noise with low frequencies is perceptible to human ear, there is ongoing research aimed at identifying, analyzing, and controlling this kind of noise.

[6] United Nations Economic Commission for Europe

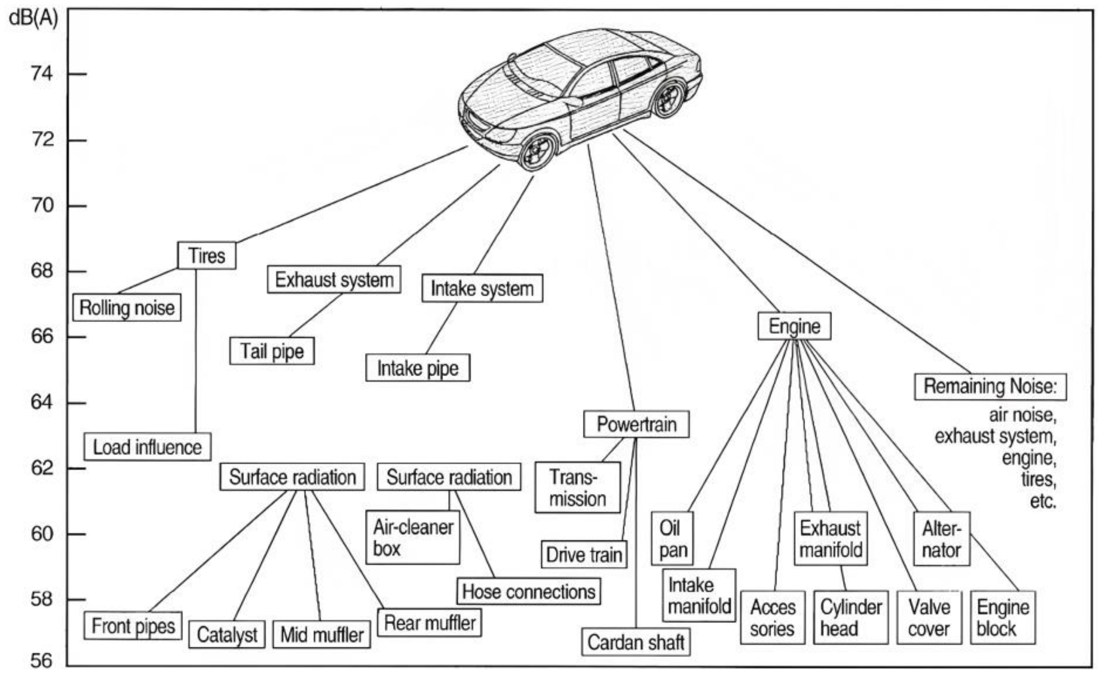

Figure 1. Noise source ranking for a pass-by vehicle (Braun et al., 2013)

Another point worth noting is that electric vehicles (EVs) have no engine noise, instead, the major source of noise is gear noise caused by the powertrain operation (Son et al., 2020). Hence, the study of transmission noise has gained momentum in recent years in response to the escalating demand for vehicles electrification.

The study of vehicle gearbox noise involves a thorough examination of the areas of NVH detection, analysis, and strategic control. This interdisciplinary endeavor converges principles from mechanical engineering, materials science, and computer science exemplifying the amalgamation of various academic disciplines. NVH analysis employs particular techniques like modal testing to uncover natural frequencies and vibrational modes, additionally identifying noise sources and their propagation pathways. An example of modal testing performed on a real gearbox assembly, which includes gears, shafts, and bearings supported by a housing is demonstrated by *Figure 2* (Zhang, 2018).

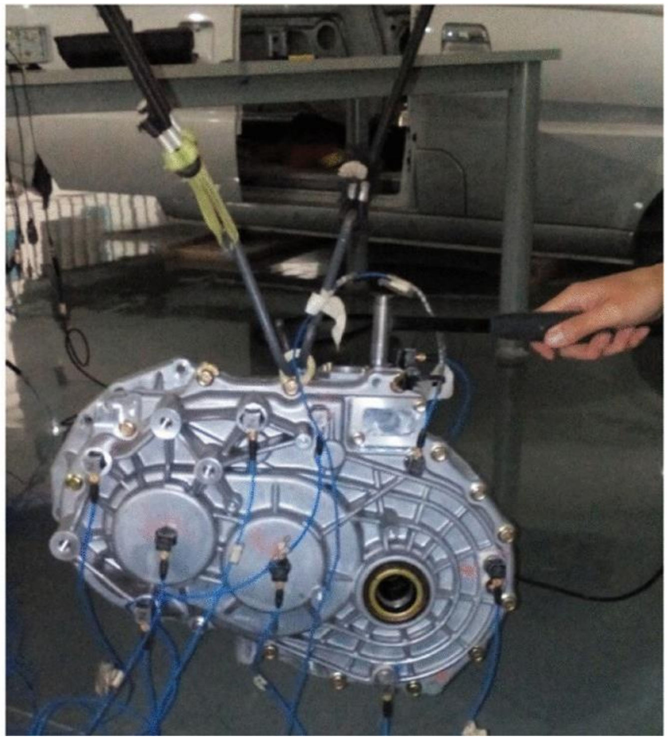

Figure 2. Modal testing of a vehicle gearbox (Zhang, 2018)

The understanding of vehicle gearbox vibration response can effectively help decide the proper solution for NVH improvement, and consequently design and apply the chosen solution. There exist four common techniques for controlling gearbox noise and vibrations. These techniques encompass: (1) active inertial actuators on the gear body, (2) semi-active gear-shaft torsional coupling, (3) direct active bearing vibration control, and (4) active shaft transverse vibration control. These approaches aim to either prevent vibration energy transmission into the housing or mitigate the effect of dynamic mesh force excitation. Their contribution to reduce vibrations in transmission systems is significant as it can improve overall durability and performance. An example of vibration control mechanism is represented by ***Error! Reference source not found.*** where piezoelectric actuators c ontribute in bearing induced reverberation.

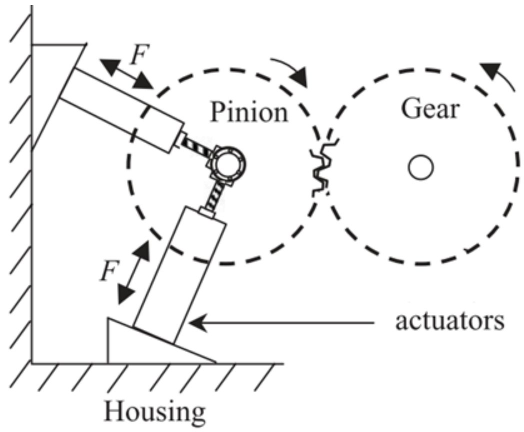

Figure 3. A control solution for bearing induced vibrations (Zhang, 2018)

Among different control strategies for vehicle transmission system noise and vibration dampening, semi-active solutions have shown a great potential according to experimental and simulative studies. By enabling controlled damping with minimal energy input, these solutions offer efficiency advantages. An ongoing research (Guglielmino and Edge, 2004) has been conducted to effectively implement semi-active approaches in the entire vehicle powertrain system.

Semi-active approaches involve making choices or trade-offs between power and bandwidth. The bandwidth itself requires specific attention since mitigating high frequency noise requires low stiffness and vice versa. The control force defining stiffness needs support from a source with a widely variable output for adaptability to a broad frequency range. Moreover, alongside the stiffness range, the switching resolution is a crucial factor that can significantly impact attenuation performance. The desired resolution requires a customized or carefully chosen technology to control the input energy properly. Thus, many considerations are required to be taken to guarantee an ideal wideband attenuation with minimal required input energy.

Semi-active systems can be implemented using a relatively simple control logic. Consequently, the application of control circuitry, programming, and automation can be executed in a straightforward manner. While the significance of simplicity as a criterion may depend on specific needs, it can lead to less space needed for control hardware in a vehicle, lighter components, and make maintenance and troubleshooting more straightforward when necessary. One point to mention is that, simplicity of control does not mean a controller with simple architecture and preferences can meet the project requirement. In fact, an ideal controller for vehicle NVH purpose at research stage should offer many characteristics such as efficient architecture, high clock speed, analog-to-Digital Converters (ADC), multiple I/O Ports, interrupt handling, and low latency communication interfaces.

Semi-active systems do not require a live optimization process common in active systems which reduces the system degree of robustness which is a critical factor in automotive sector. In fact, the system can be optimized in advance, and the control can be applied using an optimal algorithm designed for an open- or closed-loop strategy.

In conclusion, semi-active systems offer numerous advantages that can significantly enhance vehicle NVH characteristics, provided the aforementioned challenges are successfully overcome.

1.3 Research objectives

The present Ph.D. thesis is primarily concerned with reducing vibration propagation and acoustic radiation in vehicle gearbox systems. This quest is consistent with the underlying objective of improving passenger comfort, a critical requirement for contemporary car design. Furthermore, it aligns with the automotive sector's broader drive for sustainable mobility solutions, as the mitigation of these effects aids in reducing noise pollution. In accordance with this aim, the thesis follows several sub-objectives that address the intricate technical and perceptual aspects. These sub-objectives which are expressed in the following serve as a road map for advancing both vehicle engineering practices and the automotive industry's commitment to eco-friendly transportation solutions.

1. *Identification of noise and vibration source, and noise path*

Understanding the sources of noise and vibration is critical prior to isolator design and installation procedure. This understanding, based on insights from vehicular dynamics research, reveals the complicated interplay between vehicle components and transmitted forces and the noise propagation path, identifying major contributors to noise and vibration generation. Hence, this knowledge is vital to optimally tune isolator properties, successfully targeting certain frequencies and vibration modes, and encouraging superior noise and vibration reduction.

2. *Design of the semi-active isolator*

Initially, the selection of an appropriate adaptive technology that aligns with dynamic phenomena and fulfills automotive sector prerequisites is imperative. The selected technology then has to be developed in order to create a semi-active control isolator. This objective can be effectively realized by consolidating the requisite hardware, obtainable through market or fabricated from laboratory-developed components. This entails designing the isolator considering electromechanical aspects to enable semi-active automatic control. The major components include the electrical circuit elements, mechanical control devices (sensors, actuators, etc.), embedded systems (microcontrollers, microcomputers, etc.). Moreover, optimal tuning of the isolator is an essential design procedure to maximize its noise and vibration reduction capacities. Indeed, the optimization of isolator tuning, facilitated by a systematic parametric followed by an optimization algorithm, makes it possible to establish an optimal control scheme. The other side of design is the software development which entails programming the embedded system in order to accomplish the reading and writing tasks properly considering reaction time, the control algorithm, safety conditions and so on.

The multifaceted approach to design the semi-active isolator ensures harmonization between technology, design, and performance, reflecting a comprehensive strategy in pursuit of minimizing noise and vibration impacts.

3. *Application of the semi-active isolator*

To ensure the proper functionality and efficacy of the designed semi-active isolator, preliminary testing on a basic structure with known dynamic behavior is required. Hence, the success of this stage instills the confidence needed to progress further.

In fact, the implementation can extend to more intricate vibrating systems. In this study, the isolator's performance is initially evaluated on a cantilevered plate, followed by its application to a more complex structure featuring a plate hosting a bearing and a shaft. The assessment concludes with evaluating the effectiveness of the approach on a commercial vehicle transmission component. This methodological progression safeguards the isolator's reliable integration and performance across varying levels of complexity.

Chapter 2: Literature Review

2.1 Chapter organization

This chapter provides a comprehensive insight into various aspects of NVH related domain in vehicle transmission system. The chapter begins by clarifying dynamic models of these systems, scrutinizing the central components of their operation, including gears, shafts, and bearings, and extending the model to include stationary components, including structural shells and associated structures. This knowledge base provides a solid framework for understanding the micro-complexities underlying automotive transmission performance.

The great advance in transportation modeling, known as the reduced hybrid model, is described in these pages. This new approach has the potential to change the way we think about and engineer transportation. In addition, the chapter initiates an intensive investigation in the area of vibration control in automotive applications. This includes research into techniques and strategies aimed at reducing vibration and increasing overall driving efficiency, contributing to further improvements in vehicle dynamics.

In the field of vibration monitoring, this chapter critically examines the growing trend of partial vibration and acoustic manipulation techniques. These mechanisms are necessary to achieve a delicate balance between driving comfort and dynamic performance, a perennial goal in modern automotive design. This chapter also looks at "Metal Rubber" whose properties have the potential to change how engineers manage vehicle vibrations and dynamics, marking an exciting development in automotive engineering.

2.2 Dynamic modeling of vehicle transmission systems

Many engineering problems require modeling of structures with a large assembly of components. Subsequently, complexity of modeling, heavy computation cost, higher degree of nonlinearity is often associated with modeling these large assemblies. Hence, employing decoupled components for modeling, analysis and optimization could be an effective approach to overcome the aforementioned challenges.

Decoupling of components (Wang, 2010) is also useful to facilitate noise source identification and analysis. In some applications when a source is deliberately disconnected, like removing the engine mount which results a significant decrease in noise amplitude at the receiving point, the primary root cause becomes evident.

Quantifying individual components contributions to total NVH (Noise, Vibration, and Harshness) is another reason for component decoupling, in order to evaluate and quantify the degree to which each component or subsystem affects the general NVH behavior of a vehicle. Engineers can prioritize and efficiently address certain contributors by determining the relative participation of various sources in creating noise or vibration. In a case study (Noh, 2017), a methodology for evaluating and measuring the contributions of various noise and vibration sources in the passenger car interior is presented. The study identifies and ranks the key factors that contribute substantially to total NVH by combining subjective assessments, objective measures, and statistical analysis. The authors' insights into the individual contributions of different sources enable targeted changes for efficient NVH reduction.

Studies on decoupled vehicle transmission system housing and components can be classified by three distinct strategies, 2.2.1) Modeling of dynamic components: gears, shafts, etc, 2.2.2) Modeling of stationary component: casing, and 2.2.3) Reduced hybrid modeling: dynamic components integral with stationary casing. Each strategy offers its own objectives and meets particular requirements which is discussed as follows.

2.2.1 Modeling of dynamic components: gears, shafts, and bearings

This strategy requires creating precise models of the moving components of the gearbox system, such as gears, shafts, and other relevant components. These models simulate the dynamic behavior of these components, capturing their mobility, forces, and interactions. Engineers can evaluate the effect of these components on the overall vibration and noise response of the system. To study the vibration problem of gear and shaft sets, computational methods are adopted developing lumped parametric models (Amabili and Rivola, 1997; Jia and

Howard, 2006; Nguyen and Dien, 2009). These models are of significant value to understand and conduct case studies considering the influence of factors of interest into equations. *Figure 4* represents an example of lumped parametric modeling for torsional vibration of a gear pair (wheel and pinion). The meshing process of gears induces a variable mesh stiffness *k(t)*, and an added viscous damping *c(t)*. The source of harmonic motion in real application of gear systems is variable speed and STE. STE can be considered as an excitation function *e(t)*.

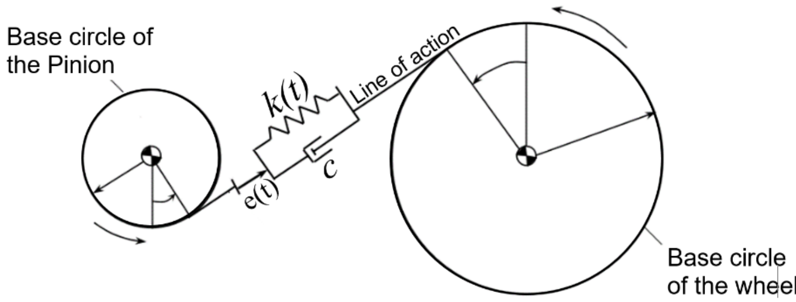

Figure 4. Lumped-parameter model for gear vibration

Accuracy limitations due to approximations limits the viability of these approaches for extensive tasks like powertrain NVH analyses. Specialized tools like Romax Designer, employing finite element discretization, enhance precision by consolidating components into super elements, reducing stiffness, and mass matrices. In 2019, Ouyang et al. (Ouyang et al., 2019) used Romax Designer[1] to obtain the stiffness of the bearing element required for their theoretical dynamic model of gear-roller-bearing. In 2020, Cho et al. (Cho et al., 2020) used Romax Designer for mico-geometry optimization of a drive reducer gear.

2.2.2 Modeling of stationary components: housing shell and associated components

This strategy includes simulating the non-moving components of the transmission system, particularly the casing that protects the dynamic components. Engineers may analyse the casing's vibration and acoustic characteristics using this method, then optimize the design to reduce noise transmission and structural resonance.

[1] A powerful tool dedicated for design of mechanical transmissions

Thus, understanding the vibration response of the casing enables engineers to improve the overall performance and comfort of the vehicle.

The casing of transmission systems plays a pivotal role in structure-born noise propagation. Several scholars have been analyzed the casing of gearboxes to understand its vibration behavior and noise transmissibility (Kumar et al., 2015; Ognjanović and Kostić, 2012). Many scholars studied the structural response of housing itself without dynamic components using finite element method. In an investigation on heavy vehicle transmission casing by Kumar (2015) et al., FE simulation is conducted on the housing itself. Modal analysis revealed three main modes of torsional vibration, axial bending vibration, and axial bending with torsional vibration two of which are reported by *Figure 5*. Moreover, they investigated the effect of transmission casing material on mode shapes and natural frequency.

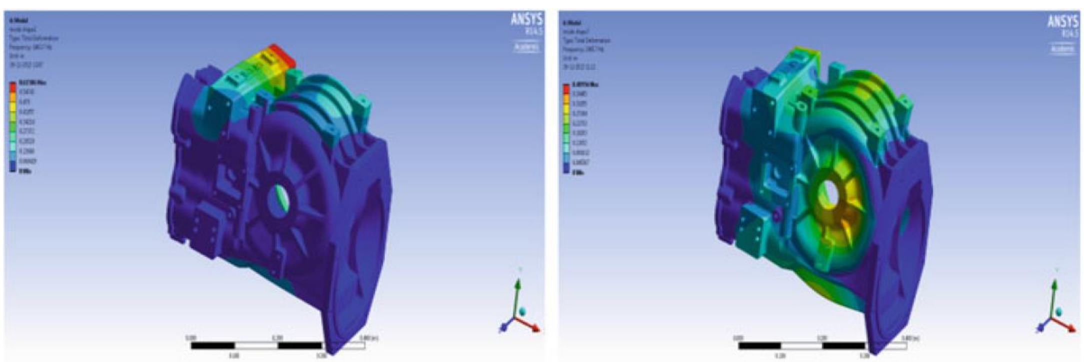

Mode 2 f_2=1463.7 Hz Mode 7 f_7=2495.7 Hz

Figure 5. Two different mode shapes of structural steel transmission casing

Another motivation in decoupling a housing component, is to predict the remaining lifespan and health condition of the component. For instance, in one study (Khawaja and Vachtsevanos, 2009) a UH-60 Blackhawk helicopter gearbox plate is disconnected for health monitoring.

The finite element model of the plate (*Figure 6*) is used to evaluate its vibration response and infer several features which could reflect the growth pattern of a simulated fault.

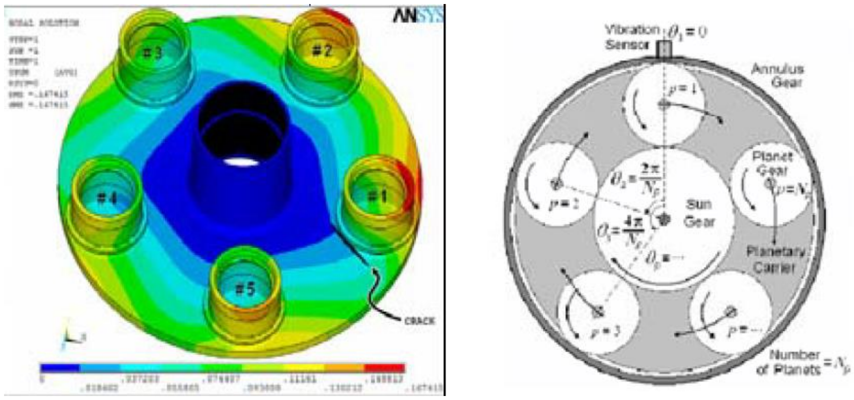

Figure 6. (a) ANSYS model of the gearbox plate (b) Mechanical layout

The finite element simulation of this plate showed that the Side-Band Ratio (SBR) correlates remarkably well with the actual fault. It is observed that this feature varies as the crack grows with time till the gear-plate breaks into half; a stage considered catastrophic.

2.2.3 Reduced Hybrid Modeling

This method is beneficial when prioritizing specific component improvement, making detailed assembly modeling unnecessary. Adopting reduced hybrid modeling shifts focus from miscellaneous components, streamlining research efforts and facilitating targeted enhancements. In this regard, a recent practice (Xie et al., 2016) to avoid the intricate modeling of untargeted components is introducing condensation models. This modeling technique efficiently condenses certain parts or degrees of freedom in a larger system. Utilizing a low-order model approximates the original high-order model, simplifying the system for improved computational efficiency. Condensation models reflect the impact of condensed components on overall dynamics. Analysis of transmission systems through modeling dynamic parts integrated with a condensate casing could be of prime value in terms of computation cost. Duan et al. (Duan et al., 2021) used lumped parametric model for the dynamic components coupled with a condensation model of housing obtained from FEM presented by *Figure 7*.

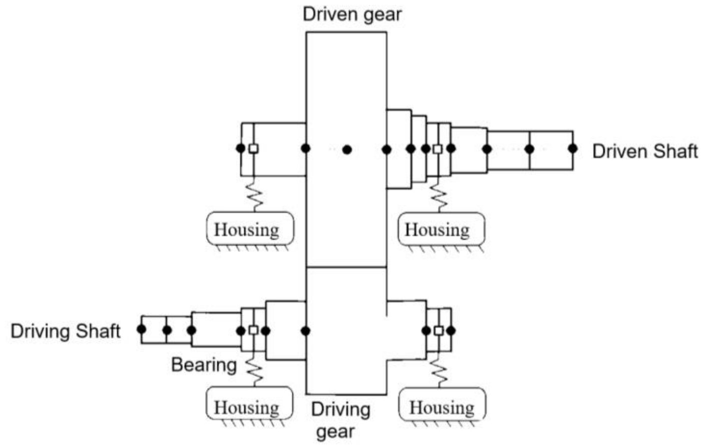

Figure 7. Employing condensation model in gearbox dynamic simulation

Basically, gearbox transmission error (TE) analysis focuses on modeling meshing gears, often neglecting component flexibility. The innovative rigid-flexible dynamic approach considers the meshing pair, flexible shaft, bearing, and housing—introducing housing flexibility through model condensation. Validation through modal and TE test rigs enhances credibility.

In one study (Duan et al., 2021), the TEs of gear transmission systems with and without a housing are compared, as presented by *Figure 8*. The figure shows the TE that takes into account the flexibility of the housing is smaller than the TE which ignores the flexibility of the housing. When the speed is higher, this phenomenon is more pronounced. In fact, the meshing force and bearing force decrease when the housing vibration is taken into account in the whole dynamic system.

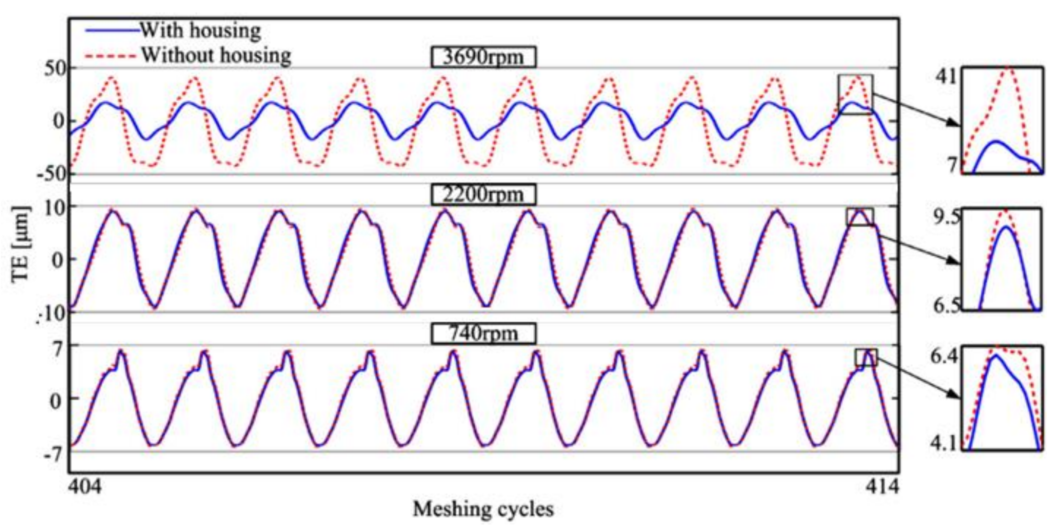

Figure 8. TE with and without housing at different speeds (Duan et al., 2021)*.*

A special kind of condensation model is *super element*. A complicated component or substructure is replaced with a reduced-order model using this modelling approach, usually one with a few degrees of freedom. The dynamic behavior of the original component or substructure is encapsulated in the reduced-order model, known as the super element.

To study dynamic characteristics of gear transmission system, Kong et al. (2021) modeled the gearbox housing as a rigid body and neglected its elasticity in the gear dynamic analysis. Finite element methods establish gear-rotor-bearing and gear-rotor-bearing-housing models. Timoshenko beam elements represent shafts, and two housing models—rigid and flexible/lighter—are adopted. Housing dynamics are simplified as super elements through the dynamic substructure method. Initial step involves creating the finite element model of the housing. Then, the nodes are divided into boundary nodes and inner nodes. The boundary nodes are used to connect the shaft nodes as shown in *Figure 9*.

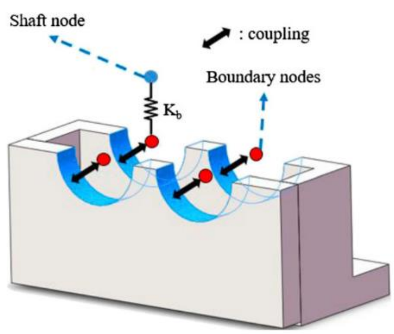

Figure 9. Schematic diagram of boundary nodes of housing connected to shaft nodes

2.3 Vibration control in vehicle applications

The substantial contributor to powertrain noise is the gear transmission system, responsible for transporting structure-borne noise from the gear mesh to the shaft and bearings (Koronias et al., 2011; Wang et al., 2016; Wu and Wu, 2016). This noise subsequently propagates all over the transmission housing and finally into the surrounding air.

Vehicle transmission noise can be mitigated directly or indirectly. Direct methods manipulate noise, while indirect ones dampen structural vibrations. Active noise control, a direct technique, requires continuous energy for anti-noise generation (Jiang et al., 2021; Munir and Abdulla, 2020). While the indirect approaches can follow an active, semi-active, or passive modes of control. Inter alia, passive control is the most prevalent practice in automotive industry due to its simplicity and robustness. For instance, passive soundproofing treatment resulted a remarkable reduction in vehicle transmission noise (Han et al., 2022; Viscardi et al., 2018). The downside of passive techniques is their limited effective frequency spectra (Ma et al., 2021; Zhang et al., 2023). On the other hand, active solutions, even with self-powered strategies (Fredriksson et al., 2002; Li et al., 2023; Shi et al., 2023) such as using engine torque for control, still contend with input power control and reliability issues (Casciati et al., 2012; Stabile et al., 2017; Zuo and Tang, 2013). Instead, semi-active solutions can maintain the reliability of passive solutions while offering great adaptability by taking the advantage of their adjustable parameters (Choi et al., 2004; Symans and Constantinou, 1999). Semi-active techniques offer efficient wide-band vibro-acoustic control in vehicle transmission systems without demanding high input power, making them a practical alternative to active control methods.

2.4 Semi-active vibro-acoustic control techniques

2.4.1 Introduction to semi-active approaches

There exist three main approach for vibration control in dynamic systems: passive, active and semi-active techniques as depicted by *Figure 10*. Sometimes, a hybrid approach, combining these systems, is recommended.

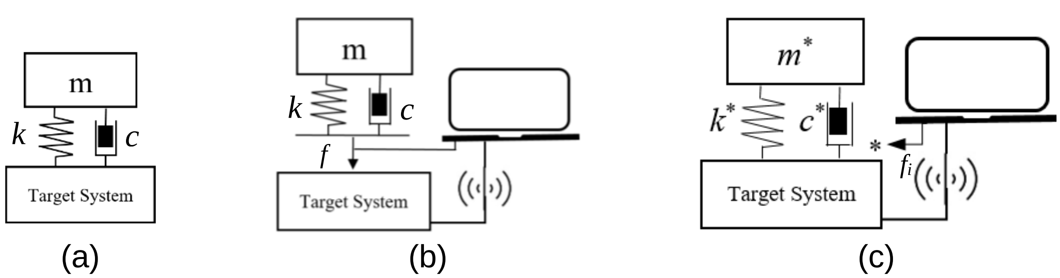

Figure 10. A schematic demonstration of vibration control: (a) passive system, (b) active system, and (c) semi-active system.

The passive vibration control system can incorporate absorber, damper, and mass elements, as shown by *Figure 10(a)*. Passive vibration control system is broadly used in industrial applications thanks to its simple design, low cost and ease of manufacturing. It can be designed for a system's durability. If an ideal stiffness is required, it can be as simple as changing the type of material being used or changing the size of the elements. However, passive mounts can rarely attenuate all of the input vibrations in a system. Active vibration controller attenuates vibration by sending an input voltage, or charge, to an actuator with respect to a feedback response as demonstrated by *Figure 10(b)*. The drawback of this kind of system is its high cost and large power source required. Another disadvantage is that the total system may become unstable if the control system is improperly designed. In contrast, in passive vibration suppression, the total system is always stable. Semi-active vibration isolation systems work based on a modification in stiffness, damping or mass according to a response sensor feedback (*Figure 10(c)*) (Onoda et al., 2003; Syam and Muthalif, 2021). This modification can be realized by an initiation force (f_i). In semi-active vibration isolation systems, external energy demands are lower than the active isolation systems

2.4.2 Adaptive technologies for semi-active control

The concept of semi-active noise and vibration control can be made possible through the design of adjustable mechanisms or the application of adaptive materials, offering effective suppression methods with versatility and adaptability. Adjustable mechanisms include intelligent structures, or flow channels or ducts which can affect the vibration or noise level by modulating a control variable.

Smart mechanisms can operate using a mechanical switch to make the adjustment of structural elements. In other words, with the help of a mechanical switch, vibration attenuation capacity and direction can be moved from one state to another one. A simple illustration of the concept is given by *Figure 11* (Nitzsche, 2012) where the different expansion levels of piezo-stack can adjust the friction and absorption levels.

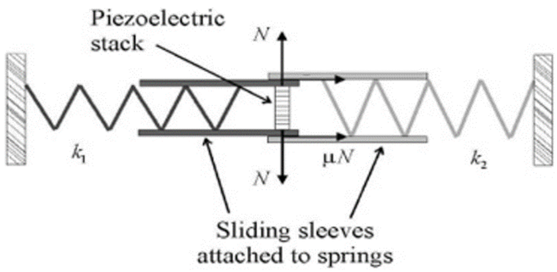

Figure 11. A switch based semi-active control concept.

An industrial application of mechanical switch is semi-active node shown by *Figure 12* (Poplawski et al., 2021) which function is based on an on/off switch by means of a hinge to transfer moment in different directions. The main responsibility of the semi-active node is to stimulate the transfer of strain energy into high frequency vibrations. The technology can be found helpful in truss-like structures.

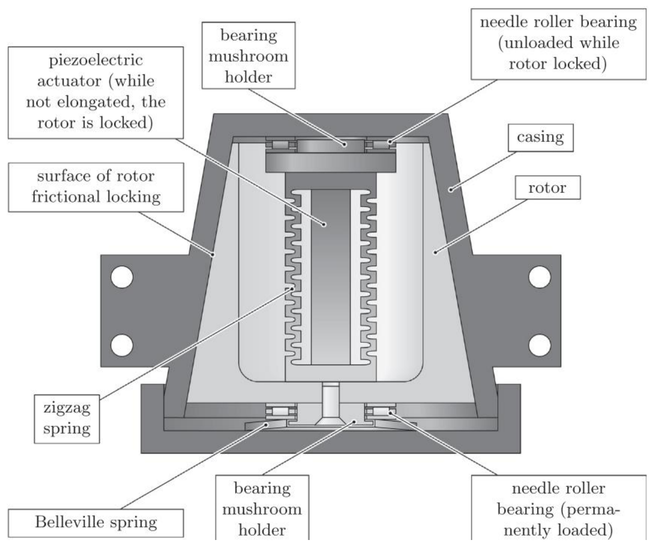

Figure 12. Semi-active node device configuration.

Another practical case for mechanical switch is shown by *Figure 13* (Nitzsche, 2012), where the actuator is developed to move from a soft link to a solid one offering two states of stiffness.

Figure 13. Semi-active actuator (left) with spring components of 163 kN/m and 256 kN/m (right).

The switch based semi-active mechanisms including two states of modulation are limited to particular applications. Therefore, the semi-active concept has been developed to enhance the modulation range by using adaptive materials. In this context, adaptive materials utilized for semi-active control such as piezoelectric shunt systems, magnetorheological (MR) dampers, and Helmholtz resonators will be discused in the following.

Semi-active control extends to airborne noise isolation. For instance, Helmholtz resonators alter noise by adjusting their acoustic impedance, controlled through termination impedance adjustments as shown by *Figure 14*. HRs are often used in duct system to control low frequency noise. It has a small neck and cavity, delivering high transmission loss at its resonance frequency. However, HRs are designed based on the source's exciting frequency due to their limited effective range.

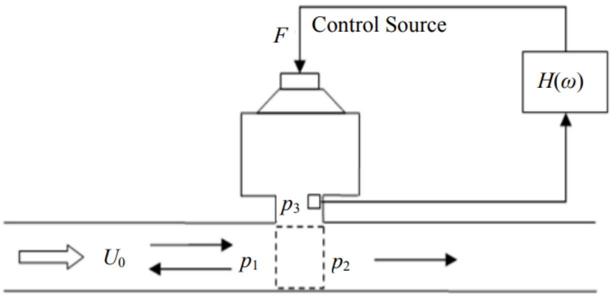

Figure 14. Semi-active airborne noise control using HR resonator.

The case studies presented earlier clarified the contribution of adjustable structures and configurations within the scope of semi-active noise and vibration control. It is now opportune to undertake a comprehensive survey concerning the semi-active control based on adaptive materials. The implementation of adaptive materials is classified in eight groups from *a* to *h*.

a. Shunted piezoelectrics

Piezoelectric patches are well-known for their capability to convert mechanical vibrations to electric power. According to force-voltage mechanical-electrical analogy, the coefficients in differential equation of charge are equivalent to the coefficients in the differential equation of motion as follows

$$L\ddot{Q} + R\dot{Q} + \frac{Q}{B} = V_p \tag{1}$$

$$M\ddot{q} + C\dot{q} + Kq = P \tag{2}$$

$$M \equiv L, C = R, K = B^{-1} \tag{3}$$

where *L*, *R*, and *B* correspond to inductance, resistance, and capacitance, respectively. Moreover, *M*, *C*, and *K* denote mass, damping and stiffness, respectively. So that a vibration control system can be a circuit of electrical elements (resistor, inductor, and capacitor) instead of mechanical elements (damper, mass, and spring) offering several advantages such as less space occupation, faster function, etc. The link between the host structure and the electric circuit can be made by a piezoelectric transducer responsible for energy conversion.

Piezoelectric shunt circuits, widely used in vibration control, incorporate on/off or multi-stage switches for semi-active systems. *Figure 15* illustrates transitions to specific electric properties, enabling tuning for proper vibration control.

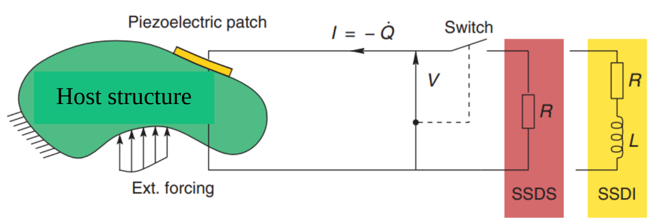

Figure 15. Vibration isolation using piezoelectric shunt circuit.

Recent research (Chatziathanasiou et al., 2021) utilizes a resistive-inductive shunt circuit for highly tunable semi-active vibration control. A tunable potentiometer controls resistive impedance, while two sets of coils with predefined inductance (32 mH and 50 mH) introduce inductance, albeit with a small amount of resistance. The assembly of shunt circuit on the target system is shown by *Figure 16(a)*. The tuning of inductance in frequency domain is done through observation of response surface indicated by *Figure 16(b)*. The experiment setup is illustrated by *Figure 16(c).*

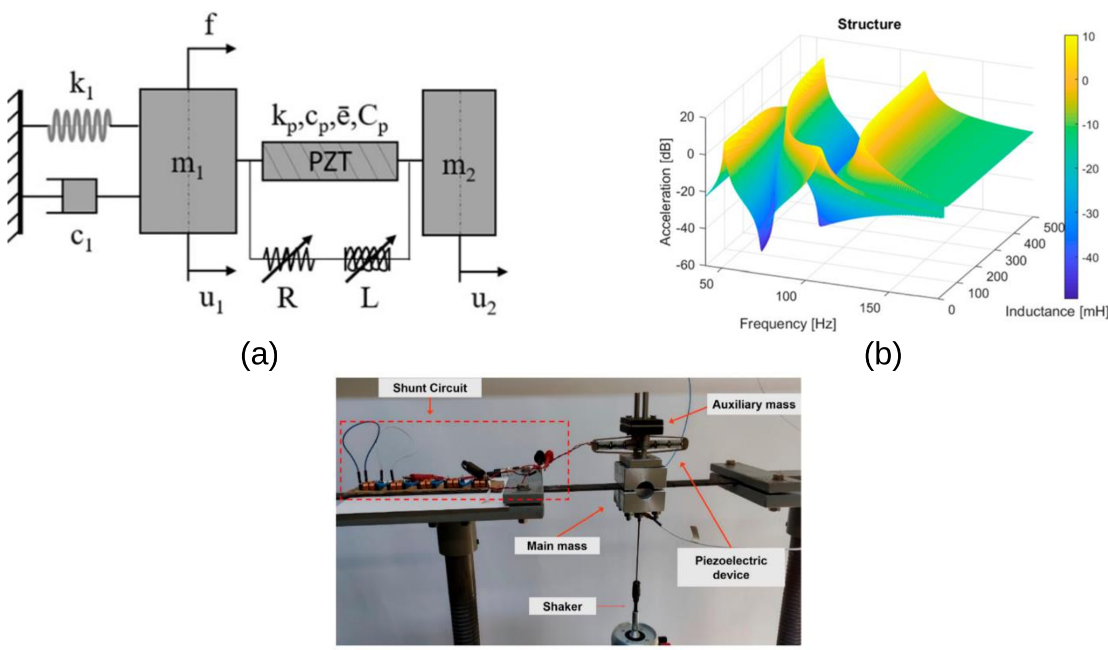

(c)

Figure 16. An implementation of Semi-active shunt: (a) lumped parametric model, (b) tuning inductance via response surface, (c) experimental lab.

In another study (Gardonio et al., 2021), the shunt circuit is employed for maximization of absorbed energy by studying all possible compositions of resistance and inductance. The ultimate goal is to find an optimal path as illustrated by *Figure 17*.

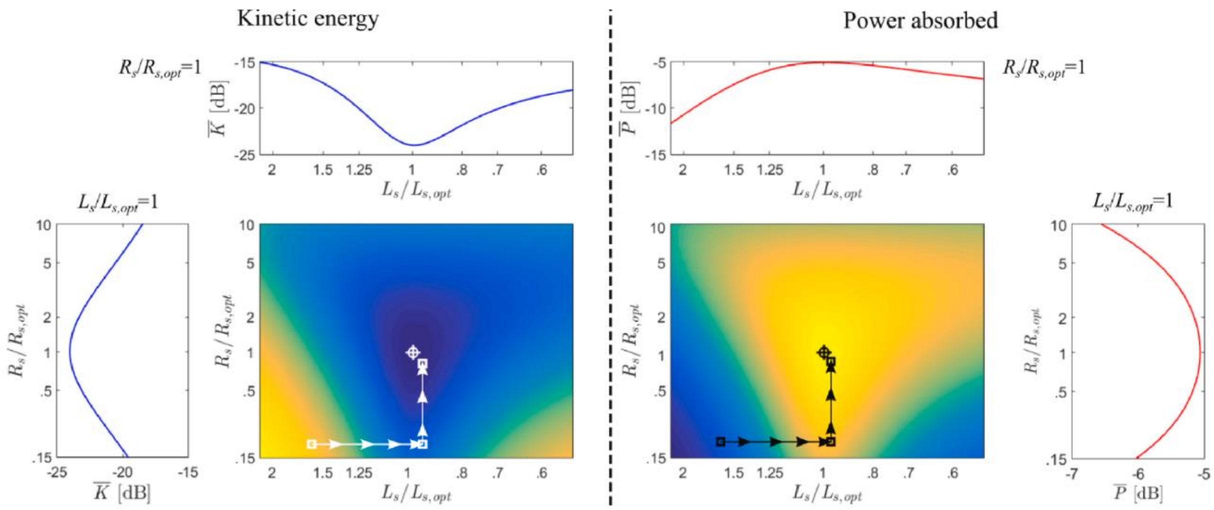

Figure 17. Tuning of shunt circuit resistance and inductance: (a) kinetic energy, (b) power absorbed.

b. Hydraulic damper with variable coefficient of damping

Figure 18 represents a rotational hydraulic damper featuring a rotating rotor, vanes, cam ring, valve core, working chambers, springs, seal rings, and a motor (Zhao et al., 2021). As the rotor rotates, sliding and spring forces cause vanes to contact the cam ring's inner surface, pushing fluid through a tunnel, generating a pressure difference. This difference acts on vanes, producing resistance torque. Simultaneously, sliding vane motion and rotor rotation create frictional resistance moments. The damper coefficient is the total resistance torque quotient by rotor shaft velocity. The damping coefficient is the sum of frictional and fluid resistance coefficients, deduced through dynamic and fluid analyses. Semi-active control is achieved with a motorized cylindrical ball valve regulating fluid tunnel area.

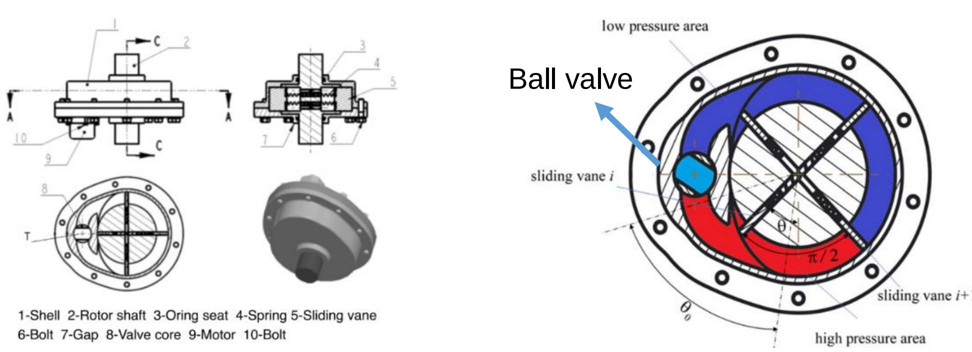

(a) (b)

Figure 18. Tuning of shunt circuit resistance and inductance: (a) structure of the rotational hydraulic damper., (b) sketch map of the fluid pressure.

c. Magnetorheological (MR) fluid damper

In a recent research (Bai et al., 2015) on MR damper, two concentric tubes, and a movable piston/shaft arrangement that slides within the inner tube are used (see *Figure 19*). Concentric tubes create the annular gap for MR fluid flow. The inner tube houses coils, while the outer tube acts as the hydraulic cylinder and flux return. By controlling current in the coils, the damper's controllable range expands, decoupling coil size from stroke requirements and reducing Reynolds number in the gap.

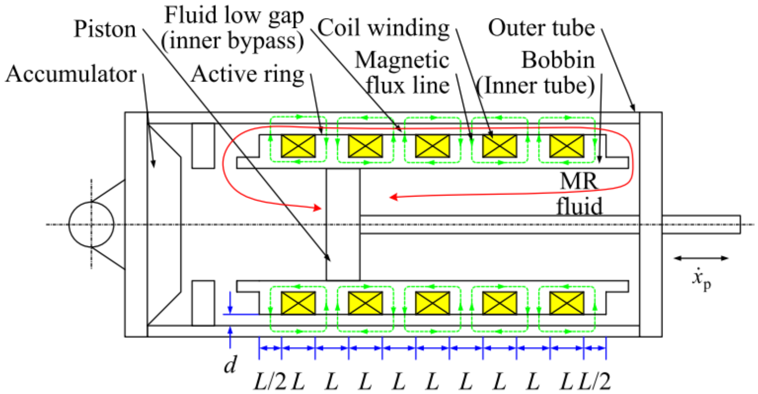

Figure 19. Configuration of an MR damper with an inner bypass.

d. Magnetorheological elastomer

Magnetorheological elastomer are widely used in semi-active vibration isolators. An isolator composed of a MR elastomer, a moving top magnetizer, a bottom magnetizer and a cylinder is designed by Wei et al. (2009) shown by *Figure 20*. An MR elastomer is situated between top and bottom magnetizers, with a coiled copper strip forming an energizing coil. Adjusting the coil current alters the magnetic flux, allowing variable stiffness and damping in response, altering vibration characteristics of the isolator.

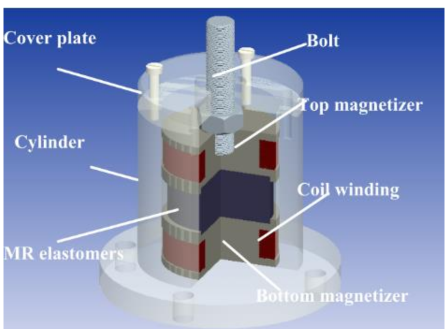

Figure 20. Configuration of the MR elastomers isolator.

e. Electromagnetic vibration absorber with variable stiffness

Liu and Liu (2006) presented a newly designed electromagnetic vibration absorber (EMVA) with variable stiffness. This device is a non-contact, with non-mechanical motion, and the stiffness can be changed instantly. Also, different from conventional electromagnetic apparatus, the system is tunable online.

The electromagnet is constructed by winding Gauge 18 copper wire around a C-shaped steel core as shown by *Figure 21*. A dual-role permanent magnet in an Electromagnetic Variable Absorber (EMVA) serves as an absorber mass and creates a variable magnetic spring by adjusting electromagnetic coil direct current. Characterizing stiffness variation is crucial for EMVA design.

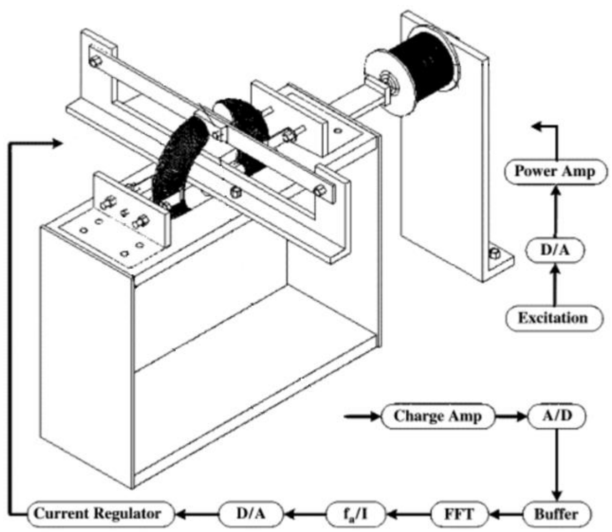

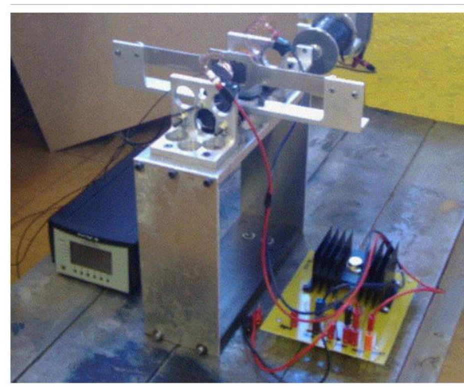

Figure 21. Electromagnetic vibration absorber with variable stiffness.

f. Tangled metal wire particles

Tangled metal wire (TMW) particles are considered as stiffness and damping elements for adjustable and semi-active vibration attenuators (Tang and Rongong, 2019). TMW particles (see *Figure 22 (a)*) are attractive as they can provide consistent performance in extreme temperature environments. The study reveals that repeatability is challenging for individual particles, but a particle collection's stiffness and damping can be largely stabilized after vibration exposure. The tuned mass damper (TMD) features a cylindrical container constraining a disc-shaped mass with TMW particles (see *Figure 22 (b)*). Device adjustment through cavity size and TMW particle compression impacted resonant behavior. Vibration tests highlighted adaptability to host structure modes. Despite the particle medium's variability, the damper's multiple internal resonances make it detuning-insensitive, allowing broad tuning range for optimal performance in critical applications amid prolonged use.

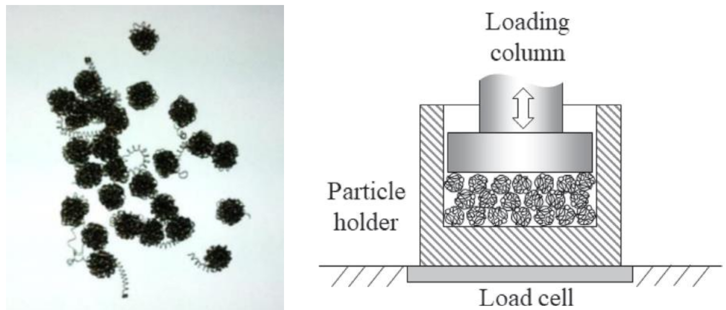

(a) (b)

Figure 22. (a) TMW samples, (b) TMW based vibration absorber.

g. Particle based semi-active dampening

Shah et al. (2011) proposed a semi-active thrust damping system, using a piston in a magnetic particle bed. Tunable damping relies on particle interactions controlled by an external magnetic field. The particle medium combines solid- and liquid-like qualities, providing wide temperature range, leak-free operation, vacuum compatibility, and system fatigue prevention. This medium is stable, cost-effective, commercially available, and user-friendly.

The designed damping system (see *Figure 23*) contains three essential components: (1) an oscillating thrust piston to transfer energy from a vibrating mass to the damping medium, (2) magnetic particles to dissipate energy and serve as tunable damping medium, and (3) an electromagnet to generate a magnetic field of desired strength. The thrust piston is a cylindrical metal rod with flat ends. It is made from either steel (12L14 carbon steel) to produce a magnetic piston or aluminum to produce a non-magnetic one. The properties of the magnetic particles and the electromagnet are presented in detail hereafter.

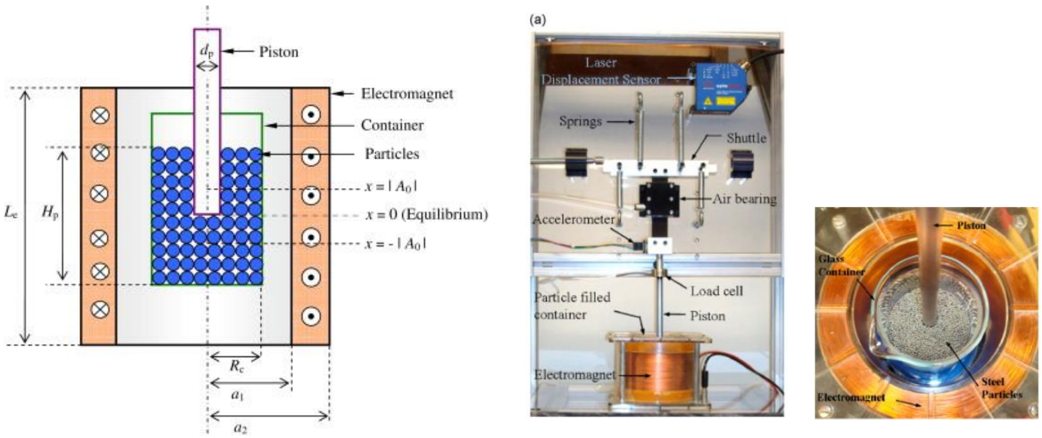

(a) (b)

Figure 23. Particle based semi-active dampening: (a) schematic model, (b) experiment setup.

Select damping medium based on magnetic, thermal, and mechanical properties. AISI 52100 chrome steel particles were chosen for large susceptibility, high-temperature resistance, and strength. *Figure 24 (a)* and *(b)* depict the steel particles and their respective responses to a magnetic field.

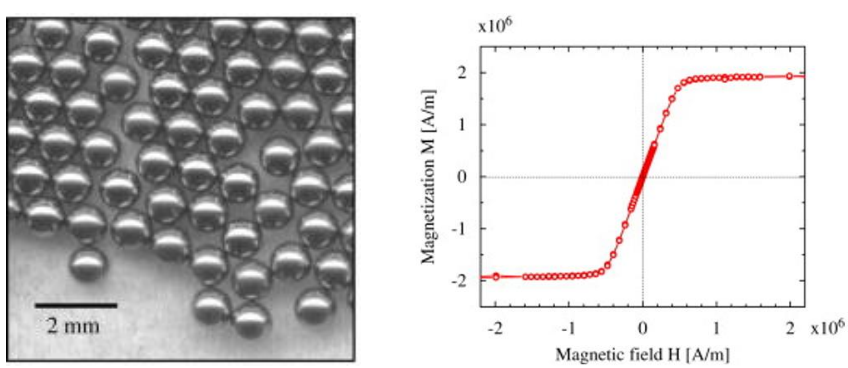

(a) (b)

Figure 24. (a) Image of 1.2 mm chrome steel particles and (b) their magnetic response to an applied field.

h. Semi-active electromagnetic torsional tuned vibration absorber

Abu Seer et al. (2019) developed a semi-active adaptive electromagnetic torsional tuned vibration absorber (ATTVA) as shown by *Figure 25*, which can be tuned to the excitation frequency by means of shunting the capacitance in the electromagnetic RLC circuit. This design will be useful in suppressing vibrations in rotary systems with variable natural frequency or excitation frequency.

Electrical capacitive shunt circuit adjusts ATTVA's apparent mass. Mechanically variable and digitally tunable capacitors are in picofarad range with limited tuning range. "Capacitor ladder" circuit with discrete capacitors, remotely controlled by low-resistance electromechanical relays, offers optimal control, avoiding undesirable circuit resistance from switches and relays.

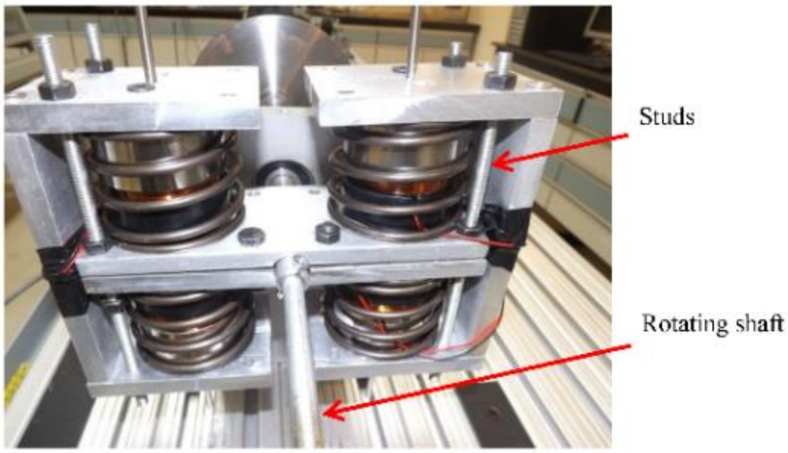

Figure 25 .The adaptive torsional tuned vibration absorber mounted on the rotating shaft.

2.4.3 Semi-active control in vehicle systems

As an example of smart mechanisms, Venhovens et al. (Venhovens et al., 1993) employed an adjustable crank to modify a mechanical lever's length, generating semi-active force to minimize vehicle roll and pitch shown by *Figure 26*.

(a)

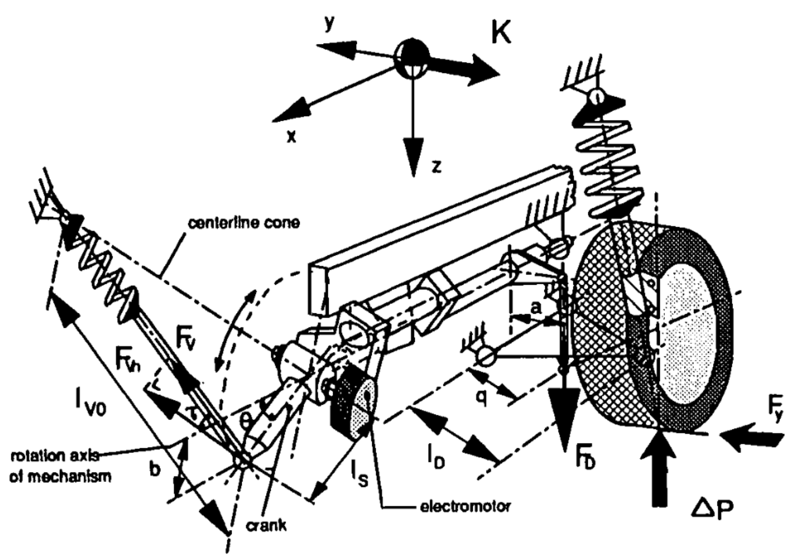

(b)

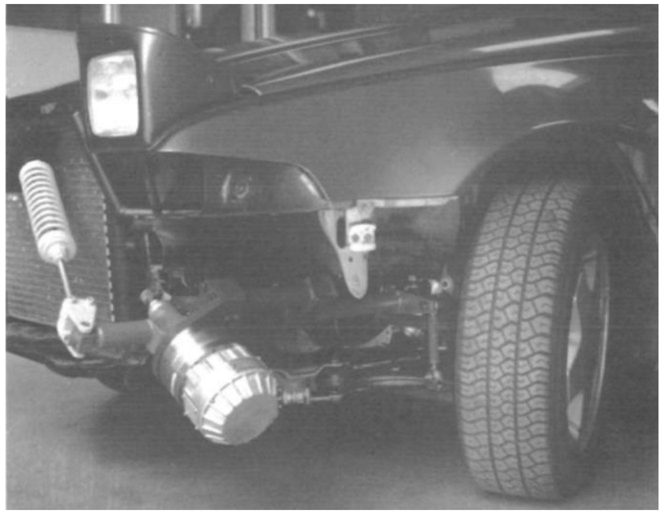

Figure 26. The cone mechanism mounted on a left front suspension: (a) schematic model, (b) implementation on a real vehicle.

With the help of a cone mechanism, a ball joint connects one end of the spring to the vehicle body, while the other end connects to an adjustable crank integrated into the transmission system. This crank's position, denoted by angle θ, is finely modulated through a linear actuator. This setup ensures that the ball joint aligns precisely with the rotation axis of the crank. Consequently, as the crank rotates, the spring's centerline traces the surface of an imaginary cone. This movement is remarkably efficient in terms of power consumption due to the perpendicular orientation of the crank's free end displacement relative to the direction of force F_V within the spring. By adjusting angle θ, the mechanical lever's length can be controlled, leading to a corresponding variation in the compensating force (F_V). The variable length of the mechanical lever, and consequently the variable compensating force can be obtained by varying angle θ. Force F_D in the push/pull rod (which connects the wishbone with the transmission mechanism) is expressed by Equation 4.

$$F_D = \frac{L_S \sin\theta}{A} f_{VN} \tag{4}$$

Another case concerns a semi-active muffler (see *Figure 27*) that operates by adjusting bypass tube count, thereby influencing sound wave interactions and phase control. This yields constructive or destructive interference by reducing noise through interference patterns. When compared to passive mufflers, the semi-active muffler technology provides substantial noise reduction performance. It excels, in particular, in the frequency band below 150 Hz, demonstrating outstanding noise reduction. In the frequency band below 350 Hz, the semi-active muffler surpasses passive mufflers in terms of average transmission loss. However, its noise elimination performance decreases significantly beyond 350 Hz.

Figure 27. The test stand for semi-active muffler device.

In a research focused on suspension system for lightweight cars, air spring and semi-active magneto-rheological fluid damper are used. By regulating the system's dynamics, a self-tuning controller successfully suppressed vibrations. Using air springs and variable stiffness dampers together, features like stability, comfort, and handling were improved. When compared to traditional controllers, the suggested self-tuning controller with an adaptive scale factor provided greater control in vehicle motion and acceleration. The study emphasized the benefits of semi-active suspension systems to increase ride quality and energy management through sophisticated components and intelligent control (Shiao et al., 2010). Generally, using air springs for semi-active control is advantageous offering a continuous range of stiffness by adjusting the volume of air (Fischer and Isermann, 2004; Guo and Zhou, 2020; Shiao et al., 2023). However, air spring systems are susceptible to air leakage (Hu, 2017), and require several utility systems such as the air reservoir, pipeline, and control valve which makes the control system complicated (Chen et al., 2021; Mendia-Garcia et al., 2023).

Using piezoelectric-based energy harvesters resulted promising effects for semi-active vibration control in a passenger car. Through experimentation, a commercial harvester was optimized using Variational Feedback Control (VFC) for adaptive impedance. Urban car vibrations caused by rough roads, engine, and bumps were harnessed by piezo harvesters. The experimentation resulted in a 2.8mW power output from a single piezo-beam, showcasing a maximum power density of 140mW/kg. *Figure 28* shows the possible the test setup including the vehicle, feedback accelerometers and the piezoelectric beam. The authors recommended to have a balance among weight, power yield, and control intricacy for an optimal design.

Figure 28. Test setup for semi-active control of vehicle vibration using piezoelectric beam.

However, the study is limited to vehicle speeds up to 40 km/h which restricts the vibration frequency range. In fact, realizing an effective wide-band performance requires the employment of a periodic array of transducers (Casadei et al., 2010; Gripp and Rade, 2018; Lossouarn et al., 2016) which reduces the system’s degree of reliability. Additionally, the irregular surfaces found in optimized industrial components hinders the appropriate attachment of all transducers within a well-ordered array.

Incorporating magnetorheological semi-active absorbers to enhance vehicle NVH performance is a feasible solution (Guo et al., 2004; Stelzer et al., 2003; Xin et al., 2017; Zhang et al., 2006). Developing a magnetorheological elastomer-based semi-active absorber resulted in a remarkable decrease in powertrain vibration by tuning the absorber's natural frequency (Xin et al., 2017). Additionally, utilization of magnetorheological fluid in a semi-active suspension system for vehicles led to a considerable reduction of up to 50% in both vertical and rocking acceleration (Zhang et al., 2006). Despite the mentioned advantages, magnetorheological isolators have shortcoming in stroke and resonance shifting capabilities(Daniel Christie et al., 2021; Komatsuzaki et al., 2016), restricting their usage to narrow-band and low-energy vibrations, which do not meet vehicle noise requirements.

A recent approach is to utilize metal rubber (MR) whose adaptive properties and semi-active vibration control performance for mechanical transmission systems were demonstrated recently (Rieß and Kaal, 2021; Soleimanian et al., 2023). MR material is a metal wire mesh with a stiffness level as low as rubber, which can be controlled by altering the material porosity through compression. Moreover, a wide range of damping is also achievable since changing porosity affects the degree of frictional contacts among individual metal wires (Xiao et al., 2018; Xue et al., 2020; Zhang et al., 2015). Due to this specific damping mechanism, the damping feature is almost insensitive to excitation frequency (Hong et al., 2013). Because of their strong relative resilience to degradation in extreme environments and their wide operating temperature range metal rubbers are preferred over their elastomeric counterparts (Jin et al., 2019; Rieß and Kaal, 2021).

2.4.4 Metal Rubber

Metal rubber materials, also referred to as "metal cushion" or "wire mesh," have recently emerged as potential components for shock and vibration cancellation (Jiang and He, 2014). Metal rubber is a type of tangled metallic mesh manufactured via a process of wire-drawing, weaving and compression molding (Zhang et al., 2013).

Although some author prefer the words "entangled metallic wire material “entangled metallic wire material” (Tan and He, 2012) or “metallic mesh” (Wang et al., 2010), the term metal rubber stems from the similarities between the characteristics of MR and those of an elastomeric rubber. The unique properties of high elasticity, damping, reliability, and adaptability to the operational environment make it a strong competitor to synthetic elastomer.

Metal cushions are available in a variety of forms and sizes that are fitted to certain requirements. These components, regardless of their shape, serve as spring masses capable of withstanding a broad range of loads without affecting their mechanical characteristics. They function as effective dampers, dissipating energy from vibrations and shocks and releasing it as heat through internal sliding friction between the knitted mesh wires (Hong et al., 2013). This friction is produced by the different types of interaction among metal wires. The typical contact status and corresponding fraction of contact wires in MR solids is demonstrated by *Figure 29*. There are three groups of wires in the MR solid that can interact with one another during compression: (a) non-contact, (b) slipping (involving relative motion in the transverse direction), and (c) sticking (both microsprings move in an identical manner).

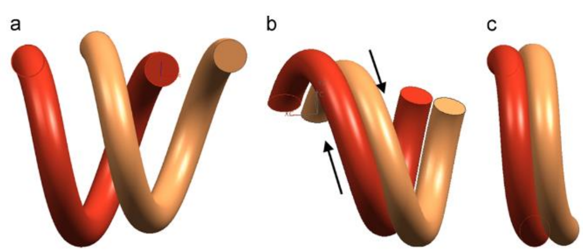

Figure 29. Different interaction modes during compression of MR solid: (a) non-contact, (b) slipping and (c) stick.

When the MR solid is compressed, or the relative density increases, some slipping wires change their interaction mode (Hong et al., 2013; Zhang et al., 2013). Based on the theoretical model, the stiffness of the wire assembly increases when the contact status changes, while the energy dissipated decreases. *Figure 30* shows the typical contact status and percentage of contact wires in MR solids. When the MR solid is compressed or the relative density increases, slipping wires move to a different interaction state, reducing the overall number of slipping micro-elements and energy dissipation. The percentage of wires in stick contact status increases, leading to a higher tangent modulus at higher densities.

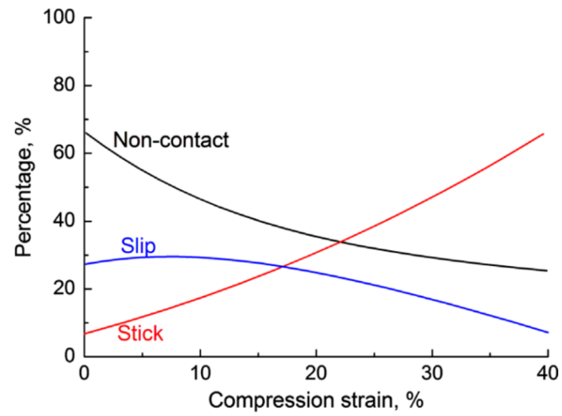

Figure 30. Variation of contact percentage with compression strain.

Hong et al. (2013) proposed a mass micro-spring model (*Figure 31*), to estimate the load-deflection behavior of MR material. By evaluating the loading for each micro spring represented in *Figure 31*, the load-deflection behavior for each mode can be calculated from the effective stiffness in each direction.

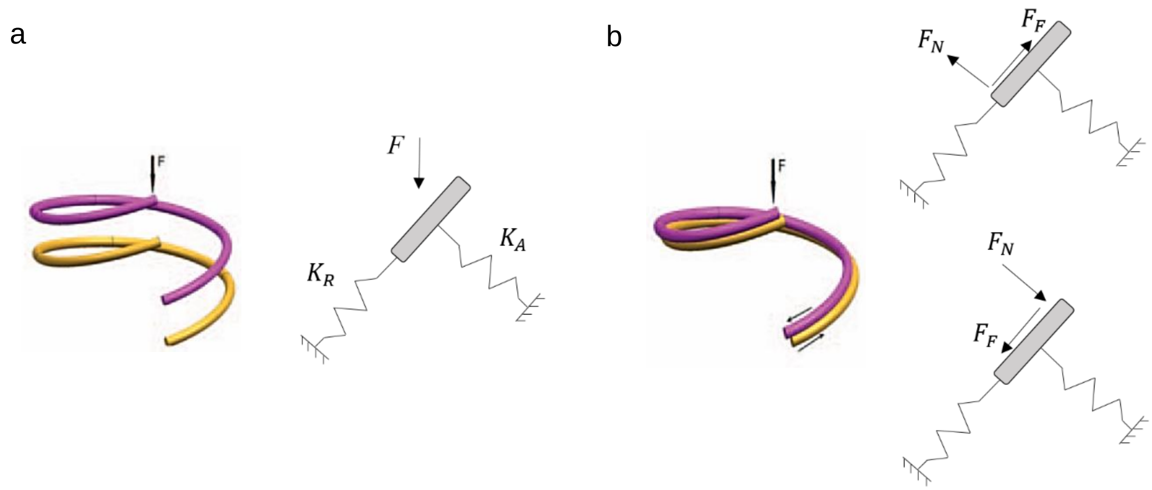

Figure 31. mass micro-spring model for each mode of wires interaction: (a) non-contact, (b) with contact (slipping, or sticking).

For the non-contact mode, one micro-spring carries the full load. When it is positioned such that its axis is aligned at an angle *α* to force *F*, the deflection is

$$\Delta L = F\left(\frac{\cos^2\alpha}{k_A} + \frac{\sin^2\alpha}{k_R}\right) \quad (5)$$

where F corresponds to the applied load, k_A and k_R represent the axial and radial coefficients of stiffness, respectively. When the springs are in contact, the load is shared equally between each micro-spring. For the sticking condition, this gives

$$\Delta L = \frac{F}{2}\left(\frac{\cos^2\alpha}{k_A} + \frac{\sin^2\alpha}{k_R}\right) \quad (6)$$

For the slipping mode, the force–deflection relationship is different for loading and unloading. For loading in the direction shown in *Figure 31*, the relationship can be given by

$$\Delta L = \frac{F\cos\alpha - F_N}{k_A}\cos\alpha + \frac{F\sin\alpha - F_F}{k_R}\sin\alpha \quad (7)$$

where F_F, and F_N denote the frictional and normal components of loading.

The concept of using metal cushions to address engineering challenges was first patented by Metal Textile Corp, in 1958, focusing on load resistance, vibration mitigation, and shock absorption (Pérez et al., 2020). Subsequent patents (Ulanov and Bezborodov, 2016; Xiao et al., 2018) explored applications of metal cushions in hose or pipe clamps, as well as the development of calculation procedures utilizing the Finite Element method (FEM) to analyze damping supports made of metal cushions for pipelines.

A metal rubber embedded coating is designed and evaluated for vibration dampening of pipeline in high temperatures. As shown by *Figure 32*, through a cladding ring, the metal rubber is applied to the exterior of the pipe as the damping layer. Hence, the structure which consists of a damping layer and a hanger, serves as a shock absorber for the pipeline system.

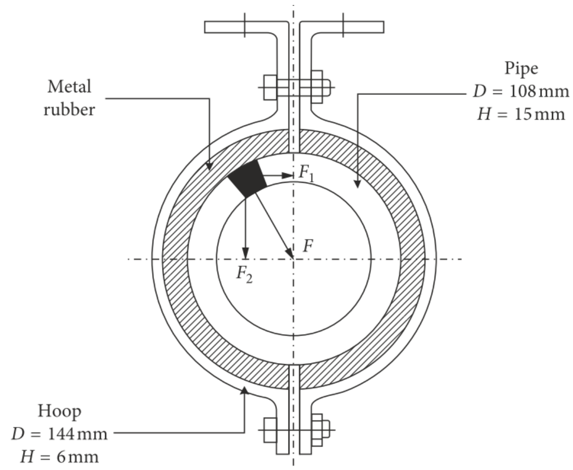

Figure 32. Scheme of the metal rubber coating.

In this regard, a theoretical approach (Xiao et al., 2018) based on the bilinear hysteresis model is adopted to study the damping effect of the cladding layer. The accuracy of analytical model is verified through experiments. Some parametric studies are conducted including the impact of various factors, such as cladding layer density, number of coating layers, and excitation magnitude, on the vibration absorption characteristics. Consequently, the results demonstrated that the damping performance of metal rubber decreases with higher forming density but increases with more cladding layers and greater excitation magnitude. The research provides a solid theoretical and experimental foundation for addressing vibration reduction in pipeline systems and offers valuable insights for future studies in the field of vibration damping for high-temperature pipelines. The findings have practical implications for engineering applications and can guide further research efforts in this area.

Cao et al. (Cao et al., 2023) reported an improvement of the damping performance of MR engine mounts by developing a mathematical model to predict the relationship between the mounting stress, strain, and strain rate of the metal rubber. In *Figure 33*, stress and strain in the metal rubber mount concentrate near the component and the bolt area. To analyze further, dynamic loading tests were conducted vertically.

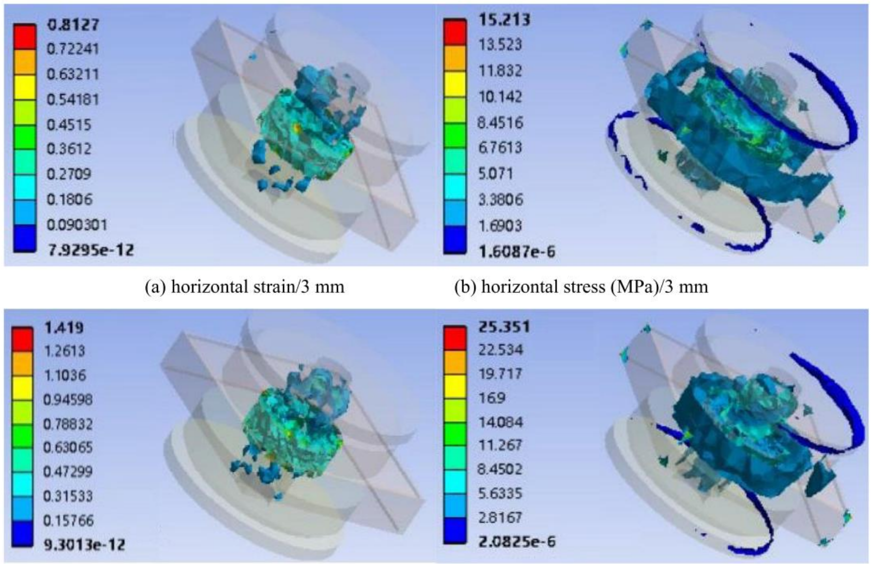

Figure 33. Stress and strain distributions in the horizontal direction of the MR mounts.

Figure 34 shows stress and strain isograms during engine vibration, indicating symmetrical changes between upper and lower metal rubber parts. Vertical strain is less than horizontal due to greater height, resulting in predominant vertical stress. However, dynamic loading in the vertical direction exhibits stress changes similar to the horizontal, yet stress in the vertical direction doesn't uniformly transfer across the entire metal rubber mount.

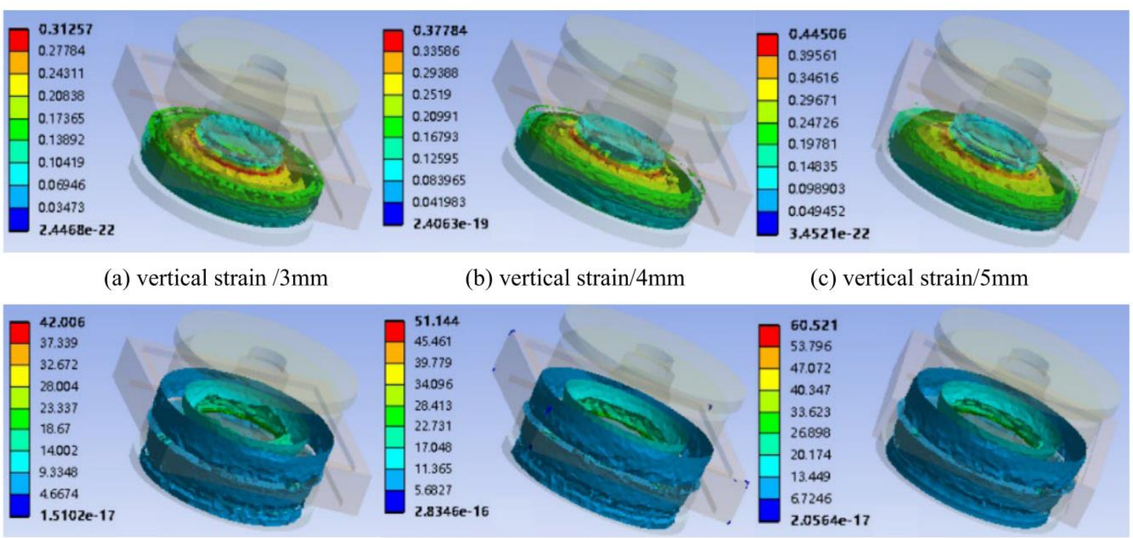

(d) vertical stress (MPa)/3mm (e) vertical stress (MPa)/4mm (f)vertical stress (MPa)/5mm

Figure 34. Stress and strain distributions in the vertical direction of the MR mount.

The last important finding was that the stress-strain behavior of metal rubber mounts is frequency independent, as shown in *Figure 35*, whereas higher excitation frequencies result in larger areas enclosed by the spatial hysteresis curve, indicating frequency-dependent variations in both the curve and the spatial hysteresis surface.

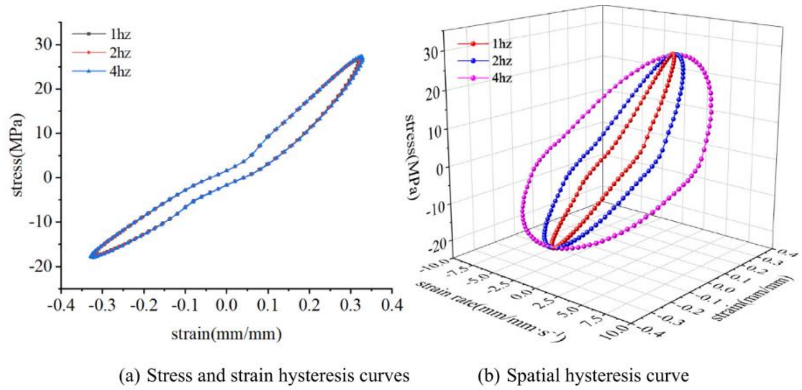

Figure 35. Metal rubber mounts stress–strain hysteresis curve.

Despite the high energy dissipation rate of MR material, thermoplastic elastomers have been found as serious competitors for them. One study (Yang et al., 2021) enhanced underwater vehicle power plant vibration isolation by designing three new types of isolator using ring metal rubber, magnesium alloy, and modified ultra-high polyethylene (MUHP).

The power plant vibration isolator system, depicted in *Figure 36*, includes a load, vibration isolators, and an aluminum thin-walled cylindrical shell housing. The load is an aluminum solid cylinder matching the housing's length. Initial isolators are divided into front and rear compositions, each comprising 6 evenly arranged metal rubber vibration isolation elements (see *Figure 36*).

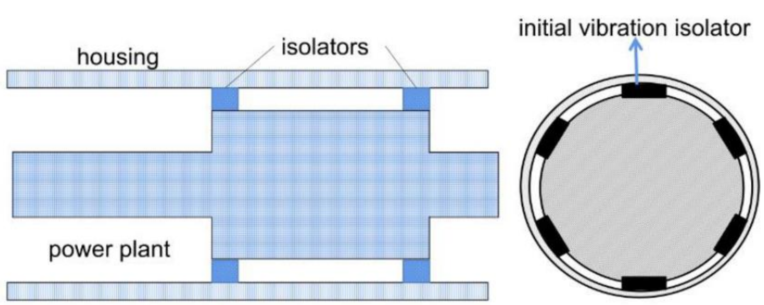

Figure 36. Schematic diagram of the dynamic vibration isolation device.

Figure 37 illustrates the insertion losses for three vibration isolator types. The ring metal rubber isolators exhibit 3–5 dB effectiveness at 1–1.5 kHz but decrease with increasing frequency. Magnesium alloy isolators show low insertion loss, with negativity around 1 kHz and vibration amplification in the 1.5–2 kHz range. In contrast, MUHP demonstrates significant and stable vibration isolation (3–5 dB) within the interest frequency band, improving with frequency. Compared to initial isolators, MUHP excels in insertion loss, while metal rubber isolators match, and magnesium alloy isolators display insignificant isolation with vibration amplification.

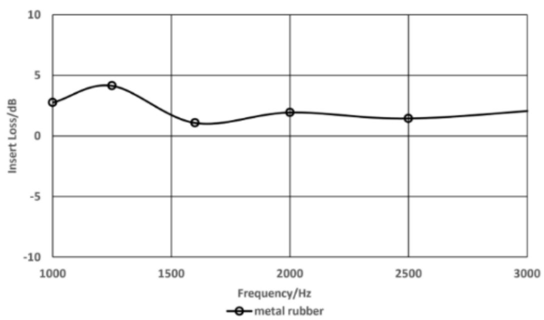

(a) Metal rubber

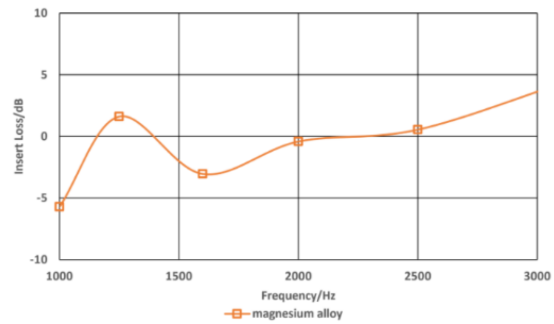

(b) Magnesium alloy

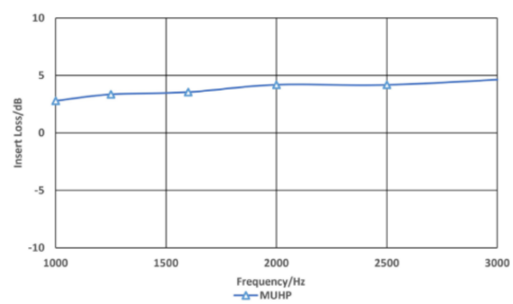

(c) MUHP

Figure 37. Insertion losses of the three new isolators.

According to the above comparison, MUHP outperforms the initial design significantly in insertion loss. Metal rubber isolators match initial effectiveness, whereas magnesium alloy isolators show insignificance and vibration amplification.

Ma et al. (2023) proposed an improved sampling method based on the surrogate model method and then optimized the structure of metal rubber isolators to the applicable standards of metal rubber isolators. The optimization configuration, validated against finite element simulation, exhibited high accuracy. An improved Latin hypercube sampling method, ensuring flexibility in generating samples, outperformed LHS and GA-LHS methods in uniformity and efficiency. The combination surrogate model optimization strategy enhanced accuracy and stability, surpassing single surrogate models and existing strategies. The single-objective model reduced response acceleration by 21.62%, 16.31%, and 17.75%, and mass by 0.87%, 4.45%, and 3.19%. The multi-objective model introduced weight coefficients, achieving a Pareto optimal set for response acceleration and mass.

Ma et al. (2013) explored the mechanical behavior of a damper design utilizing metal rubber particles (MRP) within an auxetic (negative Poisson's ratio) cellular structure. The auxetic structure is shown by ***Error! Reference source not found.*** *(a)*. T he auxetic damper is constructed using an anti-tetrachiral honeycomb configuration, with the cylinders filled with MRP material.

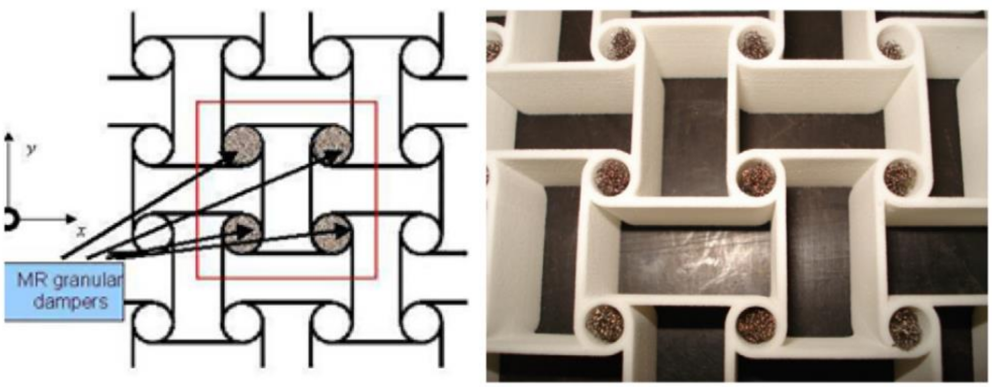

Figure 38. Anti-tetrachiral honeycomb structure with embedded MRP.

Quasi-static loading was applied to MRP samples to assess stiffness and loss factor by analyzing the static hysteresis curve. An experimental investigation was conducted to examine the influence of relative density and filling percentage on the static performance of MRP, aiming to establish the basis of design for optimal utilization of MRP devices. Additionally, the study presented an experimental evaluation of the integrated auxetic-MRP damper concept, employing static and dynamic force response techniques.

Figure 39 showed the frequency response under various single sine exciting forces. Only one global natural frequency (around 40 Hz) can be observed within the 0–1000 Hz frequency bandwidth. There are no apparent effects on the natural frequency given by increased force loading on the anti-tetrachiral panel without the metal rubber particles.

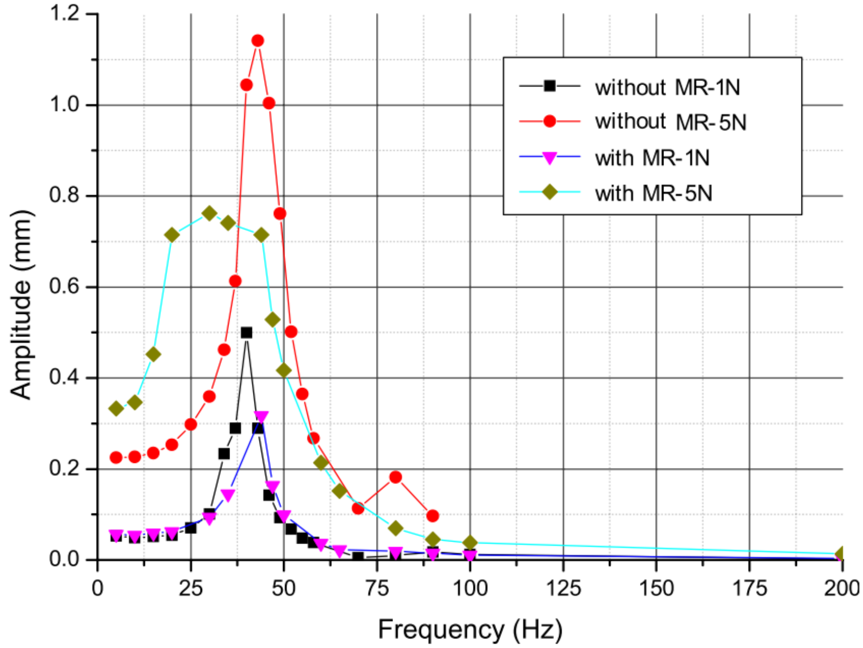

Figure 39. Amplitude–frequency curves.

Rieß and Kaal (2021) proposed a frequency-adaptable tuned mass damper (FATMD) utilizing MR material as adjustable stiffness elements. These cushions' dynamic characteristics in terms of stiffness and damping were experimentally investigated, demonstrating their nonlinear behavior resembling adjustable springs.

Pre-compression of cushions notably influences the stiffness and damping properties of the FATMD, allowing precise control of its resonant frequency. In *Figure 40*, transfer function curves depict this effect at 0.03 g input amplitude, with magnitude and phase curves on the left and right, respectively. Both measured and model data are presented, illustrating an increase in pre-compression from top to bottom.

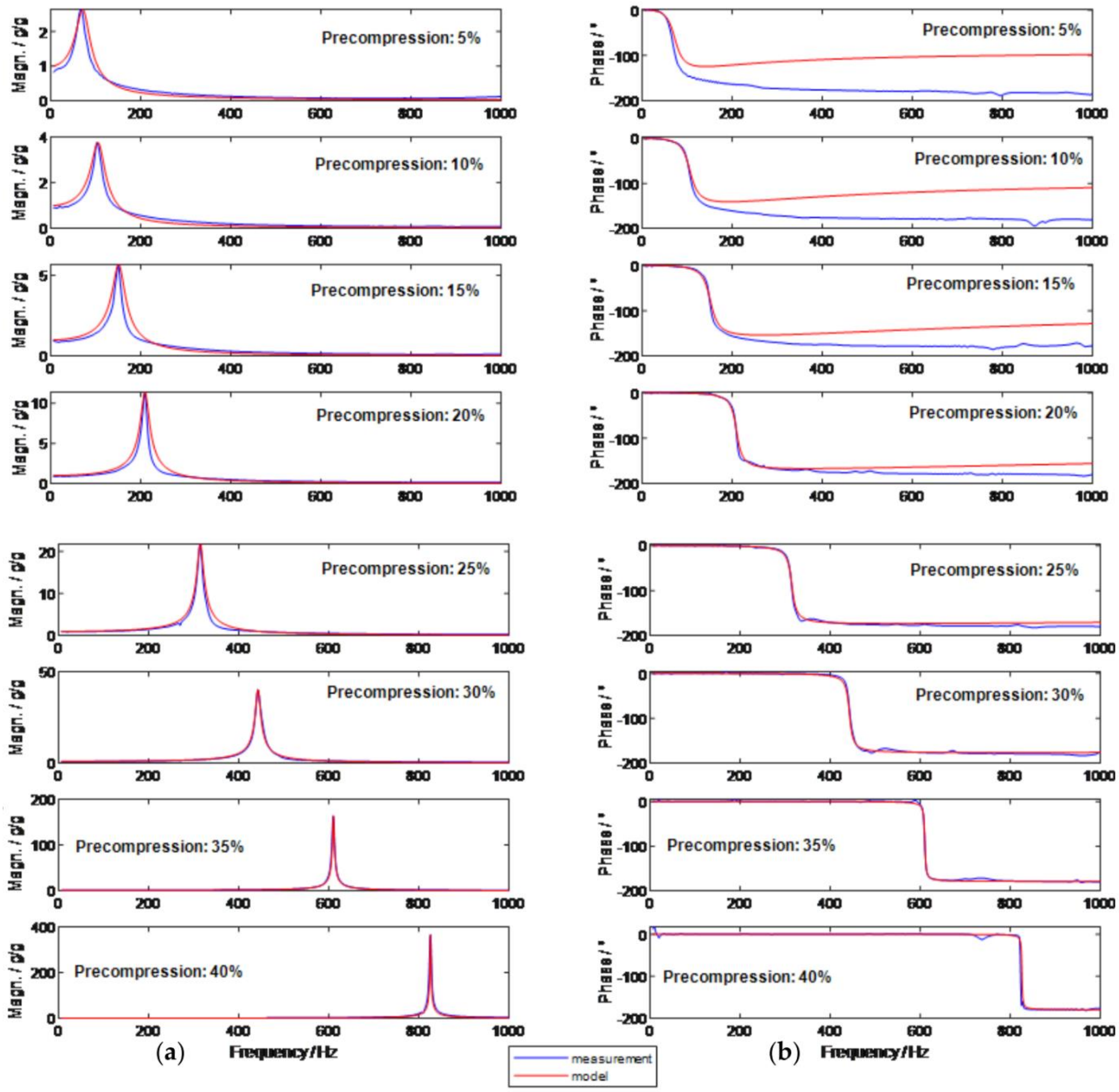

Figure 40. Magnitude (a) and phase (b) of frequency response at increasing pre-compressions.

The FATMD's natural frequency was found to be influenced by the pre-compression of the metal cushions, allowing an adjustable frequency range of 67 to 826 Hz. Increasing pre-compression heightened stiffness while reducing damping, quantified using a viscous mass damper model. The FATMD's behavior remained consistent across varying input amplitudes. Compared to elastomers, metal cushions revealed advantages in terms of stability, geometry, and fixation. The FATMD was approximately modeled by a simple spring-damper oscillator, albeit discrepancies due to complex internal damping within metal cushions. Further research is recommended to refine mathematical models for the cushion behavior. The versatile FATMD exhibited low dependency on amplitude, broad frequency range, and high damping ratio, suggesting its practical potential. Additional experiments with various excitation signals and cushion types are suggested for deeper insights.

The present research technology is basically inspired by the work by (Rieß and Kaal (2021). The frequency adaptability, durability, and lightweight property of metal rubber are the main reasons to choose this material for the current study semi-active control. In section 3, the selection and design procedure for the MR-based isolator is explained in detail.

Chapter 3: Methodology

3.1 Chapter organization

In this chapter, the methodology to design and apply a semi-active vibration control is explained in details. A novel semi-active vibration control technique is proposed for mechanical transmission systems. The semi-active isolator has been designed by implementing MR material whose adaptive stiffness and damping properties play the key role in control. The adaptive properties of MR material are proved by a previous study, but the present research investigates the effect of this feature on the structural response and designs an MR-based semi-active vibration controller for industrial application. For this purpose, the semi-active isolator is optimally tuned using experimental harmonic test results. The tuning levels have become reachable using a linear actuator which compresses the MR sample.

The experiments are carried out in phases A, B and C. Phases A, and B have been carried out in Adaptronica sp. z o.o. Poland. While, phase C is conducted in UNINA, Italy. For this reason, different instruments and devices have been used for measurement and control. It is noteworthy that the measured quantities and design parameters, as a consequence, exhibit differences from one another.

Phase A is devised and performed to assess the effect of MR material adaptive properties on the structural response using a simple structure with known dynamic response. Phase B is devoted to evaluate the effectiveness of the semi-active vibration isolator to attenuate vibrations in a mechanical transmission system. The mechanical transmission system is a plate accommodating a bearing and a shaft with the possibility to introduce several angles of excitation. In fact, exciting the shaft with different angles mimics the variable force vector imposed on the shaft due to the variable mesh stiffness during gears' operation in a transmission system.

Phase C is dedicated to assess the efficiency of the semi-active control used for a vehicle transmission system. For this purpose, a particular automotive transmission component—precisely, a plate dedicated to accommodating bearings—has been selected as the focus of research to control its noise and vibrations. The vibrations and noise have been intended to be isolated in a plate housing the main gearbox shafts. So that propagation of vibration wave to the other components can be somewhat prevented.

It is noteworthy to emphasize that within the framework of this doctoral program, an investigation in an alternative technological domain is being pursued. It is focused on the application of piezoelectric shunt circuits for the purpose of semi-active noise control. An extended abstract pertaining to this study can be found in Annex 1.

3.2 Formulating the semi-active vibration isolation system

Dynamic transmission systems are usually protected by thin-walled shell structures. In such structures, the main eigenmodes of vibration are out-of-plane ones. To isolate out-of-plane types of vibration, normal attachment of vibration isolator to system surface is required as shown by *Figure 41*. So that, it can contribute in out-of-plane stiffness and damping properties effectively. To introduce the semi-active concept, the isolator is enhanced by MR material which offers stiffness $\tilde{k}$ and damping $\tilde{b}$ properties variable with pre-compression rate *C* given by Eqs. (8) and (9).

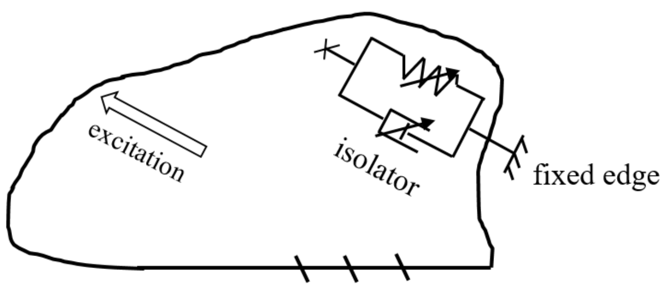

Figure 41. Schematic model for a vibration system integrated with semi-active isolator.

$$\tilde{k} = \tilde{k}(C) \quad (8)$$
$$\tilde{b} = \tilde{b}(C) \quad (9)$$

The dynamic force equilibrium equation of the structure integrated with the semi-active vibration isolator is presented by Eq. (10).

$$[M]\{\ddot{q}\} + [\tilde{B}]\{\dot{q}\} + [\tilde{K}]\{q\} = \{P\} \quad (10)$$

where [M] is the mass matrix, and [$\tilde{B}$] and [$\tilde{K}$] are variable damping and variable stiffness matrices of the vibratory system assembled with their counterparts of the MR based isolator, respectively. Moreover, {q} is displacement vector, and {P} is the out-of-plane harmonic excitation.

3.3 Optimal design of isolator, and semi-active control function

In this thesis, design of the semi-active control scheme is carried out based on optimization algorithms which use experimental data. It means parametric studies are conducted to obtain the effect of pre-compression level on the response. Therefore, the design criteria which could be the structural response amplitude, or sum of squared amplitudes will be considered for minimization with the help of optimization algorithms. Two optimization algorithms are introduced in this respect as follows: (1) point by point optimization, and (2) band optimization.

By applying the point-by-point optimization, the design criteria can be minimized frequency by frequency. Considering the design criteria function v, its values can populate a matrix according values of frequency and material pre-compression levels as expressed by Eq. (11). The optimization algorithm searches for the optimal pre-compression level corresponding to the minimum design criteria (v_{min}) ,which is less than but not equal to its reference value (v_{ref}) expressed by Eqs. (12) and (13). The reference design criteria (v_{ref}) is obviously defined as the design criteria response without any isolation treatment.

$$[v]_{f\times c} = \left[v_{f_i c_j}\right] , \qquad i \in [1, (f_{max} - f_{min})/f_{step}] , j \in [C_{min}, C_{max}] \tag{11}$$

$$\forall f \ \exists \ v_{min} \,\&\, C_{opt} \tag{12}$$

$$v_{min} = \begin{cases} v_{f_i c_j} & v_{f_i c_j} < v_{ref} \\ v_{ref} & v_{f_i c_j} \geq v_{ref} \end{cases} \tag{13}$$

On the contrary, the band optimization consists in the minimization of the area under the velocity-frequency response curve. Considering n frequency bands of Δf length, a piece-wise integration over the frequency yields the parameter, u_i, given by Eq. (14). The total value of the area under the design criteria response curve in the whole frequency range is expressed by Eq. (15).

$$u_i = \int_{f_i}^{f_i + \Delta f} v \, df \tag{14}$$

$$U = \sum_{i=1}^{n} u_i \tag{15}$$

The optimization procedure is defined by Eq. (16): the optimal pre-compression level corresponds to the minimum of the *u* values which must be less than a reference value u_{ref}. u_{ref} is a reference value corresponding to the *U* function without any isolation treatment.

$$u_{min} = \begin{cases} u_{ic_j} & u_{ic_j} < u_{ref} \\ u_{ref} & u_{ic_j} \geq u_{ref} \end{cases} \tag{16}$$

In sum, the optimization procedure can be conducted following the flowchart given by *Figure 42*.

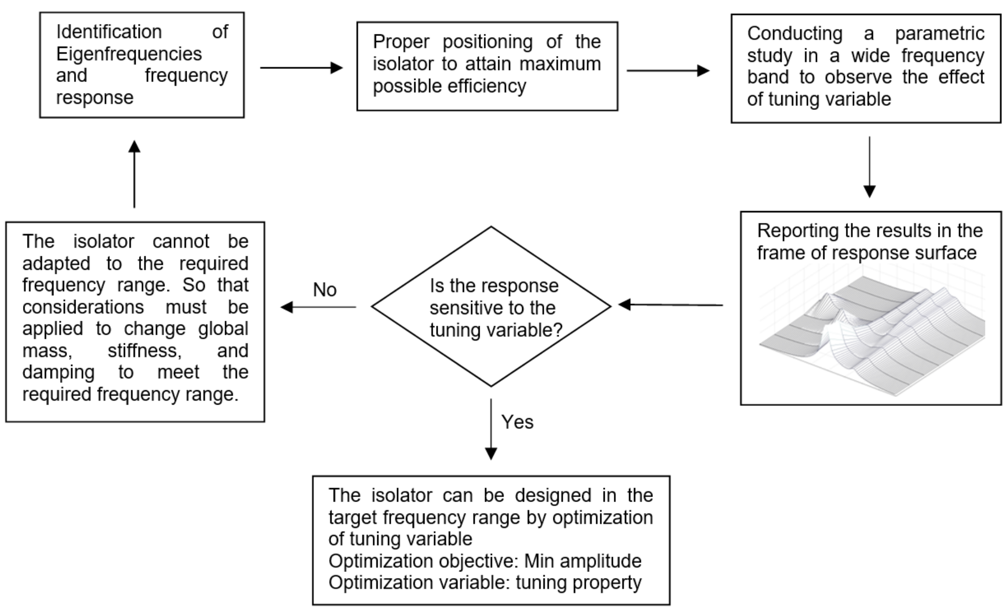

Figure 42. Optimal design procedure for the vibration isolator.

As a basic example to achieve an initial insight to point-by-point and band optimization, consider two tuning levels relevant with a vibration isolator. The frequency response corresponding to tuning levels 1 and 2 is provided by red and green colored lines given by Figure 43. Applying the point-by-point technique, the algorithm searches for the minimum values of amplitude frequency-by-frequency. Accordingly, the optimal response will be the line noted marked by - -. As can be observed, the peaks appeared in tuning levels 1 and 2 can be eliminated by this optimization algorithm. So that the optimal control path is {level 2, level 1, level 2, level 1}. However, the band optimization compares the possible tuning levels in a particular frequency band with respect to the integral of the design criteria. Considering two frequency ranges of [0, f_1] and [f_1, f_2], and taking the under the curve area as the design criteria, result of optimization aligns with tuning level 1 shown by **...** . It means the band optimization algorithm chooses the tuning level 1 response as the optimal response. Although the resulted optimal response offers lower vibrations, it is not the best. Hence, the best optimization performance can be achieved by considering proper and smaller frequency ranges for optimization.

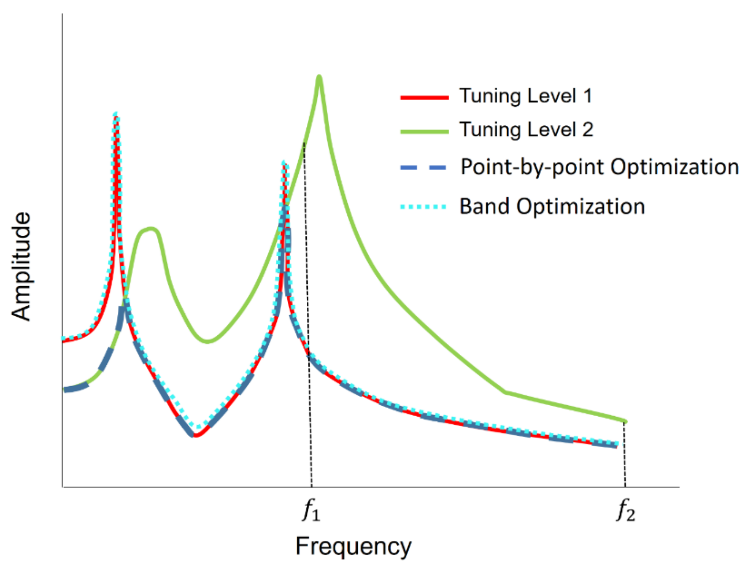

Figure 43. A basic example demonstrating the concept of point-by-point and band optimization algorithms.

The optimal control function, consisting of *n* frequency intervals set to optimal pre-compression rates C^{op}, can be determined by solving the optimization problem. So that the semi-active frequency-based control function C_{sa} can be represented by Eq. (17).

$$C_{sa} = \sum_{i=1}^{n} \left(C_i^{Op} - C_{i-1}^{Op}\right) H(f - f_i) \tag{17}$$

where *H* denotes the Heaviside function (N. Felder and M. Felder, 2015). In addition, f_i is the starting frequency of the i^{th} frequency interval. Each frequency interval corresponds to an optimal control level obtained through the optimization process. So that what determines the size of each interval is the response status with respect to the tuning variable.

3.4 Experiment phases

Three main phases are defined to conduct experiments. The first phase aims to investigate the potential of MR rubber adaptive behavior on structural response control as explained in section 3.4.1. The second phase is designed to assess the effectiveness of the optimal semi-active control for vibration isolation of a bearing host plate explained in section 3.4.2. The third phase is dedicated to evaluate the efficiency of the optimal semi-active control to damp vibration in a vehicle transmission system. In this phase both open-loop and closed-loop strategies are adopted.

3.4.1 Phase A: cantilevered plate

To have a proper understanding of the effect of adaptive properties of MR material on structural vibration response, a cantilevered steel plate with dimensions and material properties given by Table 1 is considered for a forced vibration test. So that the MR material is compressed by different rates using a linear actuator achieving different stiffness and damping levels. The effect of isolator on the system vibration can be determined by investigating *U* parameter and the shift in natural frequencies. Thus, the purpose of phase A is to gain confidence in the feasibility of adaptive structural control through an MR based isolator.

Table 1. Dimensions and material properties of the cantilevered plate.

Dimensions (mm)			Material Properties	
Length	Width	Thickness	Young's modulus (GPa)	Poisson's ratio
450	300	3	210	0.3

3.4.2 Phase B: bearing host plate

The objective of this part is to design a semi-active control scheme. In this regard, a fixed edge steel plate subjected to bearing-induced vibrations is considered. The flowchart of design procedure is given by *Figure 44*. The first step, parametric studies, refers to a set of experiments required to record the structure response for a range of pre-compression rates. The excitation is applied with an angle of 45° to guarantee equal loading components. The second step is to find the optimal pre-compression levels based on the optimization criteria. The third step is finding the optimal control function and building an automatic open-loop semi-active scheme upon that. The last step is the employment of the control scheme in vibration tests forced by an excitation in frequency range of interest to assess its effectiveness. Since the control scheme is built upon the optimization of results per 45° angle of excitation, it is conservative enough to be applied for different ratios of loading components.

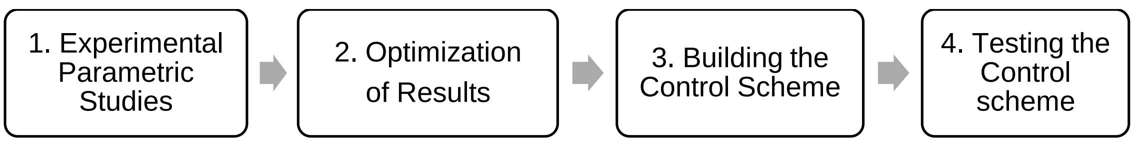

Figure 44. Flowchart showing the necessary steps for designing the semi-active control.

The plate dimensions for this phase of experiment is provided by Table 2.

Table 2. Dimensions of the bearing host plate.

Dimensions (mm)		
Length	Width	Thickness
420	270	3

To evaluate the influence of loading components on the effectiveness of the present control scheme, several vibration isolation tests are conducted. In this respect, the exciting shaker can be properly positioned to excite the shaft by angles of 0°, 30°, 45°, 60°, and 90° degrees as illustrated by *Figure 45*. So that the magnitude of imposing load can be described as follows.

$$F = \overrightarrow{F_1}\, cos\, \theta + \overrightarrow{F_2} \sin\theta \quad (18)$$

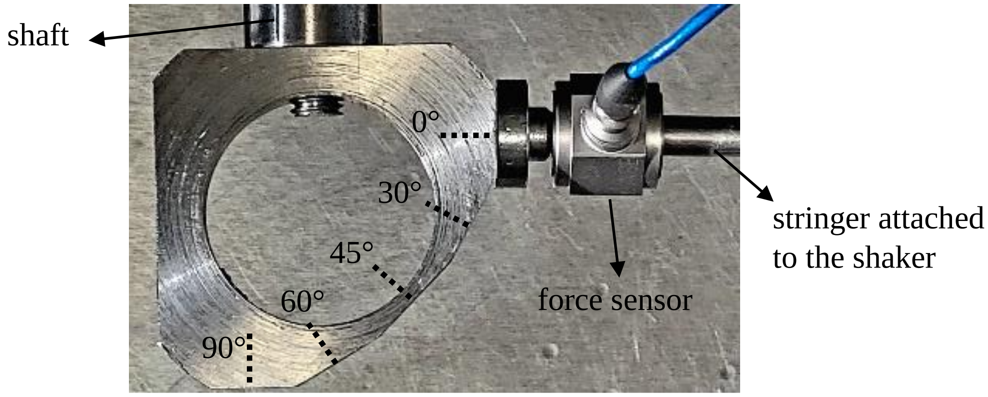

Figure 45. Different θ angles devised for introduction of loading components contribution.

3.4.3 Phase C: vehicle transmission system

The imperfect transfer of motion in gears is mainly attributed to geometrical deficiencies, manufacturing tolerances, deviations in the gear manufacturing process, and elastic deflections that occur under operating conditions. All of them lead to variations in the gear mesh excitation force, i.e. transmission error. The gear mesh excitation transmits to the housing through the shaft and bearing, causing structural vibration and radiated noise (see *Figure 46*), which is known as gear whining noise. This noise subsequently propagates all over the transmission housing and finally into the surrounding air (Koronias et al., 2011; Son et al., 2020; Wang et al., 2016; Wu and Wu, 2016). As indicated by *Figure 46*, bearings play a critical role in transmitting vibrations and structure-borne noise from the rotary system to the stationary housing. This, isolating vibrations as close as possible to bearings can help prevent its propagation to the rest of the structure.

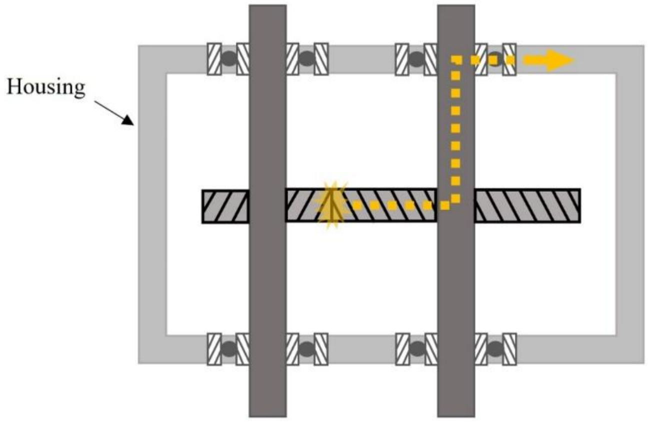

Figure 46. Noise transmission path initiated mainly at the gear mesh interface.

Figure 47 shows an explosion view of a manual transmission casing of a passenger car. The red-colored plate (gearbox plate 4467941) (Auto-Car, 2023) is the target component for vibro-acoustic control. This plate houses two sets of bearings corresponding to the transmission input and output shafts.

The main objective in targeting this plate structure is to effectively isolate vibrations at the plate level to decrease the transmitted vibration energy to the rest of housing and, consequently, reduce noise.

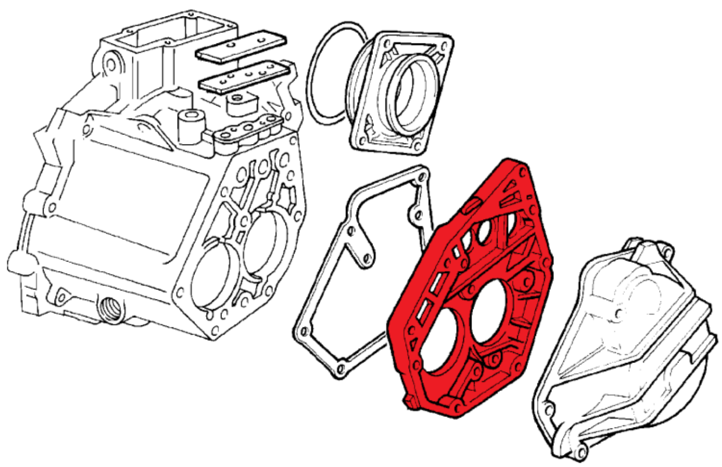

Figure 47. An explosion view of a passenger car's transmission casing.

The plate edge is fixed through six circumferential bolts. An isolator enhanced by MR material with adaptive stiffness and damping properties is attached to the plate in normal direction as shown by *Figure 48*. The effectiveness of the isolator to attenuate noise and vibration depends on a proper tuning of its features according to the excitation frequency.

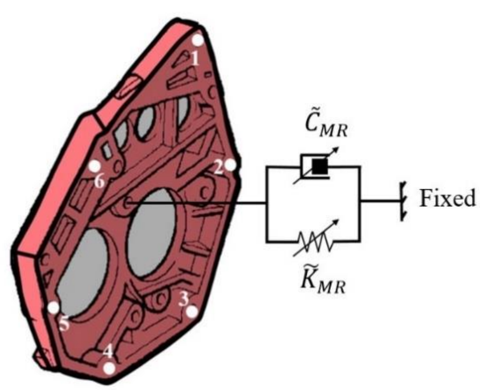

Figure 48. Dynamic model for the transmission plate associated with the semi-active vibration isolator.

The research project involved multiple phases: A, B, and C. Phases A and B were conducted in Poland at Adaptronica sp. z o.o., while Phase C was carried out in Italy at the UNINA. Due to these distinct labs, different measurement instruments, control facilities, measured quantities, and the design criteria parameter (v) were adopted for each phase.

3.5 Control Strategies

The semi-active control can be applied in practice by adopting an open-loop, or closed-loop control strategy. Implementing an open-loop control strategy necessitates a precise optimization of tuning at specific frequency intervals, delineated by the observation of attenuation in response peaks. This control strategy relies on a linear rise of frequency with respect to time dictated by a constant frequency sweep rate defined. Accordingly, the frequency-based control function can be used for a given excitation in an assigned experiment time, *t*. Thus, the open-loop semi-active control function C_{sao} can be expressed as offered by Eq. (19).

$$C_{sao} = \sum_{i=1}^{n} \left(C_i^{Op} - C_{i-1}^{Op}\right) H(t - t_i) \tag{19}$$

where t_i is a starting time for a typical time interval with an optimal control level.

On the other hand, the closed-loop control can be applied by identification of the change in harmonic mode shapes. Considering the definition of node and antinode from the theory of stationary waves (Halliday et al., 2013; Rao, 2011), the harmonic mode shape is a natural mode or a transition between several natural modes in resonant and non-resonant frequencies, respectively. As given by Eq. (20.1), the absolute amplitude of response at an arbitrary point (e.g., blue point in *Figure 49*) on the structure is either consistently bigger or consistently smaller than another one (e.g., red point in *Figure 49*) at a particular harmonic mode Φ_i. Therefore, if the congruent inequalities become incongruent, it signals the change in the mode shape ($\Phi_i \neq \Phi_{i-1}$) as given by Eq. (20.2).

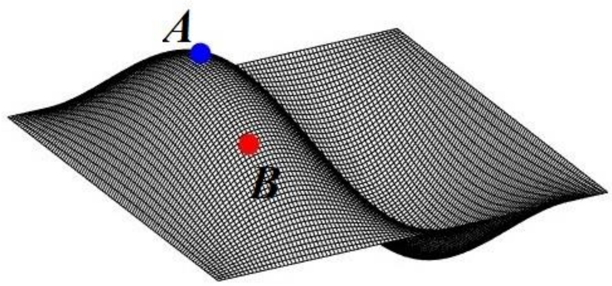

Figure 49. The relative position of points in a vibration mode.

$f_s \leq \forall f_i \leq f_e$:

$$-\Phi_i = \Phi_{i-1} \quad \{(v_A)_i > (v_B)_i \;\&\; (v_A)_{i-1} > (v_B)_{i-1} \;or\; (v_A)_i < (v_B)_i \;\&\; (v_A)_i < (v_B)_i\} \tag{20.1}$$

$$\Phi_i \neq \Phi_{i-1} \quad \{(v_A)_i > (v_B)_i \;\&\; (v_A)_{i-1} < (v_B)_{i-1} \;or\; (v_A)_i < (v_B)_i \;\&\; (v_A)_i > (v_B)_i\} \tag{20.2}$$

Thus, the closed-loop semi-active control function C_{sac} can be represented as given by Eq. (21).

$$C_{sac} = \sum_{i=1}^{n} \left(C_i^{Op} - C_{i-1}^{Op}\right) H^*(\Phi - \Phi_i) \tag{21}$$

where Φ_i corresponds to the i^{th} harmonic mode shape corresponding optimal control level. Therefore, the parametric format of the open-loop and closed-loop control functions (see Eqs. (19) and (21)) is analogous; however, they can be distinguished by the size of optimization frequency intervals, and the optimal pre-compression levels consequently.

In this research, the identification of changes in harmonic mode shape is carried out by using a pair of synchronized micro-machined accelerometers (MMAs). By finding the correlation between the absolute response amplitudes of the MMAs, it becomes possible to generate appropriate feedback, thereby facilitating the operational sequence of the control loop as depicted in *Figure 50*. This method offers two key advantages: first, it offers a robust closed-loop control by eliminating the need for computationally intensive online fast Fourier transform calculations. Second, it allows for harmonic mode identification using cost-effective MMAs, rather than expensive piezoelectric accelerometers. Thus, this approach is particularly beneficial for testing in vehicle industry due to its relative robustness and economic features. The closed-loop strategy, unlike the open-loop one, relies on harmonic mode rather than time, making it ideal for semi-active control during real-world conditions, spanning from zero to full acceleration drives or reversed.

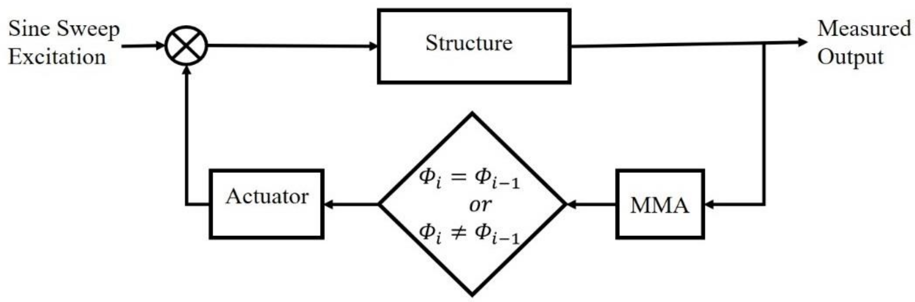

Figure 50. Closed loop control based on identification of harmonic mode shape.

3.6 Selection of installation and measurement point on the structure

Vibration mode shapes play a key role to position the vibration isolator properly. So that the maximum vibration reduction rate can be attained if the isolator can be positioned near the antinodes corresponding to a larger number of eigenmodes. Targeting a large number of eigenmodes is challenging when it comes to higher modes of vibration. So that in this condition, attachment of the isolator can be found effective if it is positioned close to the antinodes corresponding to eigenmodes with high effective mass. The effective mass M_{eff} can be related to participation factor γ as provided by Eq. (22).

$$M_{eff,i} = \gamma_i^2 \tag{22}$$

The mode participation factor can be obtained a follows

$$\gamma_i = \{\Phi\}_i^T[M]\{D\} \tag{23}$$

where vectors Φ, M, and D refer to mode shape, mass matrix, and excitation direction vector, respectively (Ansys® Academic Research Mechanical, Release 18.1, Help System, Modal Analysis Guide, ANSYS, Inc., n.d.). The eigenmode shapes and effective mass ratio can be obtained by solving the dynamic problem with the help of numerical simulation. In this study, the numerical model is built using the finite element software, ANSYS®. Then, an important point worth noticing is the investigation of elastic wave propagation with respect to the installation position. So that it can be observed to what extent the vibration wave can be transmitted which is of great significance in mechanical transmission systems.

3.7 Control Design and Measurement Settings

3.7.1 Control Setup and Measurement Configuration for Phases A and B

To generate vibrations, a shaker applies a sine sweep force, 25 mm and 100 mm far from the cantilevered plate free vertical and horizontal edges, respectively. The control devices include (a) measurement instruments, and (b) actuation devices as depicted by .

A laser vibrometer for measuring velocity, a dynamic force sensor to measure excitation force variation, and a National Instruments (NI) reading card for recording and collecting data are required for measurement.

An MR sample, a linear actuator, a DPDT relay supplied by a power source, and an NI writing card are necessary for the actuation tasks. The linear actuator embedded with a hall sensor is dedicated to control the compression rate of metal rubber (Silentflex ref. no.: 990000H27E (Silentflex, 2023)) to change the control state and achieve different stiffness and damping levels.

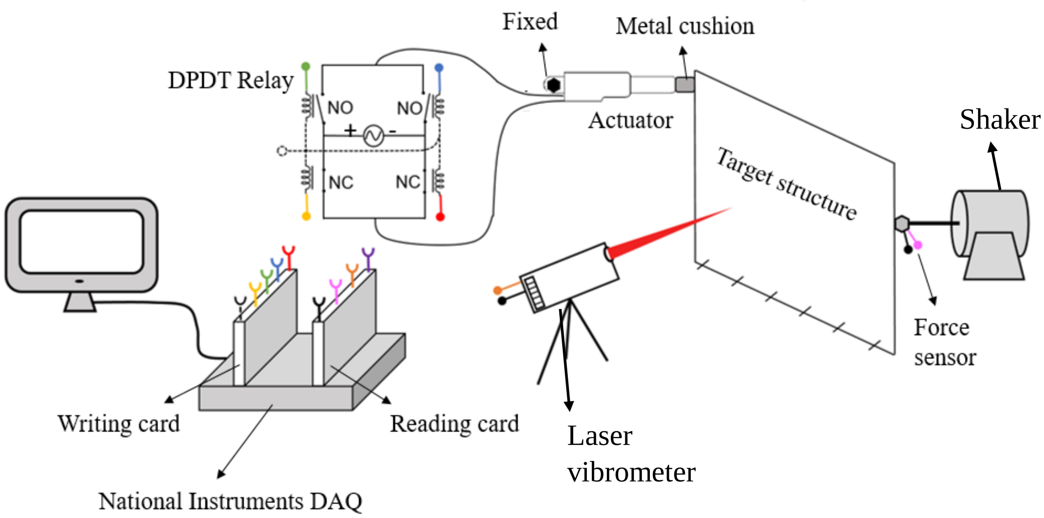

Figure 51. Schematic representation of the automatic open-loop semi-active control experiment setup.

The MR sample hysteresis behavior is provided by *Figure 52*. Minimum and maximum static loads are reported 50 kg and 600 kg, respectively. The maximum permissible dynamic load equals to 1800 kg.

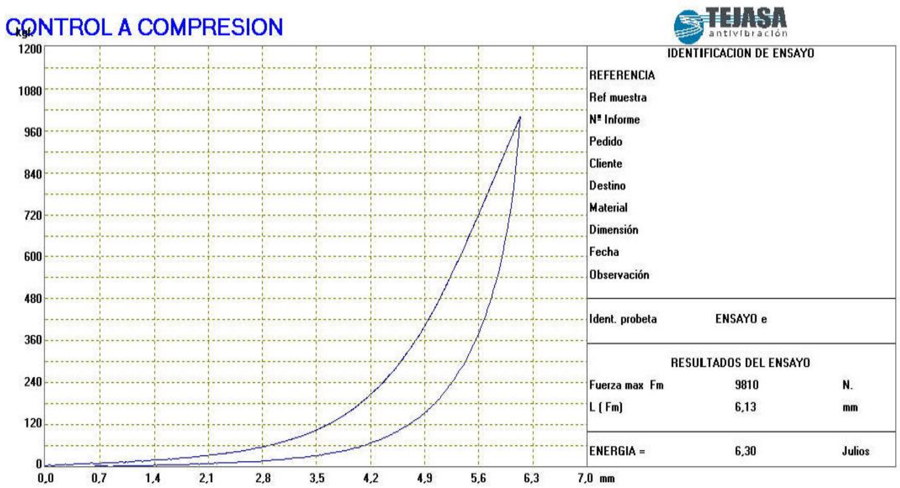

Figure 52. Hystersis behavior of Silentflex MR sample (ref. no.: 990000H27E).

To control the actuator motion, a DPDT relay is employed which can change the polarity and create three states of extension, contraction, and stop. To generate motion steps, the hall sensor measures the piston position and attains the ideal position through a feedback control program. All reading and writing tasks are programmed in LabVIEW program.

3.7.2 Control Setup and Measurement Configuration for Phase C

To apply the semi-active control, a control circuit including a RPI 4 microcomputer, a multi-channel relay, and a 24 Volt power amplifier is designed as shown by *Figure 53.* The RPI 4 oversees writing extension, contraction, and stop commands to the actuator, as well as reading the MMAs' responses following I2C protocol for the closed-loop control. See Annex 2, Figure 1 for the relevant schematic circuit.

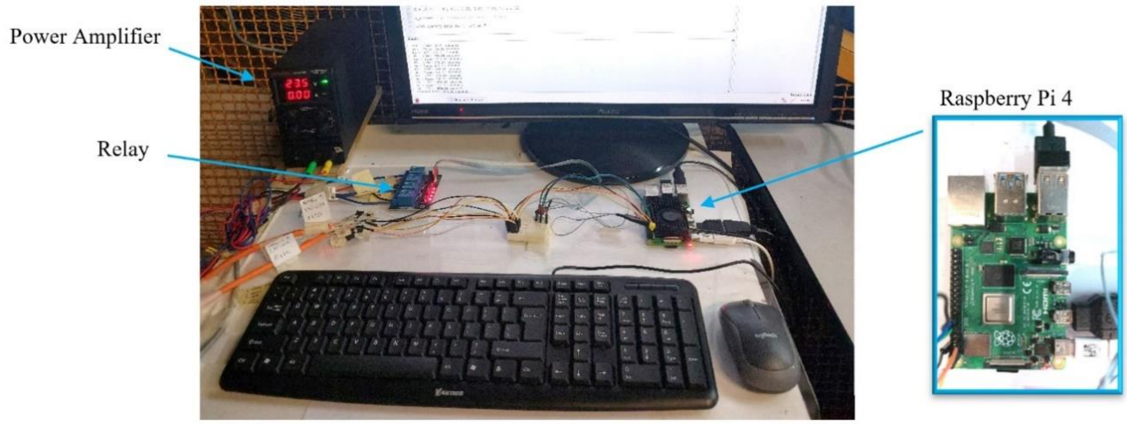

Figure 53. Control circuit for semi-active control.

Vibration acoustic measurements were performed to evaluate the semi-active control, where the transmission plate was excited with a sweep rate of 5 Hz/s during harmonic testing. The test covered of 1000 to 3750 Hz. Vibration measurement is conducted using PCB accelerometers (PZAs) (*Figure 54 (left)*), while noise measurement is conducted using a pressure-pressure sound intensity probe (SIP) (*Figure 54 (right)*). In the current acoustic test, excitation and measurement are conducted using two independent Siemens LMS SCADAS hardware units, with the semi-active isolator controlled by a RPI 4 microcomputer. In contrast, vibration tests utilize a single Siemens LMS SCADAS hardware for both excitation and measurement processes. The reason for this difference in test setup is that the acoustic measurement software module is unable to define a sine-swept excitation signal.

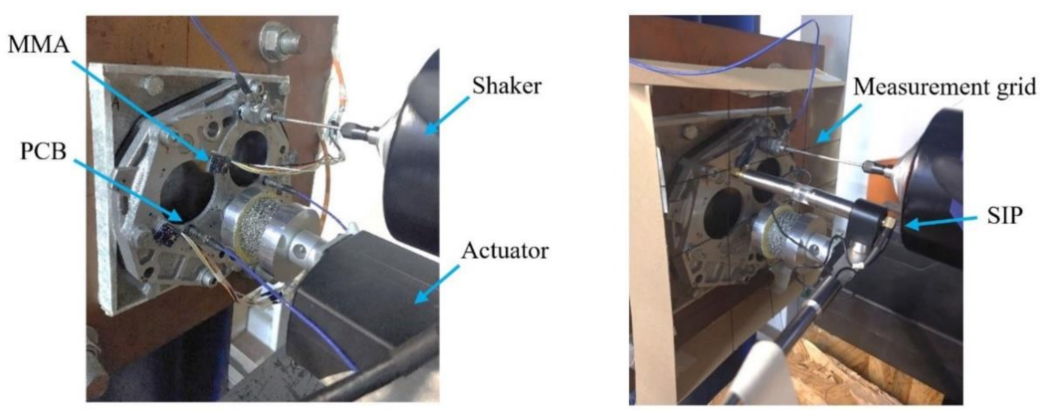

Figure 54. Measurement setup: (left) vibration measurement, (right) noise measurement.

The effectiveness of the control strategy to isolate vibrations is examined by comparing the cumulative response across the entire frequency range A_E given by Eq. (24) for control and without control scenarios.

$$A_E = \sum_{i=1}^{n} A_{(\Delta f_i)} \tag{24}$$

To assess the control effect on noise level, the radiated power *W* is an important metric which can be calculated based on integrating the measured sound intensity *I* over the closed surface *S* as given by Eq. (25) (Hickling et al., 1997; Klaerner et al., 2015). Hence, the control effectiveness for noise suppression can be determined by comparing this important metric with and without control.

$$W = \oint_S I \, ds \tag{25}$$

The sound intensity itself is recorded in normal direction to the surface at discrete points on a grid (illustrated by *Figure 54 (right)*), where each point is the representative of an acoustic element. Therefore, by applying Eq. (25), the radiated power can be derived within the frequency domain, thereby enabling the visualization of a noise map at distinct frequencies (Batel et al., 2003; Petrone et al., 2014).

Chapter 4: Results and Analysis

4.1 Chapter Organization

This chapter reports the results of three phases of research explained in chapter 3. The potential of MR material for adaptive structural control is demonstrated in phase A. In addition, the results of semi-active vibration control are reported in phases B and C. The results include both vibration, and acoustic response with and without (w/o) control in a wide range of frequency.

4.2 Results of Phase A (cantilevered plate)

The natural frequencies for the cantilevered plate bolted on the longer edge are reported in Table 3. A close agreement is achieved among the present results and those given by reference (Nagino et al., 2008).

Table 3. Natural frequencies obtained for the cantilever plate compared with reference.

Mode no.	Natural Frequency (Hz)		
	Numerical (present)	Experiment (present)	Reference (Nagino et al., 2008)
1	28.24	26.28	28.30
2	51.66	47.03	51.70
3	116.96	112.13	117.02
4	177.47	163.83	178.02
5	209.47	196.30	210.00
6	254.40	253.08	255.00

The corresponding deformation contour plots obtained through numerical simulation are shown in *Figure 55*. It can be deduced from results that the two free corners of the cantilevered plate participate in all harmonics moving either in-phase or anti-phase.

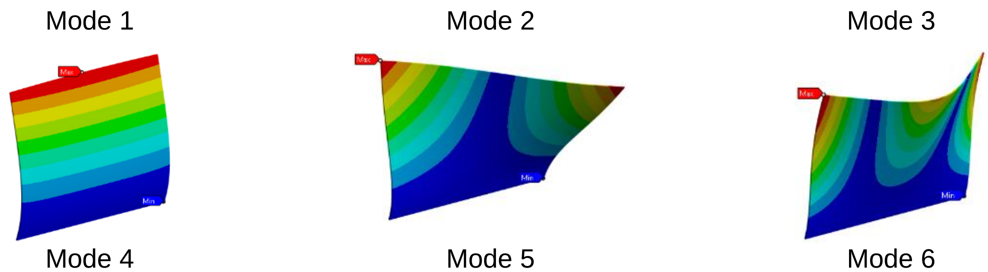

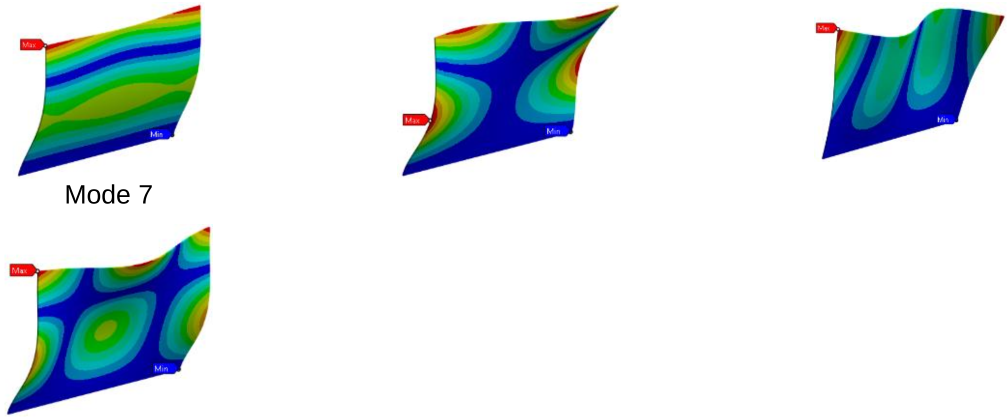

Figure 55. Deformation contour plot of the cantilevered plate for the studied eigenmodes.

In the next step, the effect of the MR –based isolator on structural behavior of the cantilevered plate is studied. The isolator is attached at a free corner to contribute maximally to displacement reduction as shown in *Figure 56*. The shaker applies a sine sweep force 25 mm and 100 mm far from the plate free vertical and horizontal edges, respectively (see *Figure 56*).

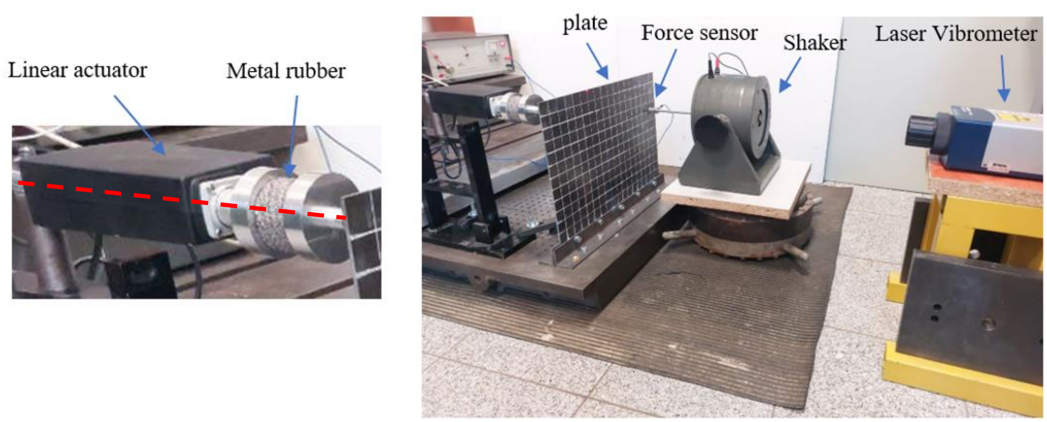

Figure 56. Vibration test setup of the cantilevered plate controlled by the MR–based isolator.

The relationship between piston displacement and MR sample compression rate is presented in *Figure 57*. The MR sample compression is not linear with the applied actuator load which means it gets compressed to a lower extent than the piston's movement. This effect is caused mostly by the elastic deflection that occurs at the plate's free corner where the isolator is attached. As can be observed in the diagram, the compression of the MR material is substantially smaller as compared to the displacement of the piston. In fact, the piston displacement of 3 mm is a turning point where for values below 3 mm, the stiffness of MR is noticeably greater than the plate stiffness. While for displacement values of bigger than 3 mm, the stiffness of MR slightly decreases. This phenomenon is an important aspect which should be considered in the implementation of MR-based isolators requiring precise control of mechanical motions.

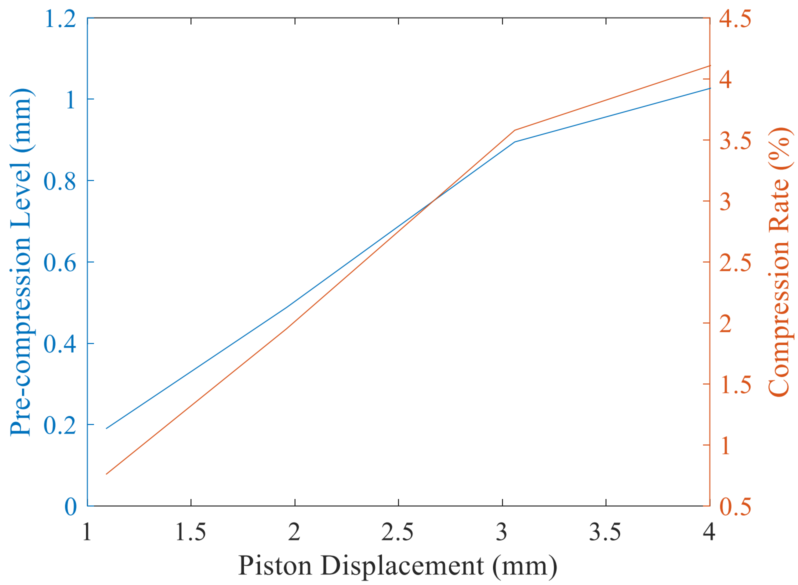

Figure 57. Relationship between the pre-compression rate and piston displacement.

The vibration level averaged along the free edge for four levels of pre-compression rate (*C*) corresponding to 1 mm, 2 mm, 3 mm, and 4 mm displacement of actuator piston, is presented in ***Error! Reference source not found.***. It can be inferred that t he MR-based isolator is tuneable to the eigenmodes within the studied frequency range. The isolator influences the response by changing both the amplitude level, and number of resonances. The isolation method reduces all large-amplitude resonances except the first one, which is adversely affected by pre-compression rates of 0.76% and 1.95%. The number of resonances with isolation is obviously larger than without isolation case due to absorption of energy.

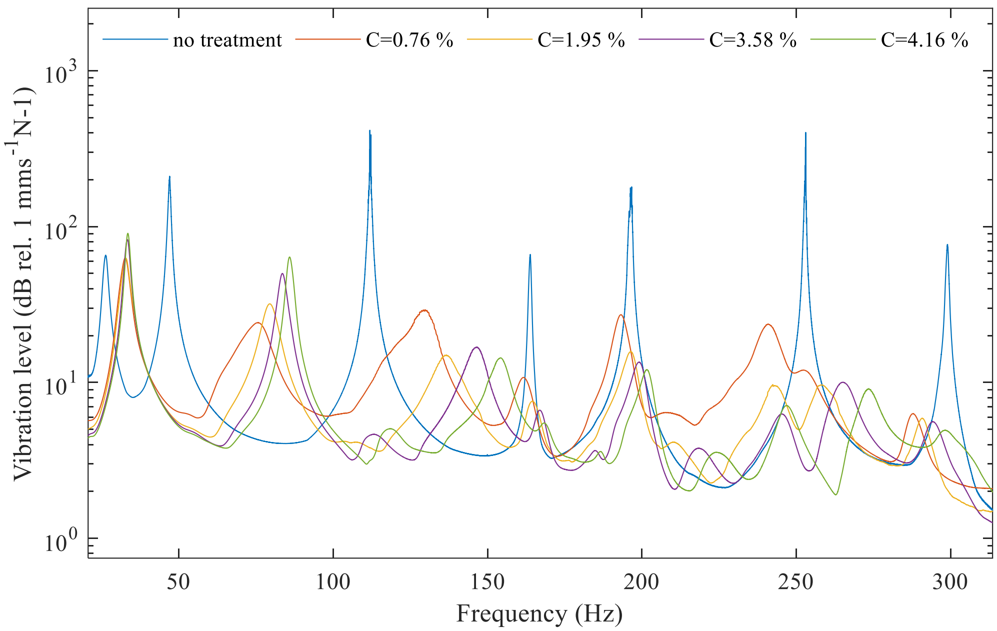

Figure 58. Vibration levels for different pre-compression rates obtained by harmonic test

The vibration response is also estimated using FEM considering Shell and Spring elements for the cantilevered plate and the isolator, respectively. First of all, the response for the without treatment case is approached to the experiment response by carefully relaxing the boundary conditions. As shown by *Figure 59*, a particular percentage of plate edge is constrained to introduce partial fixation.

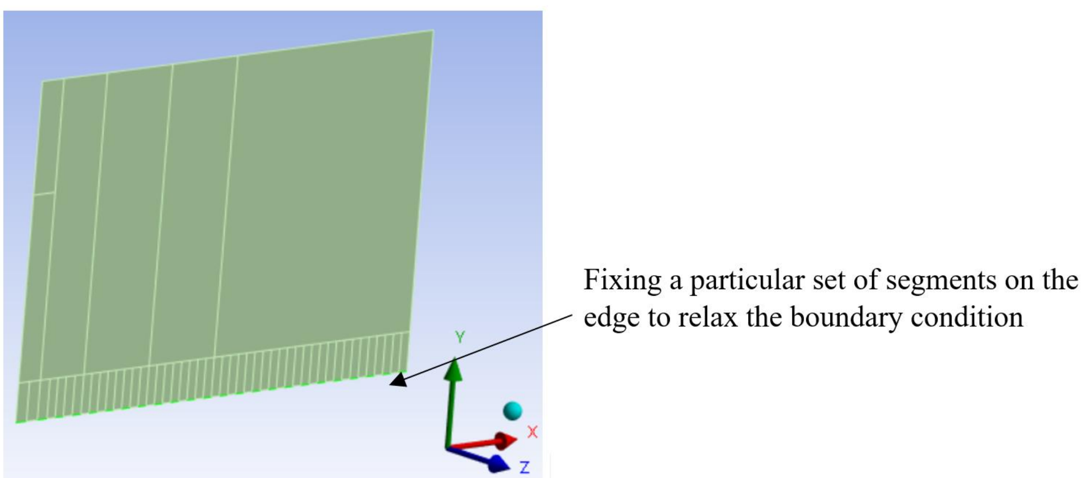

Figure 59. Relaxing boundary conditions to approach the experiment eigenfrequencies.

According to the graph given by *Figure 60*, the 26% curve is accepted.

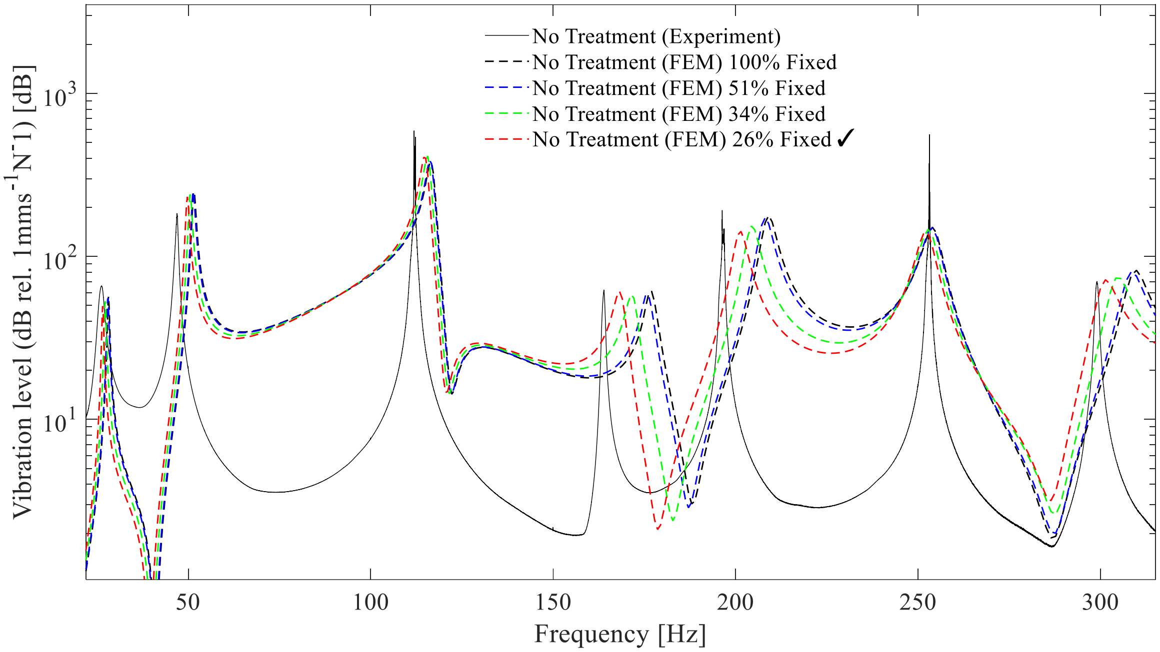

Figure 60. Comparing experiment and FEM results for the without treatment case considering different percentage of edge fixation.

the stiffness and damping of metal rubber is a function all components in series on the line of action noted by dashed red line in *Figure 56*, not only the MR sample. Hence consideration must be applied to estimate the stiffness and damping properties in order to achieve a meaningful insight regarding the experimental results.

Given the inverse relationship between damping and stiffness in metal rubber with respect to pre-compression level, compressing the material leads to increased stiffness but reduced damping (Rieß and Kaal, 2021). The metal rubber is represented using a spring element (Link element), and based on the mentioned relationship between stiffness, damping, and pre-compression rate, two finite element models are developed, incorporating appropriate values for directional stiffness (kL) and directional damping (dL). The Finite Element Method (FEM) results reveal that pre-compressing the metal rubber predominantly shifts the peaks to the right and downward.

The results are presented in *Figure 61*. If we interpret the effects of stiffness and damping as absorption and dissipation, respectively, the study confirms that the absorption achieved through pre-compression is more influential than the decrease in damping. In other words, the contribution of stiffness, which divides the initial peaks into multiple shorter peaks, surpasses the impact of reduced damping feature. by pre-compressing the metal rubber, effective absorption and dissipation of vibration energy are achieved, confirming its potential for utilization in a semi-active mode, as elaborated in phase B. Another noteworthy observation is the numerical results are more closed to the experiment at lower frequencies (≤ 200 Hz) than higher frequencies. Moreover, the higher number of observed peaks in experimental results compared to numerical results, attribute to the higher complexity of the actual structure integrated with the isolator.

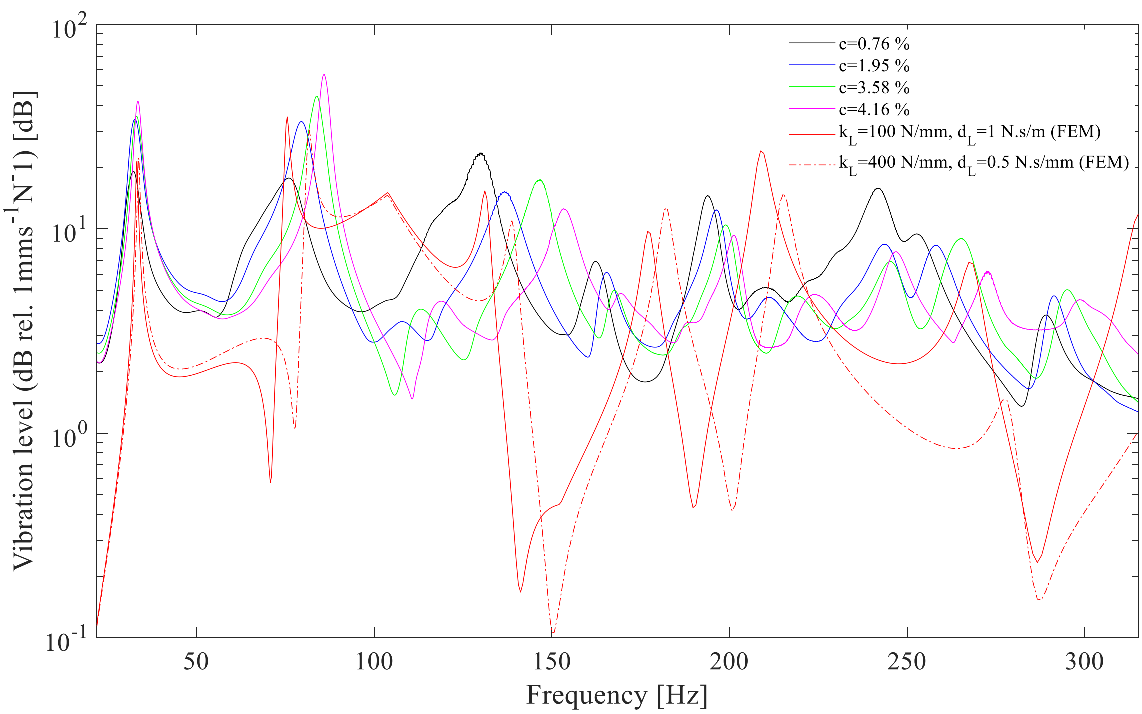

Figure 61. FEM results associated with experimental ones for the with treatment case.

As reported in Table 4, the response curve area (U) can be reduced by increasing the pre-compression rate (C). So that a multimode vibration isolation of almost 44 % is achievable by a pre-compression rate as small as 4 %.

Table 4. The reduction rate achieved per different pre-compression rates.

C (%)	U (Hz.ms^{-2}N^{-1})	Reduction rate (%)
0	3656.3	-
0.76	3009.7	17.68

1.95	2158.1	40.98
3.58	2071.2	43.35
4.16	2034	44.37

The results revealed that higher pre-compression rate offers higher isolation rate over the whole frequency range, although the relationship between the *C* parameter and vibration amplitude is not necessarily linear when it comes to local peaks. So that the isolation rate can be improved if the isolator follows a semi-active scheme optimized in frequency domain. Accordingly, an automatic semi-active vibration control strategy will be proposed in the next section, where wide band vibration cancellation is accomplished through a range-by-range vibration treatment.

4.3 Results of Phase B (Bearing host plate)

The experimental setup entails a bearing host plate that is securely fastened alongside its edges. This plate is subjected to excitation using an electromagnetic shaker, and this excitation occurs within the frequency range of 200 Hz to 1800 Hz, as illustrated in *Figure 62(a)*. As described in Section 2.3.2, the excitation is applied with an angle of 45° to ensure equal loading components are applied. The frequency response derived from experiment is used to extract *natural* frequencies. Moreover, a free vibration analysis is conducted through numerical simulation, employing higher-order shell elements to model the plate's behaviour. Additionally, a point mass element is used to represent the bearing and shaft masses, as demonstrated in *Figure 62(b)*.

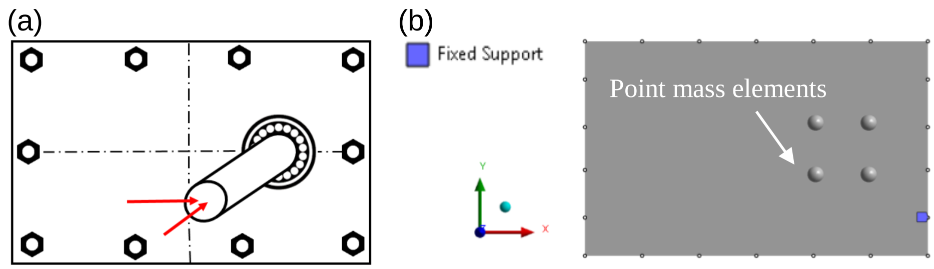

Figure 62. Bearing host plate: (a) schematic model, (b) finite element model.

The experimental results are compared with numerical ones in Table 5 and a relatively close agreement is obtained. The error achieved between two methods is expectable due to the ignorance of the shaft and bearing stiffness in numerical simulation. The effective mass ratio is also reported for each eigenmode, as a result, mode numbers 1, 3, and 8 have the most contribution in system dynamic response.

Table 5. Natural frequencies for the cantilever steel plate (450*300*3 mm3).

Mode no.	M_{eff}/M_t (numerical)	Natural Frequency (Hz)		Error (%)
		Numerical (present)	Experiment (present)	
1	2.12	240.67	246.78	2.54
2	0	360.35	362.1	0.49
3	7.14	388.48	402.96	3.73
4	0	523.57	516.39	1.37
5	0.15	595.64	553.23	7.12
6	0	629.96	646.24	2.58
7	0	843.44	732.8	13.12
8	8.6	937.57	803.23	14.33
9	0	1017.5	1025.54	0.79
10	0.22	1054.3	1122.21	6.44
11	0	1154	1341.39	16.24
12	1.43	1235.2	1468.28	18.87
13	0	1259.6	1512.1	20.05
14	0.49	1435.2	1647.31	14.78
15	0	1504.2	1682.8	11.87
16	0.01	1532.8	1713.36	11.78
17	0	1657.2	1734.68	4.68
18	1.6	1661.2	1753.67	5.57
19	0	1667.2	1769.36	6.13

The deformation contour plots for the eigenmodes with the biggest effective mass ratio are shown in *Figure 63*. It is It can be observed that primarily the eigenmodes are of out-of-plane type in the studied frequency range. Therefore, the vibration isolator is considered to be considered normal to the plate plane to provide the greatest isolation effect. Considering the deformation distribution illustrated by *Figure 63*, the isolator location is denoted by (★) where primarily targets the antinode associated with mode no.8. Additionally, it affects the antinodes corresponding to mode no.1, and to some degree with mode no.3.

Mode no. 1

Mode no. 3

Mode no. 8

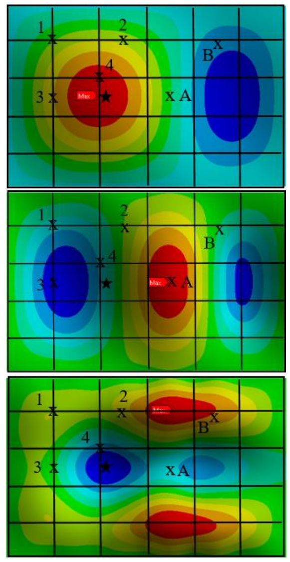

Figure 63. Deformation contour of the bearing host plate for the eigenmodes with largest effective mass ratio.

The isolator is located near an antinode corresponding to the first eigenmode and at a distance equal from the shaft and the plate edge. So that the wave transmission mechanism before and after reaching the isolator can be studied. *Figure 64* shows the physical setup for the bearing host plate forced vibration test. Points A and B which lie on symmetric lines with respect to the bearing position, are selected for optimal tuning of the vibration isolator (see *Figure 64*). The choice of these points is motivated by the aim of minimizing the response at points as close as possible to the excitation source.

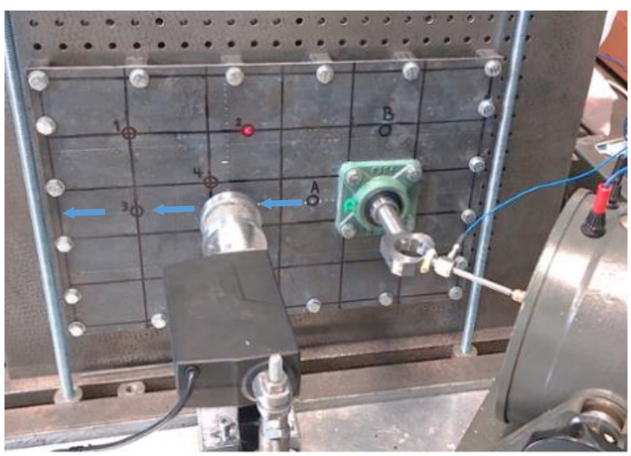

Figure 64. Positioning the isolator on the bearing host plate, and assigning the optimization and measurement points.

As a result of vibration test under semi-active control, the mobility spectra for points A and B considering a possible range of compression rates are presented in *Figure 65* (a) and (b), respectively.

(a) (b)

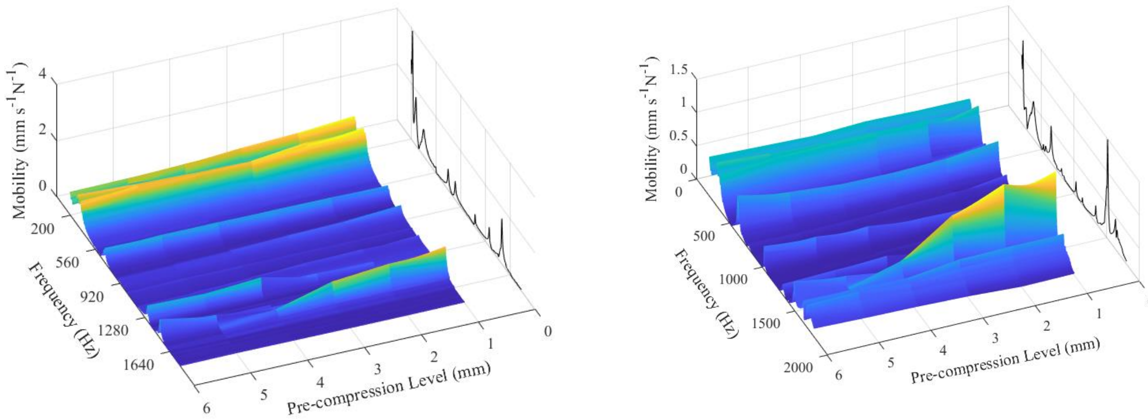

Figure 65. Frequency response surface for different pre-compression levels recorded at points: (a) A, and (b) B.

To perform the cumulative optimization, the frequency range is divided to four equal frequency intervals. Each frequency interval is considered for dual objective optimization of pre-compression rate based on minimization of *U* parameter for points A and B. *Figure 66 (a-d)* illustrate the variation of *U* value at points A and B versus *C* parameter. The cumulative optimization algorithm searches for the minimum value *U* common between points A and B. So that it converges after I, II, III, ... iterations reaching the optimum value of *C* for each frequency interval.

(a)

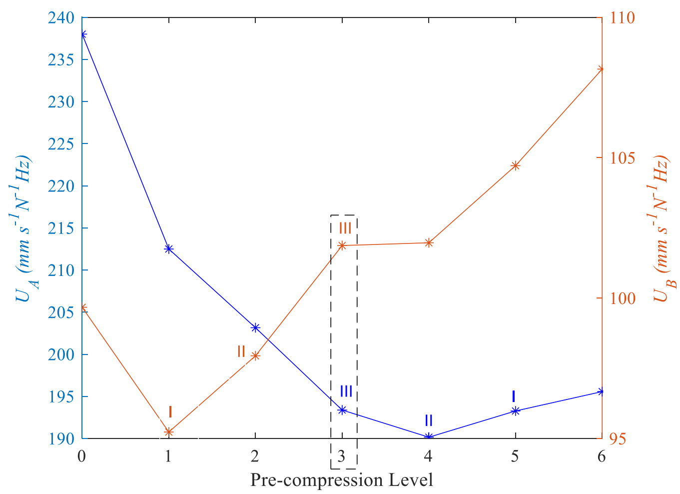

(b)

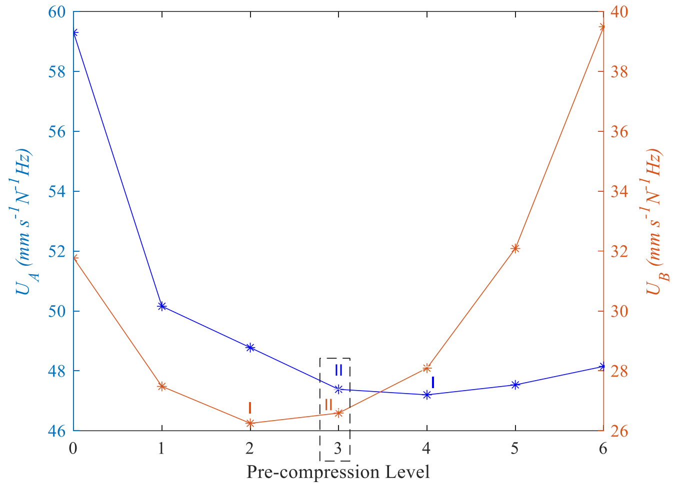

(c)

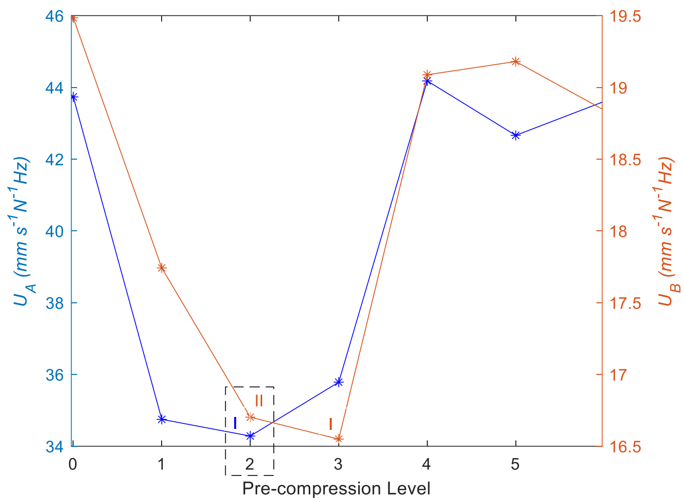

(d)

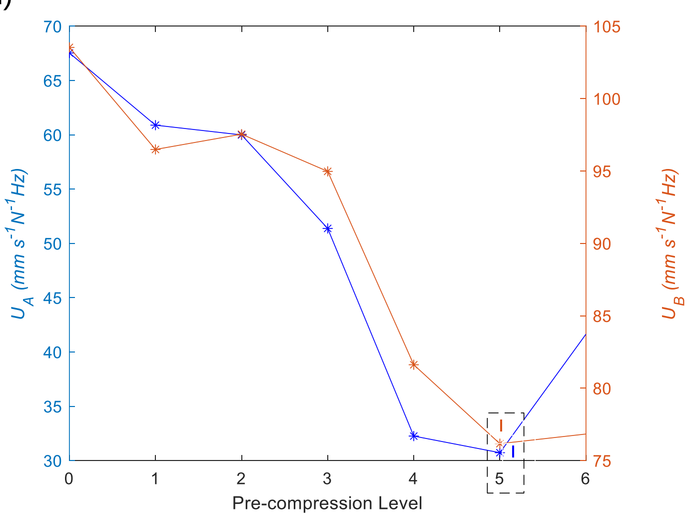

Figure 66. U parameter versus pre-compression level at points A and B, and convergence of optimization algorithm: (a) 200-600 Hz, (b) 600-1000 Hz, (c) 1000-1400 Hz, (d) 1400-1800 Hz.

According to the result of optimization, the optimal values of pre-compression for the four chosen frequency ranges are obtained as C_{opt1}=3 mm, C_{opt2}=3 mm, C_{opt1}=2 mm, and C_{opt1}=5 mm. So that the optimal control function can be written as

$$C_{semi-active} = 3\ heaviside(f - 200) - heaviside(f - 1000) + 3\ heaviside(f - 1400); \quad (26)$$

The results of point by point and cumulative optimizations at points A and B are illustrated in *Figure 67 (a) and (b)*, respectively. It can be determined that when a sine sweep excitation is used, the cumulative optimization is more useful than the frequency based optimization. The reason is that the cumulative optimization provides a limited number of optimal levels that correlate to specific frequency ranges, whereas point-by-point optimization provides an optimal level for each frequency value. As a result, when cumulative optimization is used, fewer actuator movements are needed, and the transient effect caused by actuation motion is reduced.

(a)

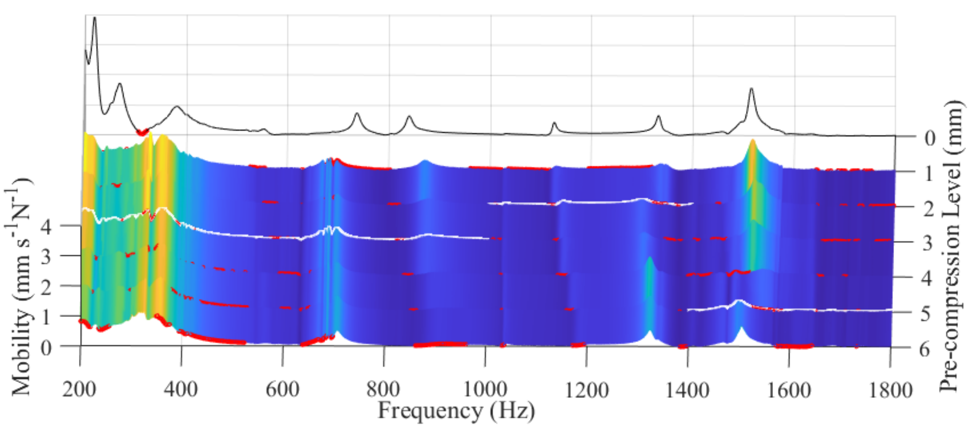

(b)

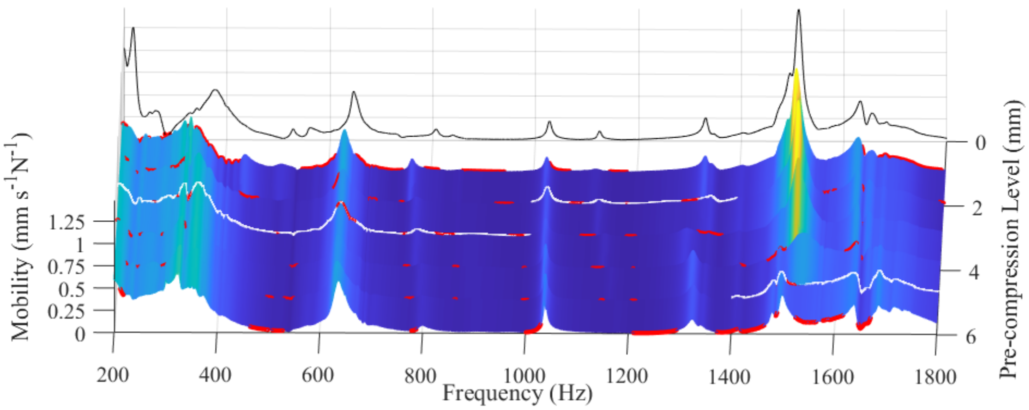

Figure 67. Optimization results based on point by point (—), and band (▭) optimization methods associated with the reference (—) recorded at points: (a) A, and (b) B.

In order to isolate vibrations semi-actively, the control function obtained by band optimization is used to define the optimal control path for a forced vibration test which takes 200 seconds indicated by *Figure 68*.

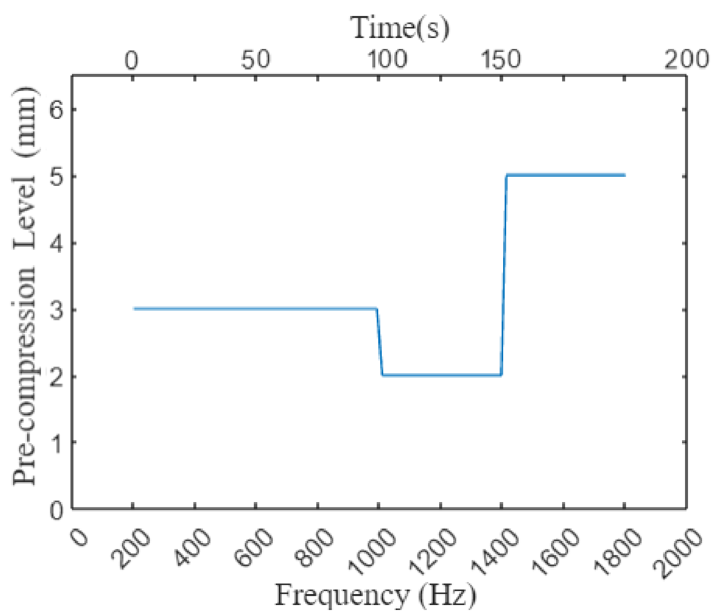

Figure 68. Optimal pre-compression path in frequency and time domain.

The mobility-frequency response at optimization points with and without (w/o) semi-active control is demonstrated by *Figure 69*. Points A and B exhibit isolation rates of 13.63% and 5.95%, respectively. These specific points hold significance in the optimization process, although their vibration reduction rates are relatively minor. The modest impact on vibration levels at points A and B can be attributed to their considerable distance from the isolator attachment point.

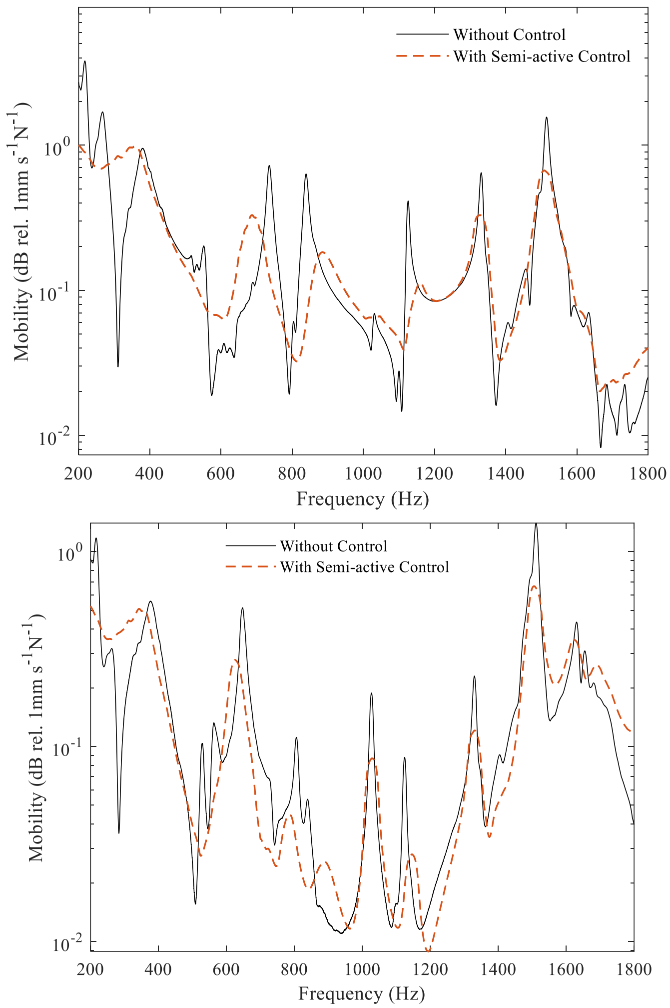

Figure 69. Mobility response w/o control recorded at points: (upper) A, and (lower) B.

To reach a clear understanding of the structure behavior w/o semi-active control, points 1-4 showed in *Figure 70* are considered for measurement. According to *Figure 70* (a-d), the semi-active vibration control led to reduction of vibration by 20.94 %, 23.54 %, 43.76 %, and 55.17 %, respectively for points (1-4). The highest isolation rate occurs at point 4, closest to the isolator attachment position. With respect to the elastic wave propagation indicated by blue arrows in *Figure 64*, points A and 3 are positioned on opposite sides of the isolator, with point A preceding it. The isolation rates for points A and 3 are 13.63% and 43.76%, respectively. This increase in isolation rate occurs as the elastic wave passes the isolator attachment position. Similar reasoning applies to points 1 and 2.

(a)

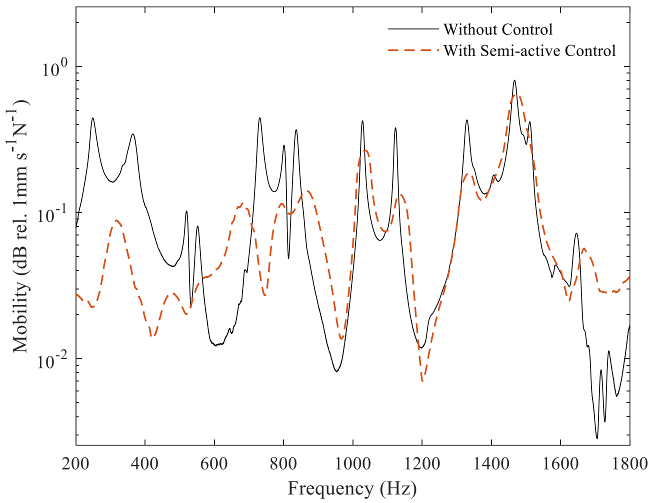
Without Control
With Semi-active Control
Mobility (dB rel. 1mm s-1N-1)
Frequency (Hz)

(b)

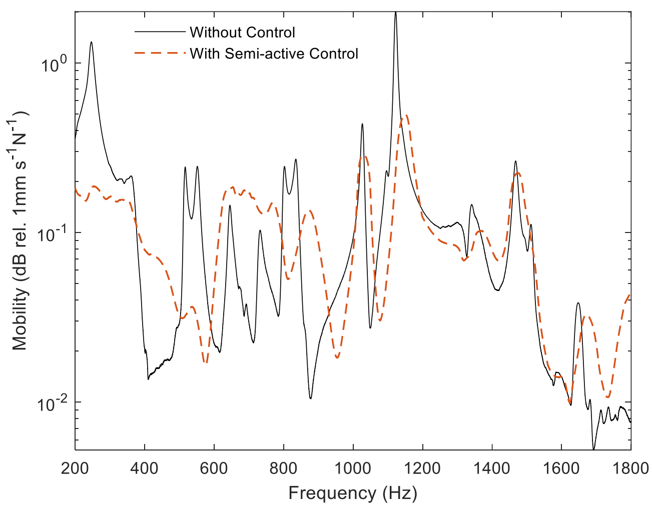
Without Control
With Semi-active Control
Mobility (dB rel. 1mm s-1N-1)
Frequency (Hz)

(c)

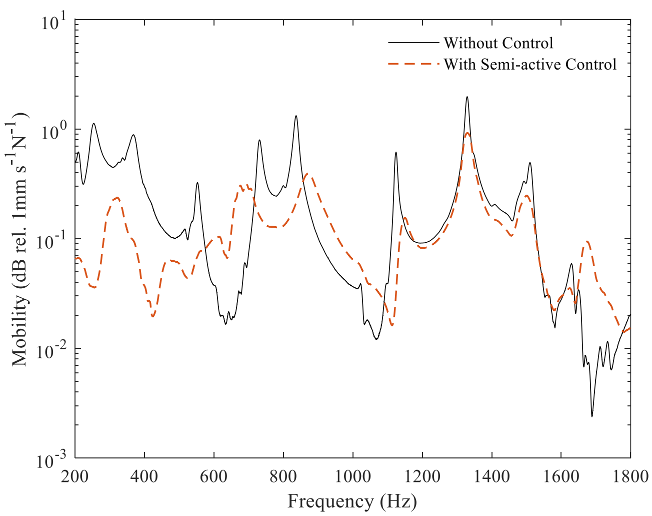
Without Control
With Semi-active Control
Mobility (dB rel. 1mm s-1N-1)
Frequency (Hz)

(d)

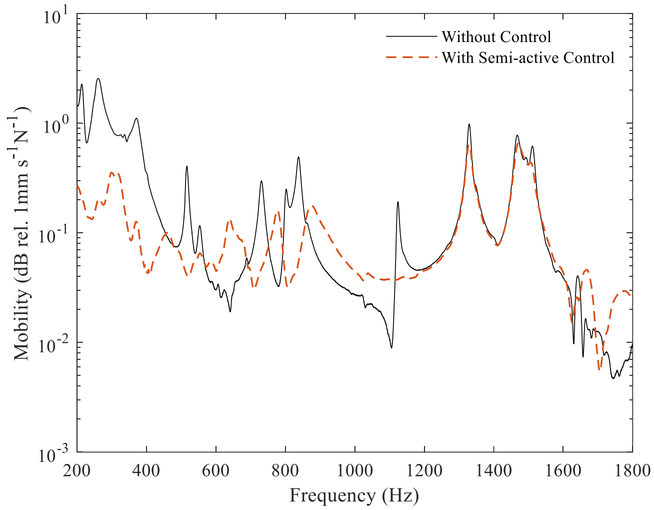

Figure 70. Mobility response w/o control recorded at points: (a) 1, (b) 2, (c) 3, and (d) 4.

The effectiveness of current semi-active approach for different contributions of excitation load is investigated. For this purpose, harmonic tests for several excitation angles are conducted w/o semi-active control. *Figure 71* demonstrates the effect of loading components contribution on the *U* parameter w/o semi-active control over the whole frequency range recorded at point 4. It can be observed that the semi-active control has led to isolation at all angles; however, the isolation rate is minimum at the angle of 0°. The isolation rate obtained for angles 0, 30, 45, 60, and 90 is 26.76 %, 68.86 %, 55.17 %, 51.75 %, 51.63 %, respectively. The isolation rate is minimum for the loading angle of 0 which is expected since the isolator is attached normal to the plate, and loses its efficiency when the normal component of bearing reaction force is much smaller than the in-plane one.

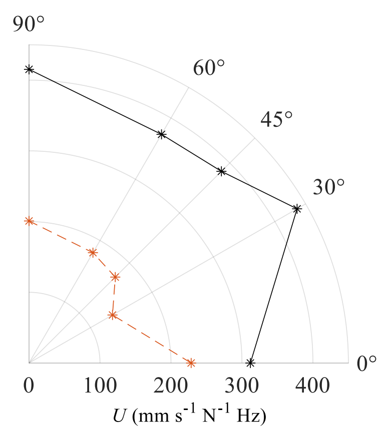

Figure 71. Effect of loading components contribution on U parameter w/o semi-active control over the whole frequency range (200-1800 Hz).

To figure out the influence of loading components contribution on the control approach at resonances, the mobility-frequency response is studied. Although *Figure 71* shows that a successful isolation is feasible according to *U* parameter criteria, the results of mobility amplitude at resonances, reveal favorable and unfavorable effects as reported in *Figure 72*.

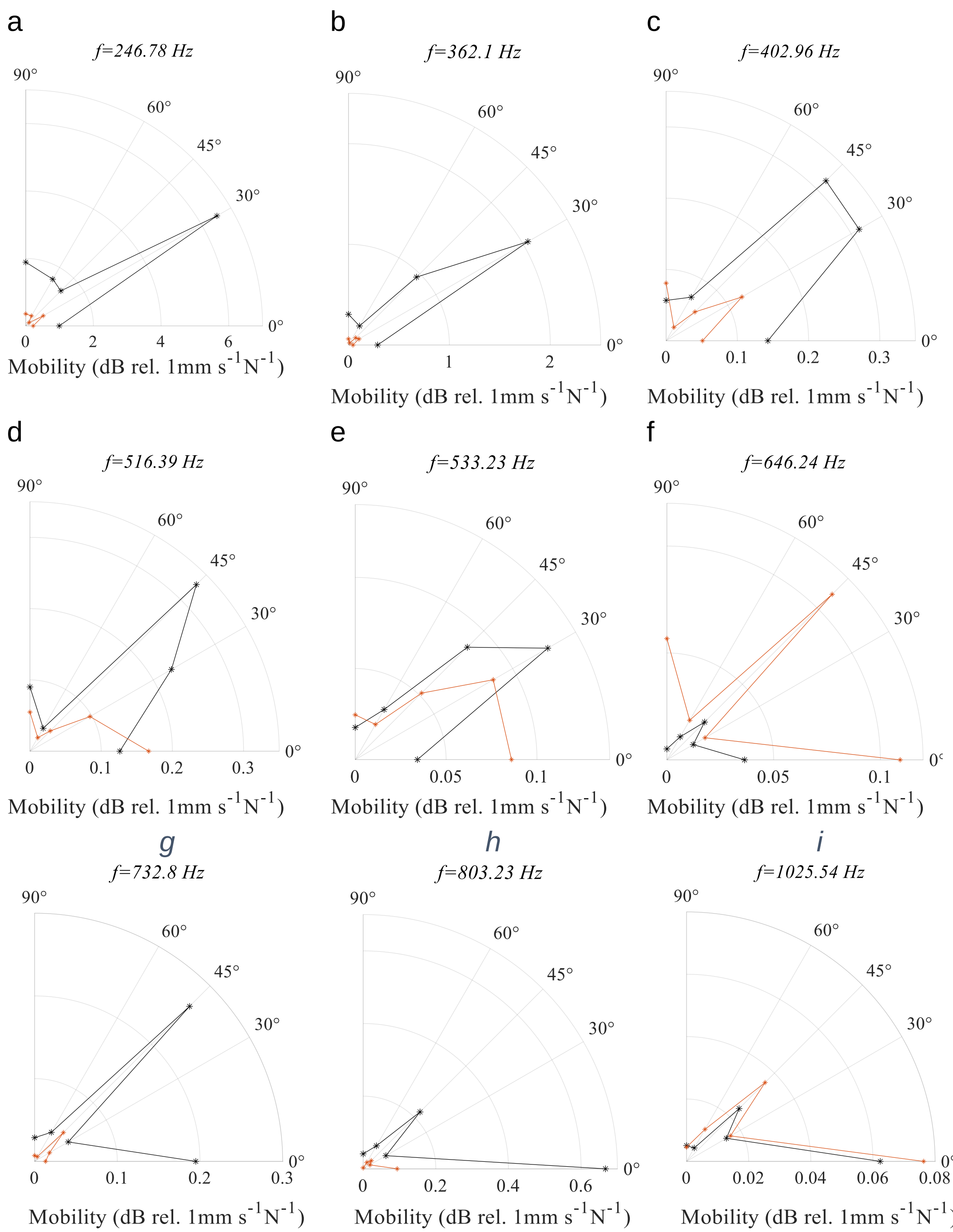

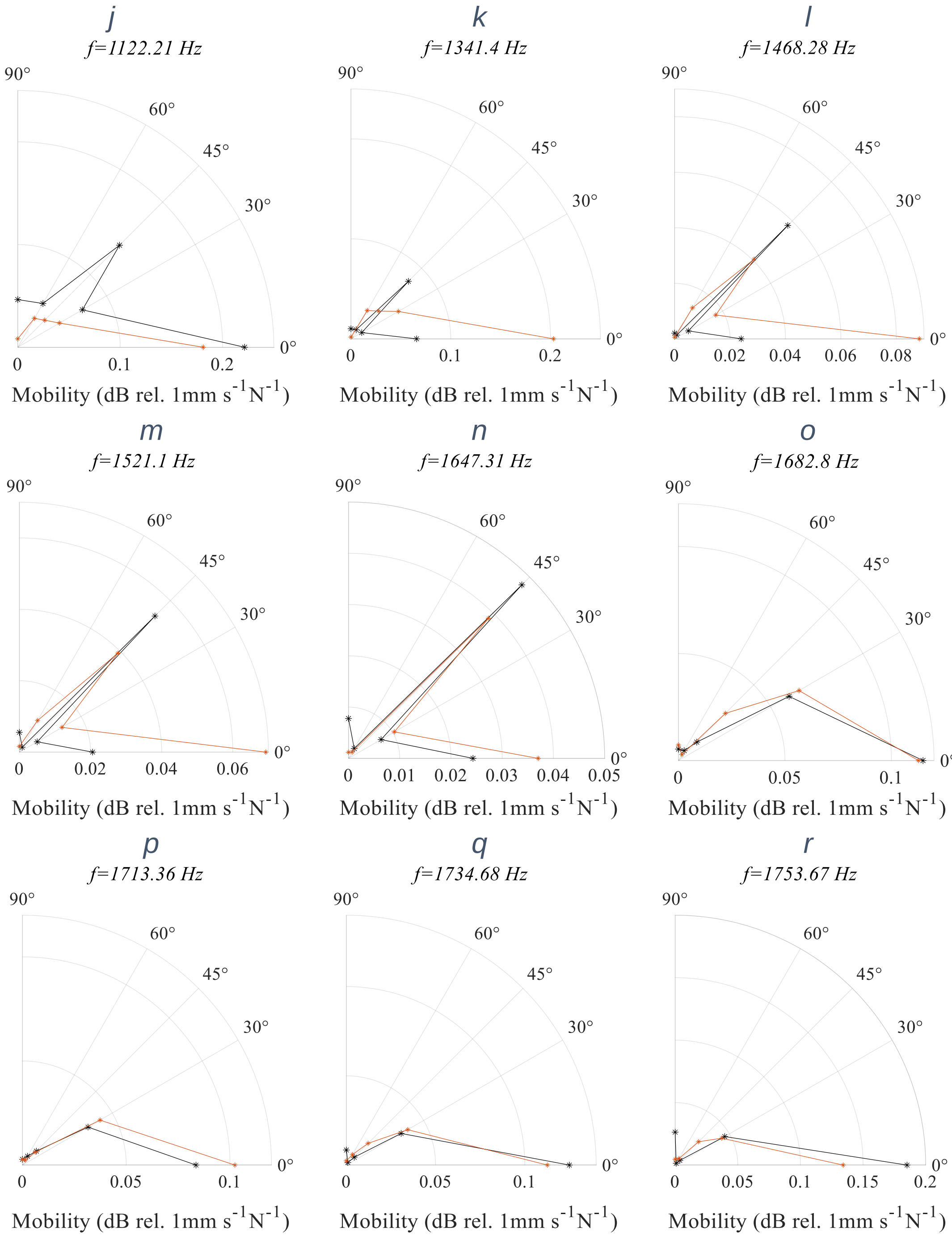
j
f=1122.21 Hz
k
f=1341.4 Hz
l
f=1468.28 Hz
m
f=1521.1 Hz
n
f=1647.31 Hz
o
f=1682.8 Hz
p
f=1713.36 Hz
q
f=1734.68 Hz
r
f=1753.67 Hz
90°
60°
45°
30°
0°
Mobility (dB rel. 1mm s-1N-1)

s

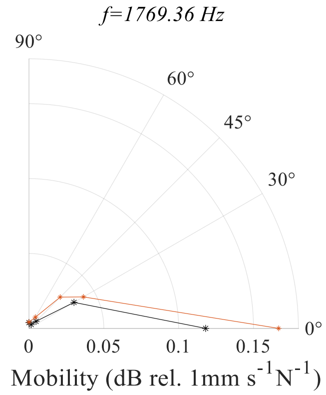

Figure 72. Effect of loading components contribution on mobility (mm.s-1N-1) amplitude with (___) and without (___) semi-active control reported at resonances.

It can be observed that a successful isolation is attained for excitation angles of 30°, 45°, and 60° at resonances 246.78° Hz, 362.1° Hz, 402.96 Hz, 516.39 Hz, 533.23 Hz, 732.8 Hz, 803.23 Hz and 1122.21 Hz, whereas unfavorable effects attribute to the angles of 0°, 90°, or both of them. Ergo, it can be stated that vibrations can be isolated at the vicinity of isolator attachment point in the frequency range of 246.78-1122.21 Hz for 30°, 45° and 60° loading angles which offers a wide range of angles for mechanical transmission systems design. Excitation angle of 0° has produced unfavorable impacts in more than 50% of resonances across the entire frequency range. This indicates that the efficacy of isolation decreases when the in-plane component of loading is significantly greater than the out-of-plane component. Although having unfavorable local effects is inevitable using the semi-active control based on optimal *U* parameter, they can somewhat be eliminated by reducing the size of frequency interval for optimization of *U* parameter. It should be also noted that under operational industrial condition, the favorable effects can be enhanced since the working frequency ranges are determined and limited.

4.4 Results of Phase C (Vehicle Transmission Plate)

4.4.1 Results of Natural Frequency Testing

The plate natural frequencies obtained by modal testing are in accord with those achieved by FEM using ANSYS (version 2022 R2; Ansys Inc.) as reported in Table 1. The natural frequencies are quite far from the metal rubber resonance, which, as reported by Silentflex Company, falls between 14 and 18 Hz (Silentflex, 2023). Since the first natural mode has the highest contribution in the structure harmonic response, the isolator is attached to the hole noted by star symbol on the FEM model in *Table 6* to affect the first natural frequency antinode. In addition, having enough room for the shaker required for the upcoming harmonic tests slightly limits the freedom to position the isolator. The natural mode shapes also help choose proper points for optimization. In this regard, points A and B are selected for double-objective optimization since they are more or less close to mode shapes antinodes.

Table 6. Natural frequency and mode shapes obtained by experiment and FEM.

Experiment		FEM	
Natural Frequency (Hz)	Natural Mode	Natural Frequency (Hz)	Natural Mode
2345. 74	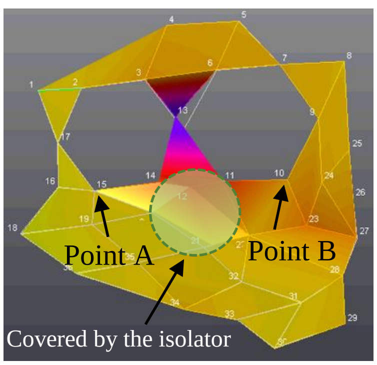	2151.3	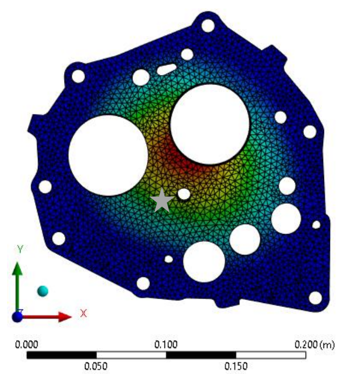
3454.66	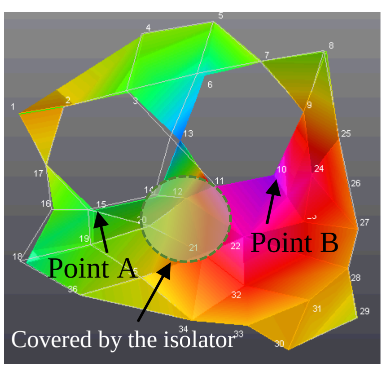	3595.5	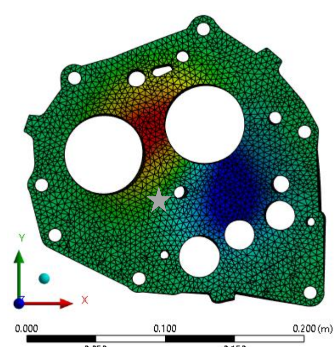

4802.69	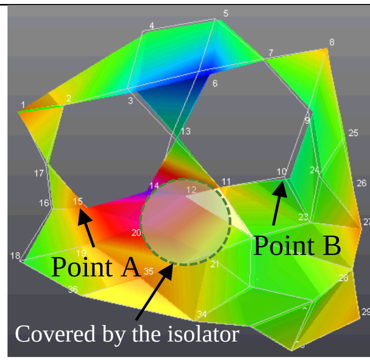	4910.8	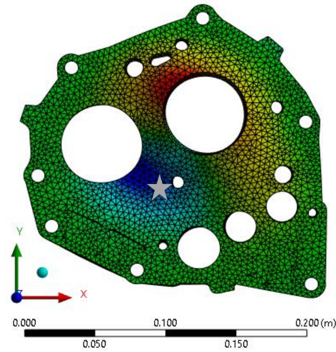

4.4.2 Results of Tuning

To tune the vibration isolator, a parametric study on the effect of six control levels which correspond to 2%, 3%, 4%, 5%, 6%, and 7% pre-compression rates is carried out. The result of impact hammer testing indicated by *Figure 73(upper) and (lower)* represents the effect of control level on the response at points A and B, respectively. These findings highlight the potential to fine-tune the isolator and reduce vibrations by adjusting the control level. The outcome of optimizing the parametric studies is visually manifested through the utilization of color-coded lines. In this context, the red and green lines are expected to be the optimal responses associated with the open-loop and closed-loop strategies, respectively. It is worth noting that the multitude of resonances surpassing those listed in *Table 6,* is attributed to the supporting structure's contribution to the response recorded which is even unavoidable in operative conditions. Thus, in this study the effect of vibration control will be assessed in the whole frequency domain continuously including all resonances.

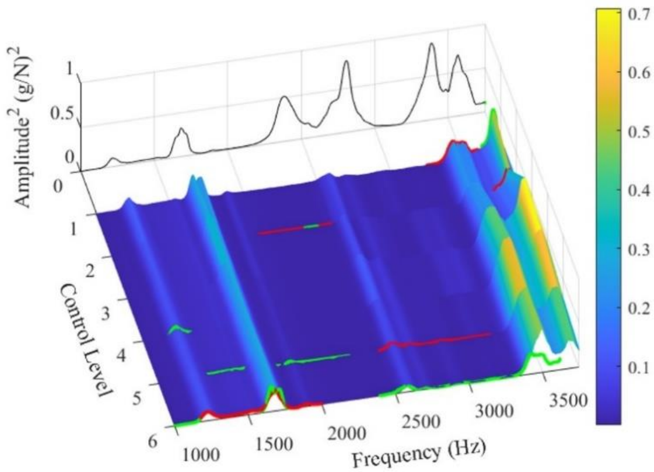

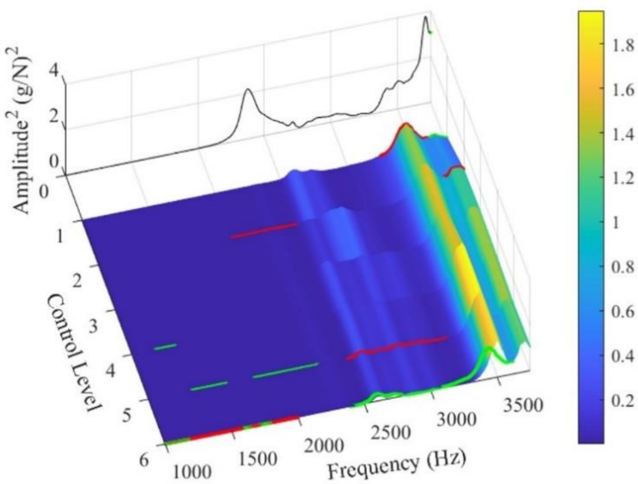

Figure 73. Response recorded at optimization points associated with reference response (black line), open-loop optimal. response (red line), and closed-loop optimal response (green line): (upper) point A, (lower) point B.

Finally, the optimal semi-active functions for open-loop and closed-loop controls are driven by Eqs. (13) and (14), respectively. In addition, *Figure 74* shows the optimal control paths for open-loop and closed-loop strategies. The two paths are different because the harmonic modes determine the optimization frequency intervals for the closed-loop strategy, while the open-loop strategy is developed based on observation of response peaks.

$$C_{sao} = 6H^*(f-1000) - 4H^*(f-2000) + 3H^*(f-2500) - 4H^*(f-3250) + H^*(f-3600) \tag{13}$$

$$C_{sac} = 6H^*(f-1000) - 2H^*(f-1177.7) + H^*(f-1326.1) + H^*(f-1587.2) - H^*(f-1793.2) - 3H^*(f-2293.6) + 4H^*(f-2396.8) + 5H^*(f-3620.9) \quad (14)$$

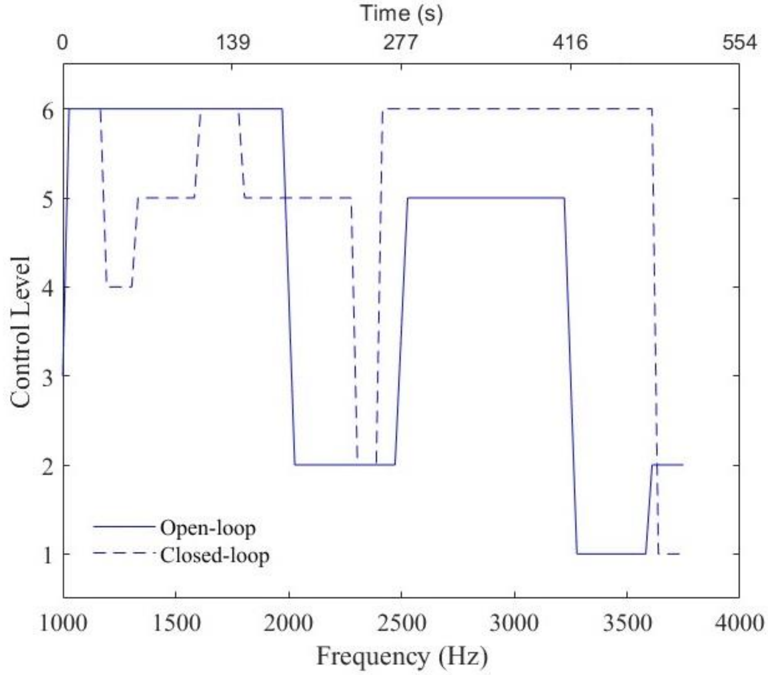

Figure 74. Open-loop and closed-loop optimal control paths.

4.4.3 Results of Noise and Vibration Control

According to *Figure 75* (upper), the vibration response is measured by PCB accelerometers at points 1, 4, 6, 8, 10, 15, 18, 28, 30, 34, and 35, while points 10, and 15 are the only points for the optimization. The points in green circles are unmeasurable because of interference with the isolator. The dashed red circle is the shaker stinger attachment point. Therefore, the study analyzed vibrations at 11 selective points (see *Figure 75* (upper)) and found that open-loop and closed-loop strategies can reduce vibrations by 28.71% and 23.57%, respectively (*Figure 75 (lower)*). One more finding is that the closed-loop curve behaves like an off-set of the open-loop curve; however, their amplitude compared to each other is variable over the frequency range.

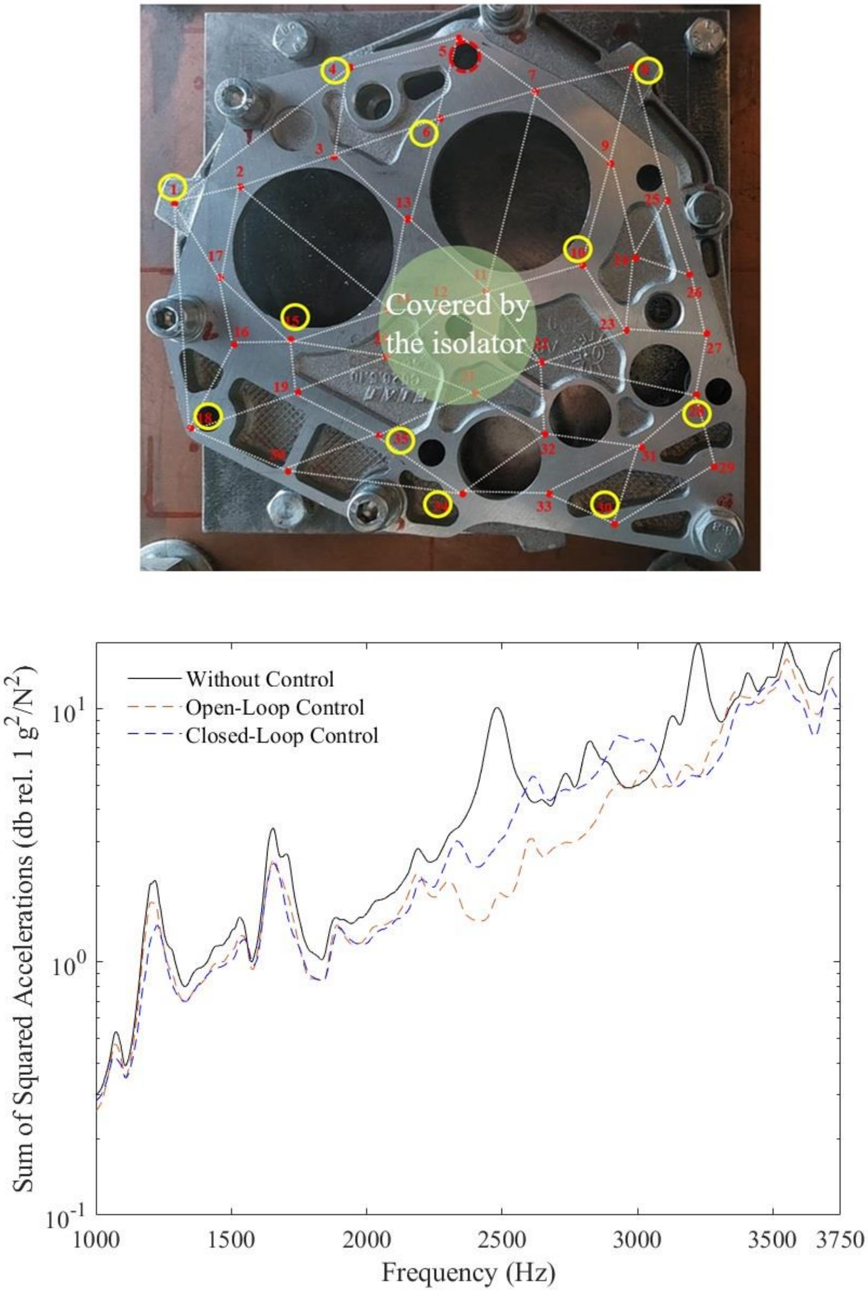

Figure 75. Vibration control testing: (upper) measurement points marked by yellow circles, (lower) structural response w/o control.

The Radiated power measured by SIP is illustrated by *Figure 76* indicating the effect of control strategies with the reference case where no control is applied. The open-loop and closed-loop strategies adopted for noise control resulted an overall isolation of 25.03% and 19.97%, respectively, indicating proper attenuation of structure-borne noise. A largely favorable influence on the radiated noise level is found across the studied frequency range using the closed-loop control strategy.

However, there is a unique lower frequency band below 1375 Hz where two distinct peaks clearly exceed the reference noise level. The extent of this adverse effect is substantial, resulting in a reduction of the overall closed-loop impact to a level lower than the overall open-loop impact. Shifted slightly to the right along the frequency axis, the aforementioned adverse effect is also evident in the open-loop response, albeit with reduced intensity.

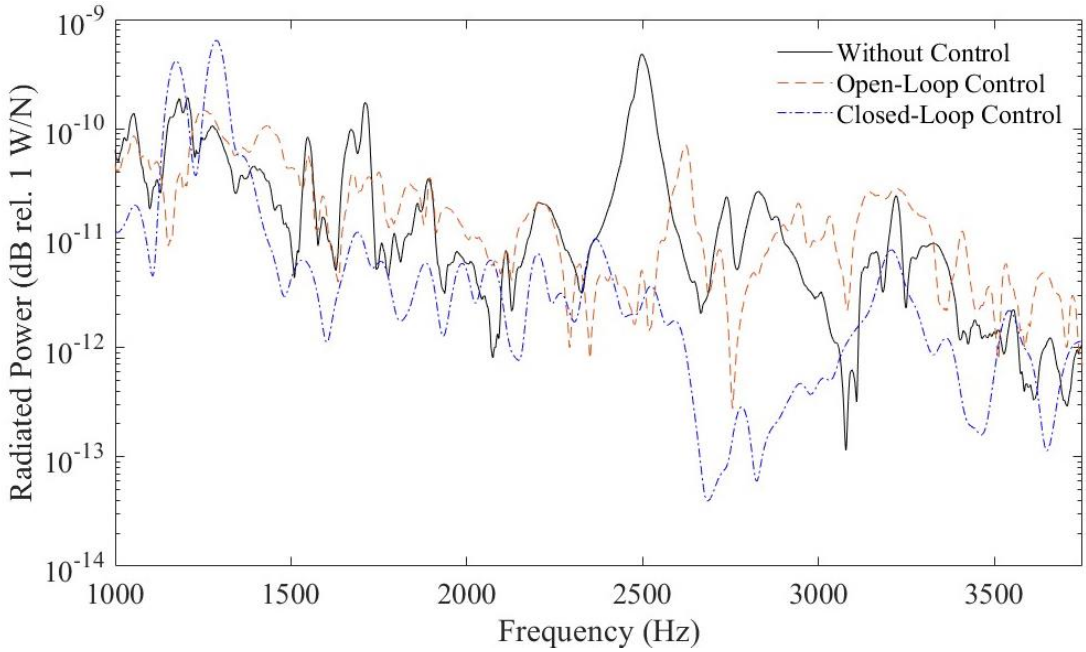

Figure 76. Radiated power measured by sound intensity probe.

The representation of radiated power in standard one-third octave frequency bands is provided by *Figure 77*. Despite the overall noise reduction discussed previously, it is essential to address the adverse effects observed within certain frequency bands. Notably, the open-loop technique demonstrates effectiveness in the first and third octave bands, whereas the closed-loop strategy proves advantageous across all octave bands except for the first one. To scrutinize the underlying cause for the adverse effect observed in the first octave, the frequency response for both vibrations and acoustics should be investigated. The vibration frequency response given by *Figure 75* shows no indication of shortcomings at low frequencies for the closed-loop control scheme. However, in *Figure 76*, illustrating the radiated power in the frequency domain, "Closed-loop Control" curve have two peaks at 1483.41 Hz and 1505.27 Hz, surpassing the "Without Control" curve values. It is noteworthy that, given a sine-swept excitation rate of 5 Hz/s, the transition from the first peak to the second one occurs over a duration of 4.4 seconds. The brief transition time is susceptible to time mismatches from a possible imperfect triggering of the three hardware components (two measurement units and one control unit described in section 3.7.2). A solution to this challenge is to conduct all measurement and control tasks using a unique processor, and program the processor to trigger all tasks simultaneously. For instance, the execution of the aforementioned tasks can be all delegated to a single microcomputer; nonetheless, it necessitates hardware development, such as the incorporation of signal conditioning circuits, and software development.

An alternative factor resulting the observed adverse effect of control at low frequencies could be the material elastic instability after cycles of loading and unloading. As outlined in section 4.4.2, with six control levels (2-6% pre-compression rates) applied to the 25 mm MR sample, the MR sample static displacement domain spans from 0.5-1.5 mm, with notably small increments. The reason behind this control domain definition is to prevent excessive elastic deformation to the host structure shell which is not recommended for long term operation. Consequently, such these small control levels may be applied inaccurately if the elastic instability order exceeds the displacement steps. Thus, studying the elastic instability of MR material under different levels of porosity is a topic of paramount importance to be carried out in future studies.

The radiated power contour plots corresponding to these octave bands are represented by Appendix 2. The radiated power maps offer a continuous variation of power over the surface which verifies the continuity of energy, indicating that the measurement grid size adopted is sufficient. In addition, making a comparison between plots with and without control notifies that the control does not much improve the area around the stinger attachment point. The last point is that comparing plots with and without control reveals fewer distinct zones in the controlled map. This suggests the suppression of some vibration modes of higher order.

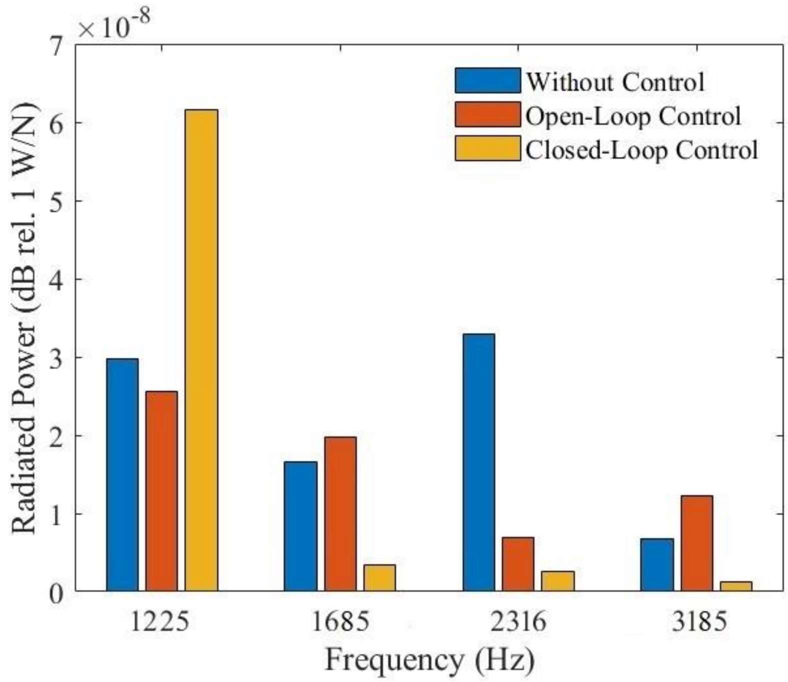

Figure 77. The radiated power in 1/3 Octave band.

Chapter 5: Summary, Conclusion and Future Work

5.1 A glance to research motivation

The impact of means of transportation on the overall comfort and life quality of passengers in urban areas is multidimensional, including vibration, noise and other responsible effects. In recent years, the effects of excessive noise pollution on urban dwellers are becoming more dominant. To address this issue, the United Nations Economic Council for Europe (UN/ECE) has introduced stringent regulations on the permissible levels of noise emitted by vehicles. These regulations emphasize the necessity to improve the vehicle noise and vibration performance.

One of the most important contributors to vehicle overall acoustics is powertrain noise. In the era of automotive electrification, where electric motors replace the traditional internal combustion engine, engine noise is vanished but this transition has overshadowed the prominence of powertrain noise. EVs and hybrids in particular are known for relatively loud powertrain noise. Addressing powertrain noise is therefore of the utmost importance as it can significantly affect passenger comfort and the overall occupant experience. Furthermore, in an urban environment where traffic congestion is prevalent, the noise generated by heavy traffic can greatly affect the quality of life for urban residents so it is important to find innovative solutions to reduce electrical noise and enhance acoustic comfort for commuters and city dwellers.

There are two main methods of effectively reducing power supply noise that can be used alone or in combination. The first involves redesigning the powertrain design itself, focusing on optimizing components and reducing noise-generating processes. The second approach involves innovative vibro-acoustic solutions that can accommodate, to smooth, or reduce the vibration and noise generated by the powertrain. The solution can be integrated into the structure of the vehicle to reduce noise to the passenger compartment and surrounding environment

Several innovative solutions have emerged to address noise and vibration challenges in vibration and sound control, especially in automotive-like applications where lightweight systems, fuel efficiency and wideband efficiency are essential conditions to be met. These solutions encompass passive, active, and semi-active systems. Passive solutions involve the use of materials and structures designed to absorb or dampen vibrations and noise passively, enhancing comfort without the need for active intervention. Active solutions, on the other hand, employ sensors and actuators to actively counteract incoming vibrations and noise, offering real-time noise cancellation. Semi-active systems strike a balance between the two, providing dynamic control of vibrations and noise while optimizing energy efficiency. In the automotive sector, where reducing vehicle weight and fuel consumption are critical, semi-active vibroacoustic control solutions play a pivotal role in creating quieter, more efficient, and more comfortable vehicles for consumers.

5.2 Summary of key findings and contributions

This is the first thesis to present a semi-active vibration control based on MR material, the frequency adaptability of which was previously demonstrated by Rieß and Kaal (Rieß and Kaal, 2021). The current research design includes the MR sample selection, assembly of the electromechanical devices, and programming the control. The assessment of noise and vibration reduction is carried out in three phases using different structures including a cantilevered plate, a bearing host plate, and a vehicle transmission system plate.

In the first phase, the cantilevered plate which free vibration behavior has been validated by numerical simulation and literature is tested under different pre-compression levels of the MR material. The results revealed 44 % reduction of plate free edge mobility amplitude when the MR is compressed only 4 %.

The result obtained for vibration isolation of the cantilevered plate provided the confidence to employ the MR-based isolator for a bearing host plate, as a practical example. In this regard, the isolator has been positioned according to the analysis of eigen mode shapes obtained by numerical simulation. The excitation has been applied with an angle of 45° to impose comprehensive reaction forces. A point-by-point numerical optimization led to a heavily variable control path which implementation is not feasible for a sine sweep excitation since the control state should be changed repeatedly, inducing many transient effects. For this reason, the results have been optimized through a cumulative method which minimizes the *U* parameter in frequency ranges, and proposes a control function based on Heaviside functions. With the help of Heaviside functions, optimal values of control variable, *C,* have been introduced not for each frequency value but for four frequency ranges of the same size. Hence, the actuator required to move for fewer times. So that an open-loop semi-active control strategy has been developed for a given frequency range based on the cumulative optimization results to isolate the vibrations.

Studying *U* parameter values at a point near the actuator attachment point, isolation rates of 26.76 %, 68.86 %, 55.17 %, 51.75 % and 51.63 % have been recorded for the excitation angles of 0°, 30°, 45°, 60°, and 90°, respectively, using the current semi-active control. The parametric study on the angle of excitation revealed that the semi-active control efficiency reduces when the in-plane component of bearing reaction force is much bigger than the normal one.

The second phase of study is dedicated to investigate noise and vibration mitigation efficiency for a plate hosting main transmission bearings in a passenger car. So that by isolating noise and vibrations at the plate level, its transmission to the rest of components can be prevented. To the best of our knowledge this is the first study to assess the effect of a semi-active MR-based isolator in a real-world application. The isolator is tuned to minimize the response at two key points through optimizing the response of a hammer impact test. The result of optimization is used to build the control functions for open-loop and closed-loop strategies using Heaviside functions. It is noteworthy to mention that a novel feed-back control is introduced in this research based on harmonic mode shifting which benefits the development of assessment testing in real-time vehicles. In sum, the semi-active control attenuated vibration level by 28.71% and 23.57% using open-loop and closed-loop strategies, respectively.

In terms of noise control, the implementation of open and closed strategies revealed noticeable results, as shown 25.03% and 19.97% respectively. This means an effective reduction of structure-borne noise is made possible. In particular, the use of a closed-loop control strategy has shown a favorable impact on the reduction of radiated noise levels across the entire range analyzed. However, a distinct observation appears within a certain low frequency range, namely below 1375 Hz, where two noticeable peaks exceed the reference noise. This negative effect is particularly visible and results in a significant effect in the overall isolation rate. Shifted slightly to the right along the frequency axis, the aforementioned adverse effect is also evident in the open-loop response, albeit with reduced intensity.

The functionality of the current approach is deemed acceptable for NVH (Noise, Vibration, and Harshness) improvement. However, it is observed that the closed-loop control exhibits slightly lower efficiency compared to the open-loop control, attributed to the differences in the optimization procedures employed.

5.3 Recommendations for further studies and improvements

Several research and development avenues are open to enhance the functionality and application potential of current research semi-active solution. First, extending the number of MMAs in the system can significantly increase the closed-loop controllability to identify the mode shape perfectly rather than just identifying its change.

Another viable solution is to centralize measurement and control tasks on a single processor, programming it to trigger all tasks simultaneously. However, this approach requires hardware development, including signal conditioning circuits, and software development.

Enhancing the current semi-active controller involves exploring self-powered methods, utilizing pre-compression force to pressure a piezoelectric transducer for potential actuator power. The promising concept, however, poses complexities like designing charging circuits and precise voltage control, necessitating further research and development.

Annex 1

In addition to its current focus, this Ph.D. program also explores another research direction using piezoelectric shunt circuits to control noise semi-actively. Within this context, a numerical model is developed to realize the ABH effect virtually with help of capacitive shunt circuits. The main objective is to attenuate structure-born noise for several resonance modes. Theoretically, virtually imposing the ABH effect is feasible through the electrical analogy which equalizes stiffness with capacitance. The ABH effect is virtually defined by considering *i* number of piezoelectric elements with equal distances attached on a beam surface (see *Annex 1 Figure 1*). Each piezoelectric element is shunted independently by a capacitor.

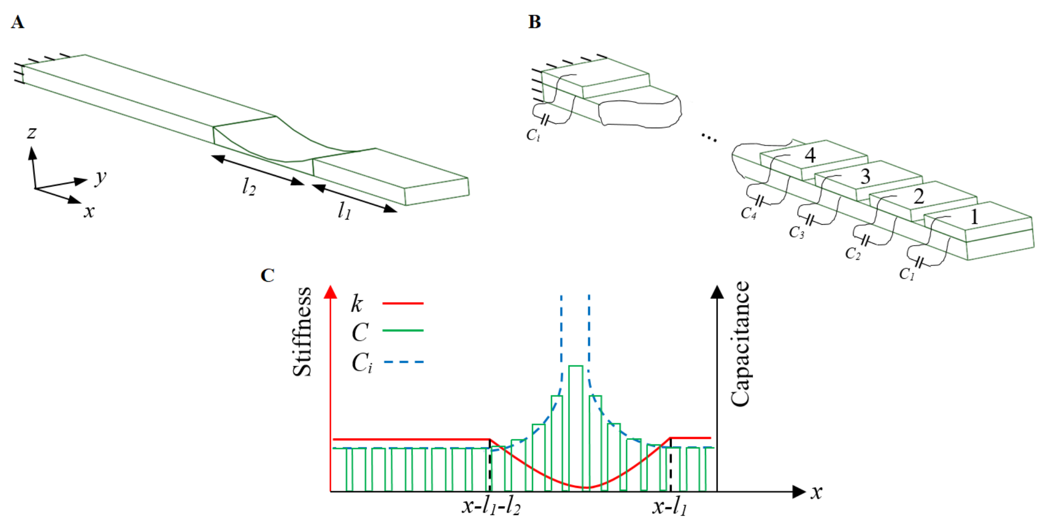

Annex 1 Fig. 1. (A) physical ABH, (B) virtual ABH, (C) stiffness and capacitance variations.

A noteworthy advantage of virtual ABH is the potential for semi-active use which is obviously impossible with the ABH effect imposed by geometry. In addition, the geometrical restrictions related to the physical manifestation of the ABH effect (such as having enough initial thickness and material) do not apply to the virtual method.

For two main reasons the virtual ABH effect deviates from the ideal ABH: 1. Since the energy conversion rate in piezoelectric material is not 100%, the ABH effect can never be idealized. 2. The capacitance profile is discrete along the beam due to the distance between piezoelectric elements which is unavoidable.

The results of present numerical modeling revealed at least 6.37 % improvement for noise radiation. The attenuation is well achieved by breaking down each peak to many more peaks which results an effective absorption effect.

Finally, the virtual ABH effect realized numerically in the present research can be used for isolating structural noise in industrial bodies where there is enough surface for attachment of piezoelectric elements.

Annex 2

The electromechanical control circuit, along with the necessary wirings is illustrated by *Annex 2 Fig. 2*.

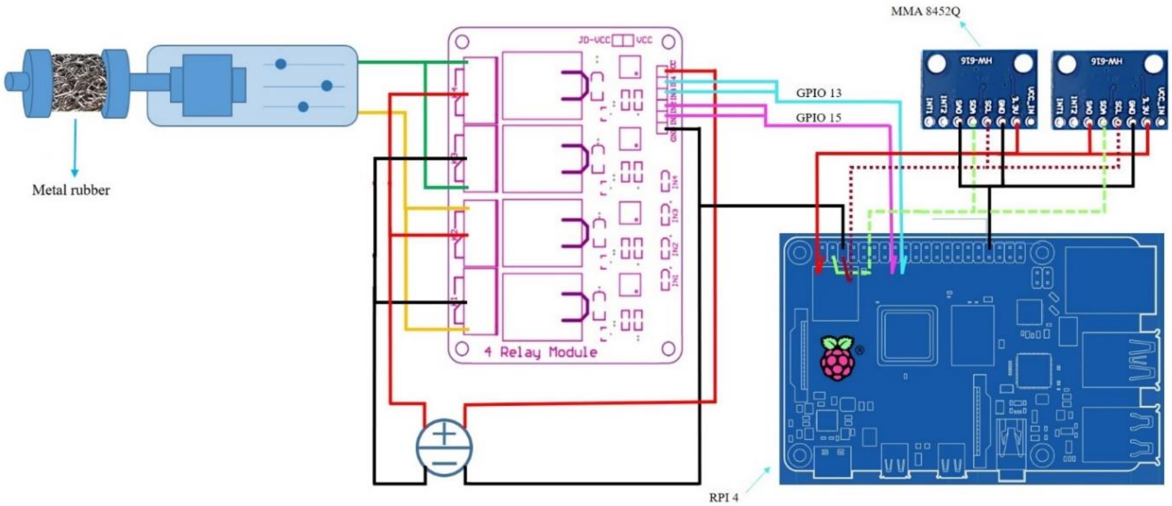

Annex 2 Fig. 1. The control circuit including all electromechanical components.

Annex 3

The *Annex 3 Table 1* offers contour plots illustrating non-dimensionalized radiated power, achieved by dividing the radiated power by the maximum value of power (W_{max}) of the same contour plot.

Annex 3 Table 1. The radiated power maps in one-third octave band centre frequencies (--- represents the stinger attachment point).

Center Frequencies (Hz)	Without Control	With Control
1225	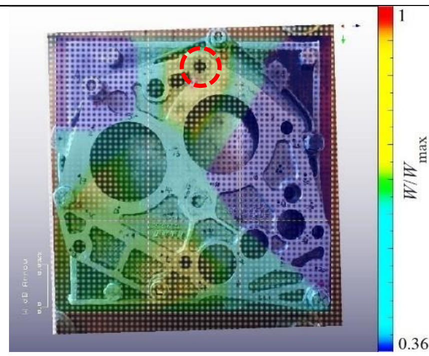	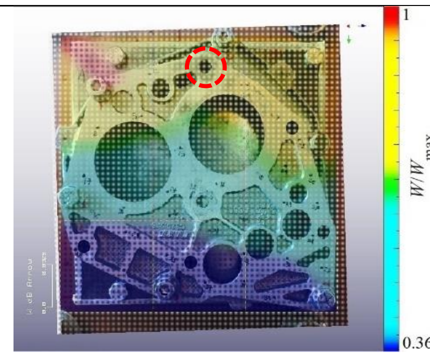
1685	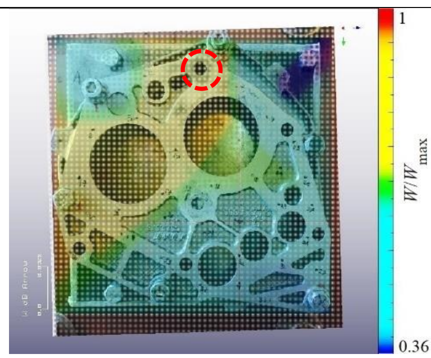	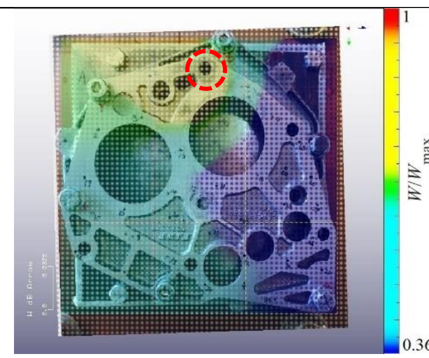
2316	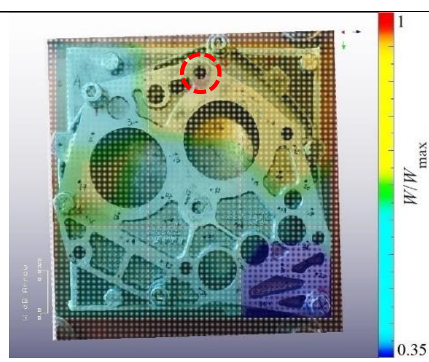	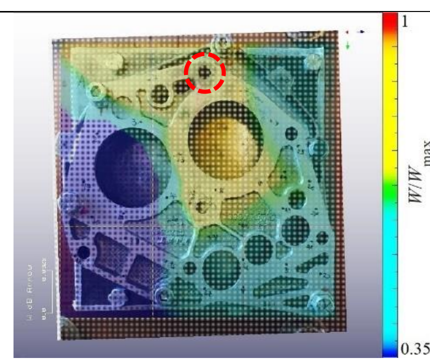

3185	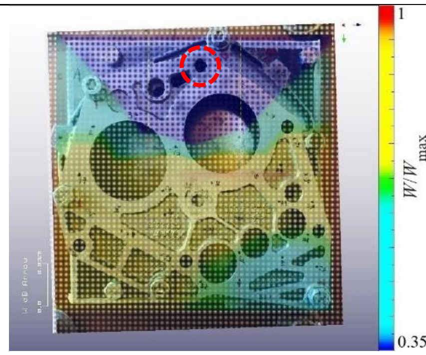	

References

Abu Seer T, Vahdati N and Shiryayev O (2019) Adaptive Torsional Tuned Vibration Absorber for Rotary Equipment. *Vibration* 2(1): 116–134. DOI: 10.3390/vibration2010008.

Ahmed SR (1995) A survey of automobile aeroacoustic activities in germany. *SAE Technical Papers* 104(1995): 1100–1118. DOI: 10.4271/950623.

Amabili M and Rivola A (1997) Dynamic analysis of spur gear pairs: Steady-state response and stability of the SDOF model with time-varying meshing damping. *Mechanical Systems and Signal Processing* 11(3): 375–390. DOI: 10.1006/mssp.1996.0072.

Ansys® Academic Research Mechanical, Release 18.1, Help System, Modal Analysis Guide, ANSYS, Inc. (n.d.).

Auto-Car (2023). Available at: https://autocarsavona.it/.

Bai XX, Wereley NM and Hu W (2015) Maximizing semi-active vibration isolation utilizing a magnetorheological damper with an inner bypass configuration. *Journal of Applied Physics* 117(17): 1–5. DOI: 10.1063/1.4908302.

Batel M, Marroquin M, Hald J, et al. (2003) Noise source location techniques - Simple to advanced applications. *Sound and Vibration* 37(3): 24–38.

Boer LC (Eelco) den and Schroten A (Arno) (2007) *Traffic Noise Reduction in Europe Health Effects , Social Costs And*. Delft.

Braun ME, Walsh SJ, Horner JL, et al. (2013) Noise source characteristics in the ISO 362 vehicle pass-by noise test: Literature review. *Applied Acoustics* 74(11). Elsevier Ltd: 1241–1265. DOI: 10.1016/j.apacoust.2013.04.005.

Cao Y, Hao H, Wang J, et al. (2023) Constitutive relation expansion of large load metal rubber engine mount stress bivariate function relationship using the strain and strain rate. *International Journal of Non-Linear Mechanics* 152(November 2022). Elsevier Ltd: 104385. DOI: 10.1016/j.ijnonlinmec.2023.104385.

Casadei F, Ruzzene M, Dozio L, et al. (2010) Broadband vibration control through periodic arrays of resonant shunts: experimental investigation on plates. *Smart Materials and Structures* 015002. DOI: 10.1088/0964-1726/19/1/015002.

Casciati F, Rodellar J and Yildirim U (2012) Active and semi-active control of structures − theory and applications: A review of recent advances. *Journal of Intelligent Material Systems and Structures* 23(11): 1181–1195. DOI: 10.1177/1045389X12445029.

Chatziathanasiou GM, Chrysochoidis NA and Saravanos DA (2021) A semi-active shunted piezoelectric tuned mass damper for robust vibration control. *JVC/Journal of Vibration and Control* (May). DOI: 10.1177/10775463211026487.

Chen J, Yin Z, Yuan X, et al. (2021) A refined stiffness model of rolling lobe air spring with structural parameters and the stiffness characteristics of rubber bellows. *Measurement* 169(May 2020). Elsevier Ltd: 108355. DOI: 10.1016/j.measurement.2020.108355.

Cho S, Kim H, Kim D, et al. (2020) Optimization and Analysis of Output Pinion Design for Worm Gear Reducer. *The Korean Society of Manufacturing Process Engineers* 19(1): 108–113. DOI: 10.14775/ksmpe.2020.19.01.108.

Choi KM, Cho SW, Jung HJ, et al. (2004) Semi-active fuzzy control for seismic response reduction using magnetorheological dampers. *Earthquake Engineering and Structural Dynamics* 33(6): 723–736. DOI: 10.1002/eqe.372.

Covaciu D, Florea D and Timar J (2015) Estimation of the noise level produced by road traffic in roundabouts. *Applied Acoustics* 98. Elsevier Ltd: 43–51. DOI: 10.1016/j.apacoust.2015.04.017.

D'Alessandro V, Petrone G, Franco F, et al. (2013) A review of the vibroacoustics of sandwich panels: Models and experiments. *Journal of Sandwich Structures and Materials* 15(5): 541–582. DOI: 10.1177/1099636213490588.

Daniel Christie M, Sun S and Li W (2021) Building Vibration Suppression Through a Magnetorheological Variable Resonance Pendulum Tuned Mass Damper. In: *Building Vibration Suppression Through a Magnetorheological Variable Resonance Pendulum Tuned Mass Damper*. Cham, pp. 281–287. DOI: 10.1007/978-3-030-47618-2.

De Roo F (2013) New EU and UN/ECE vehicle noise emission limits and associated measurement methods. In: *Noise Control for Quality of Life*, Innsbruck, 2013, pp. 1–16. 42nd International Congress and Exposition on Noise Control Engineering 2013, INTER-NOISE 2013:

De Rosa S, Franco F, Li X, et al. (2012) A similitude for structural acoustic enclosures. *Mechanical Systems and Signal Processing* 30: 330–342. DOI: 10.1016/j.ymssp.2012.01.018.

Duan T, Wei J, Zhang A, et al. (2021) Transmission error investigation of gearbox using rigid-flexible coupling dynamic model: Theoretical analysis and experiments. *Mechanism and Machine Theory* 157. Elsevier Ltd: 104213. DOI: 10.1016/j.mechmachtheory.2020.104213.

Fischer D and Isermann R (2004) Mechatronic semi-active and active vehicle suspensions. *Control Engineering Practice* 12(11): 1353–1367. DOI: 10.1016/j.conengprac.2003.08.003.

Fredriksson J, Weiefors H and Egardt B (2002) Powertrain control for active damping of driveline oscillations. *Vehicle System Dynamics* 37(5): 359–376. DOI: 10.1076/vesd.37.5.359.3527.

Gardonio P, Turco E, Kras A, et al. (2021) Semi-active vibration control unit tuned to maximise electric power dissipation. *Journal of Sound and Vibration* 499. Elsevier Ltd: 116000. DOI: 10.1016/j.jsv.2021.116000.

Gripp JAB and Rade DA (2018) Vibration and noise control using shunted piezoelectric transducers: A review. *Mechanical Systems and Signal Processing* 112. Elsevier Ltd: 359–383. DOI: 10.1016/j.ymssp.2018.04.041.

Guglielmino E and Edge KA (2004) A controlled friction damper for vehicle applications. *Control Engineering Practice* 12(4): 431–443. DOI: 10.1016/S0967-0661(03)00119-9.

Guo DL, Hu HY and Yi JQ (2004) Neural Network Control for a Semi-Active Vehicle Suspension with a Magnetorheological Damper. *JVC/Journal of Vibration and Control* 10(3): 461–471. DOI: 10.1177/1077546304038968.

Guo R and Zhou Z (2020) Non-Linear Modeling and Parameter Identification of Semi-Active Engine Mounts With Air Spring. *Journal of Vibration and Acoustics, Transactions of the ASME* 142(February): 2070–2082. DOI: 10.1115/1.4045267.

Halliday D, Resnick R and Walker J (2013) *Fundamentals of Physics*. Hoboken: Wiley.

Han HW, Im WH, Choi HJ, et al. (2022) Effect of sound insulation on noise reduction in an agricultural tractor cab. *Scientific Reports* 12(1). Nature Publishing Group UK: 1–15. DOI: 10.1038/s41598-022-26408-3.

Hickling R, Lee P, Goumilevski A, et al. (1997) Determining sound power for automotive applications. *SAE Transactions* 106(1997): 3151–3163. DOI: 10.4271/972037.

Hong J, Chen LL, Ma Y, et al. (2013) Hysteretic properties of metal rubber particles. *Proceedings of the Institution of Mechanical Engineers, Part C: Journal of Mechanical Engineering Science* 227(4): 693–702. DOI: 10.1177/0954406212452380.

Hu X (2017) Study on dynamic behavior of CRH380B type high speed vehicle with suspension component failures. In: *Proceedings of 2016 IEEE International Wheelset Congress, IWC 2016*, 2017, pp. 151–155. IEEE. DOI: 10.1109/IWC.2016.8068386.

Jia S and Howard I (2006) Comparison of localised spalling and crack damage from dynamic modelling of spur gear vibrations. *Mechanical Systems and Signal Processing* 20(2): 332–349. DOI: 10.1016/j.ymssp.2005.02.009.

Jiang G and He G (2014) Enhancement of the porous titanium with entangled wire structure for load-bearing biomedical applications. *Materials and Design* 56. Elsevier Ltd: 241–244. DOI: 10.1016/j.matdes.2013.11.019.

Jiang Y, Chen S, Gu F, et al. (2021) A modified feedforward hybrid active noise control system for vehicle. *Applied Acoustics* 175. Elsevier Ltd: 107816. DOI: 10.1016/j.apacoust.2020.107816.

Jin X, Chen K, Ji J, et al. (2019) Intelligent vibration detection and control system of agricultural machinery engine. *Measurement: Journal of the International Measurement Confederation* 145. Elsevier Ltd: 503–510. DOI: 10.1016/j.measurement.2019.05.059.

Khawaja T and Vachtsevanos G (2009) A novel architecture for on-line failure prognosis using probabilistic least squares support vector regression machines. *Annual Conference of the Prognostics and Health Management Society, PHM 2009*: 1–8.

Klaerner M, Wuehrl M, Marburg S, et al. (2015) Efficient FEA simulation of structure borne sound radiation. In: *DYNAMICAL SYSTEMS Mathermatical and Numerical Approaches*, pp. 279–290.

Kołakowski P, Szelek J, Sekuła K, et al. (2011) Structural health monitoring of a railway truss bridge using vibration-based and ultrasonic methods. *Smart Materials and Structures* 20(3). DOI: 10.1088/0964-1726/20/3/035016.

Komatsuzaki T, Inoue T and Terashima O (2016) Broadband vibration control of a structure by using a magnetorheological elastomer-based tuned dynamic absorber. *Mechatronics* 40. Elsevier Ltd: 128–136. DOI: 10.1016/j.mechatronics.2016.09.006.

Kong X, Tang J, Siyu C, et al. (2021) Effects of gearbox housing flexibility on dynamic characteristics of gear transmission system. *JVC/Journal of Vibration and Control* 27(17–18): 2097–2108. DOI: 10.1177/1077546320953733.

Koronias G, Theodossiades S, Rahnejat H, et al. (2011) Axle whine phenomenon in light trucks : a combined numerical and experimental investigation. *Journal of Automobile Engineering* 225(7): 885–894. DOI: 10.1177/0954407011401302.

Kumar A, Dwivedi A, Jaiswal H, et al. (2015) *Material-Based Vibration Characteristic Analysis of Heavy Vehicle Transmission Gearbox Casing Using Finite Element Analysis*. DOI: 10.1007/978-81-322-2012-1_80.

Laib F, Braun A and Rid W (2019) Modelling noise reductions using electric buses in urban traffic. A case study from Stuttgart, Germany. *Transportation Research Procedia* 37(September 2018). Elsevier B.V.: 377–384. DOI: 10.1016/j.trpro.2018.12.206.

Li S, Zhou C, Savin L, et al. (2023) Theoretical and experimental study of motion suppression and friction reduction of rotor systems with active hybrid fluid-film bearings. *Mechanical Systems and Signal Processing* 182(600). Elsevier Ltd: 109548. DOI: 10.1016/j.ymssp.2022.109548.

Li T (2018) Literature review of tire-pavement interaction noise and reduction approaches. *Journal of Vibroengineering* 20(6): 2424–2452. DOI: 10.21595/jve.2018.19935.

Liu J and Liu K (2006) A tunable electromagnetic vibration absorber: Characterization and application. *Journal of Sound and Vibration* 295(3–5): 708–724. DOI: 10.1016/j.jsv.2006.01.033.

Lossouarn B, Deü J, Aucejo M, et al. (2016) Multimodal vibration damping of a plate by piezoelectric coupling to its analogous electrical network. *Smart Materials and Structures* (March 2018). DOI: 10.1088/0964-1726/25/11/115042.

Ma H, Zhu S, Luo C, et al. (2023) Structural optimization design of metal rubber isolator based on an ensemble surrogate model. *Structures* 56(June). Elsevier Ltd: 104964. DOI: 10.1016/j.istruc.2023.104964.

Ma R, Bi K and Hao H (2021) Inerter-based structural vibration control: A state-of-the-art review. *Engineering Structures* 243(January). Elsevier Ltd: 112655. DOI: 10.1016/j.engstruct.2021.112655.

Ma Y, Scarpa F, Zhang D, et al. (2013) A nonlinear auxetic structural vibration damper with metal rubber particles. *Smart Materials and Structures* 22(8). DOI: 10.1088/0964-1726/22/8/084012.

Mendia-Garcia I, Facchinetti A, Bruni S, et al. (2023) Analysis and modelling of the dynamic stiffness up to 400 Hz of an air spring with a pipeline connected to a reservoir. *Journal of Sound and Vibration* 557(November 2022). Elsevier Ltd: 117740. DOI: 10.1016/j.jsv.2023.117740.

Mróz A, Holnicki-Szulc J and Kärnä T (2008) Mitigation of ice loading on off-shore wind turbines: Feasibility study of a semi-active solution. *Computers and Structures* 86(3–5): 217–226. DOI: 10.1016/j.compstruc.2007.01.039.

Munir MW and Abdulla WH (2020) On FxLMS Scheme for Active Noise Control at Remote Location. *IEEE Access* 8: 214071–214086. DOI: 10.1109/ACCESS.2020.3040718.

N. Felder G and M. Felder K (2015) *Mathematical Methods in Engineering and Physics*. Hoboken: Wiley.

Nagino H, Mikami T and Mizusawa T (2008) Three-dimensional free vibration analysis of isotropic rectangular plates using the B-spline Ritz method. *Journal of Sound and Vibration* 317(1–2): 329–353. DOI: 10.1016/j.jsv.2008.03.021.

Nguyen VK and Dien P (2009) Linearization and parametric vibration analysis of some applied problems in multibody systems. *Multibody Syst Dyn* 22(2): 163–180. DOI: 10.1007/s11044-009-9156-4.

Nitzsche F (2012) The use of smart structures in the realization of effective semi-active Control systems for vibration reduction. *Journal of the Brazilian Society of Mechanical Sciences and Engineering* 34(spe): 371–377. DOI: 10.1590/s1678-58782012000500005.

Noh HM (2017) Contribution analysis of interior noise and floor vibration in high-speed trains by operational transfer path analysis. *Advances in Mechanical Engineering* 9(8): 1–14. DOI: 10.1177/1687814017714986.

Ognjanović M and Kostić SC (2012) Gear unit housing effect on the noise generation caused by gear teeth impacts. *Strojniski Vestnik/Journal of Mechanical Engineering* 58(5): 327–337. DOI: 10.5545/sv-jme.2010.232.

Onoda J, Makihara K and Minesugi K (2003) Energy-recycling semi-active method for vibration suppression with piezoelectric transducers. *44th AIAA/ASME/ASCE/AHS/ASC Structures, Structural Dynamics, and Materials Conference* 41(4). DOI: 10.2514/6.2003-1869.

Ouyang T, Su Z, Li S, et al. (2019) Experimental and numerical investigations on dynamic characteristics of gear-roller-bearing system. *Mechanism and Machine Theory* 140. Elsevier Ltd: 730–746. DOI: 10.1016/j.mechmachtheory.2019.06.034.

Pérez A, Ferreño D, Carrascal IA, et al. (2020) Metal cushion dampers for railway applications: A review. *Construction and Building Materials* 238. DOI: 10.1016/j.conbuildmat.2019.117711.

Petrone G, D'Alessandro V, Franco F, et al. (2014) Numerical and experimental investigations on the acoustic power radiated by Aluminium Foam Sandwich panels. *Composite Structures* 118(1). Elsevier Ltd: 170–177. DOI: 10.1016/j.compstruct.2014.07.031.

Poplawski B, Mikułowski G, Wiszowaty R, et al. (2021) Mitigation of forced vibrations by semi-active control of local transfer of moments. *Mechanical Systems and Signal Processing* 157. Elsevier Ltd: 107733. DOI: 10.1016/j.ymssp.2021.107733.

Rao SS (2011) *Mechanical Vibrations*. Fifth. London: Pierson.

Rieß S and Kaal W (2021) Frequency-Adaptable Tuned Mass Damper Using Metal Cushions. *Frequency-Adaptable Tuned Mass Damper Using Metal Cushions* 4(1): 77–90. Available at: https://doi.org/10.3390/vibration4010007.

Shah BM, Nudell JJ, Kao KR, et al. (2011) Semi-active particle-based damping systems controlled by magnetic fields. *Journal of Sound and Vibration* 330(2). Elsevier: 182–193. DOI: 10.1016/j.jsv.2010.08.009.

Shi X, Mak CM and Yang J (2013) Attenuation Performance of a Semi-Active Helmholtz Resonator in a Grazing Flow Duct. *Open Journal of Acoustics* 03(01): 25–29. DOI: 10.4236/oja.2013.31004.

Shi X, Yu Q, Wu Z, et al. (2023) Active control for vehicle suspension using a self-powered dual-function active electromagnetic damper. *Journal of Sound and Vibration*. Elsevier Ltd: 117976. DOI: 10.1016/j.jsv.2023.117976.

Shiao Y, Lai CC and Nguyen QA (2010) The analysis of a semi-active suspension system. In: *Proceedings of the SICE Annual Conference*, Taipei, 2010, pp. 2077–2082. IEEE.

Shiao Y, Lai C and Nguyen Q (2023) The Analysis of a Semi-Active Suspension System. In: *Proceedings of SICE Annual Conference 2010*, Taipei, 2023, pp. 2070–2082. IEEE.

Silentflex (2023). Available at: https://silentflex.eu/.

Soleimanian S, Petrone G, Franco F, et al. (2023) Application of metal rubber for semi-active vibration control of mechanical transmission systems. *Journal of Vibration and Control* 0(0). Available at: https://doi.org/10.1177/10775463231192747.

Son GH, Kim BS, Cho SJ, et al. (2020) Optimization of the housing shape design for radiated noise reduction of an agricultural electric vehicle gearbox. *Applied Sciences (Switzerland)* 10(23): 1–19. DOI: 10.3390/app10238414.

Stabile A, Aglietti GS, Richardson G, et al. (2017) Design and verification of a negative resistance electromagnetic shunt damper for spacecraft micro-vibration. *Journal of Sound and Vibration* 386. Elsevier: 38–49. DOI: 10.1016/j.jsv.2016.09.024.

Stelzer GJ, Schulz MJ, Kim J, et al. (2003) A magnetorheological semi-active isolator to reduce noise and vibration transmissibility in automobiles. *Journal of Intelligent Material Systems and Structures* 14(12): 743–765. DOI: 10.1177/104538903038840.

Syam TMI and Muthalif AGA (2021) Magnetorheological Elastomer based torsional vibration isolator for application in a prototype drilling shaft. *Journal of Low Frequency Noise Vibration and Active Control* 0(0): 1–25. DOI: 10.1177/14613484211044627.

Symans MD and Constantinou MC (1999) Semi-active control systems for seismic protection of structures: A state-of-the-art review. *Engineering Structures* 21(6): 469–487. DOI: 10.1016/S0141-0296(97)00225-3.

Tan Q and He G (2012) 3D entangled wire reinforced metallic composites. *Materials Science and Engineering A* 546. Elsevier B.V.: 233–238. DOI: 10.1016/j.msea.2012.03.058.

Tang N and Rongong JA (2019) Feasibility study on the use of tangled metal wire particles as the adjustable elements in tuned mass dampers. *Journal of Sound and Vibration* 457. Elsevier Ltd: 1–14. DOI: 10.1016/j.jsv.2019.05.045.

Ulanov AM and Bezborodov SA (2016) Calculation Method of Pipeline Vibration with Damping Supports Made of the MR Material. *Procedia Engineering* 150. The Author(s): 101–106. DOI:

10.1016/j.proeng.2016.06.725.

UN-ECE Regulation (n.d.).

Venhovens PJTH, Van Der Knaap ACM and Pacejka HB (1993) Semi-Active Attitude and Vibration Control. *Vehicle System Dynamics* 22(5–6): 359–381. DOI: 10.1080/00423119308969037.

Viscardi M, Arena M, Siano D, et al. (2018) Validation of an innovative viscoelastic treatment, integrated on a real vehicle mock-up for the internal vibro-acoustic improvement. *International Journal of Vehicle Noise and Vibration* 14(4): 341–360. DOI: 10.1504/IJVNV.2018.099796.

Wang H, Rongong JA, Tomlinson GR, et al. (2010) Nonlinear static and dynamic properties of Metal Rubber dampers. In: *Proceedings of ISMA 2010 - International Conference on Noise and Vibration Engineering, including USD 2010*, Leuven, 2010, pp. 1301–1315.

Wang X (2010) *Vehicle Noise and Vibration Refinement*. Cambridge: Woodhead Publishing Limited. DOI: 10.1533/9781845698041.

Wang Y, Yang J, Guo D, et al. (2016) Vibration and sound radiation analysis of the final drive assembly considering the gear-shaft coupling dynamics. *Proceedings of the Institution of Mechanical Engineers, Part C: Journal of Mechanical Engineering Science* 230(7–8): 1258–1275. DOI: 10.1177/0954406216632021.

Wei K, Meng G, You H, et al. (2009) Study on a new semi-active vibration isolation system. *Second International Conference on Smart Materials and Nanotechnology in Engineering* 7493(July): 749357. DOI: 10.1117/12.840173.

Wu H and Wu G (2016) Driveline Torsional Analysis and Clutch Damper Optimization for Reducing Gear Rattle. *Shock and Vibration* (1): 1–24. Available at: https://doi.org/10.1155/2016/8434625.

Xiao K, Bai H, Xue X, et al. (2018) Damping Characteristics of Metal Rubber in the Pipeline Coating System. *Shock and Vibration* (1): 1–11. DOI: 10.1155/2018/3974381.

Xie Q, Zhang N, Zhang B, et al. (2016) Boundary condition handling approaches for the model reduction of a vehicle frame. *Mechanical Systems and Signal Processing* 75. Elsevier: 123–137. DOI: 10.1016/j.ymssp.2015.12.018.

Xin FL, Bai XX and Qian LJ (2017) Principle, modeling, and control of a magnetorheological elastomer dynamic vibration absorber for powertrain mount systems of automobiles. *Journal of Intelligent Material Systems and Structures* 28(16): 2239–2254. DOI: 10.1177/1045389X16672731.

Xue X, Ruan S, Bai H, et al. (2020) An enhanced constitutive model for the nonlinear mechanical behavior of the elastic-porous metal rubber. *Mechanics of Materials* 148(May). Elsevier: 103447. DOI: 10.1016/j.mechmat.2020.103447.

Yang Y, Pan G, Yin S, et al. (2021) Verification of vibration isolation effectiveness of the underwater vehicle power plant. *Journal of Marine Science and Engineering* 9(4). DOI: 10.3390/jmse9040382.

Zhang CW, Ou JP and Zhang JQ (2006) Parameter optimization and analysis of a vehicle suspension system controlled by magnetorheological fluid dampers. *Structural Control and Health Monitoring* 13(5): 885–896. DOI: 10.1002/stc.63.

Zhang D, Scarpa F, Ma Y, et al. (2013) Compression mechanics of nickel-based superalloy metal rubber. *Materials Science and Engineering A* 580. Elsevier: 305–312. DOI: 10.1016/j.msea.2013.05.064.

Zhang K, Zhou Y and Jiang J (2015) Experimental study and dynamic modeling of metal rubber isolating bearing. *IOP Conference Series: Materials Science and Engineering* 103(1). DOI: 10.1088/1757-899X/103/1/012048.

Zhang S (2018) Parameter Study and Improvement of Gearbox Whine Noise in Electric Vehicle. *Automotive Innovation* 1(3). Springer Singapore: 272–280. DOI: 10.1007/s42154-018-0029-5.

Zhang X, Li K, Li L, et al. (2023) Temperature-controlled tunable zigzag metamaterial beams to manipulate flexural waves. *Journal of Sound and Vibration* 563(December 2022). Elsevier Ltd: 117863. DOI: 10.1016/j.jsv.2023.117863.

Zhao H, Wang B and Chen G (2021) Numerical study on a rotational hydraulic damper with variable damping coefficient. *Scientific Reports* 11(1). Nature Publishing Group UK: 1–16. DOI: 10.1038/s41598-021-01859-2.

Zuo L and Tang X (2013) Large-scale vibration energy harvesting. *Journal of Intelligent Material Systems and Structures* 24(11): 1405–1430. DOI: 10.1177/1045389X13486707.